Synthesis and Surface Characterization of Semiconductor Nanocrystals for Photovoltaic Application

Von der Fakultät für Mathematik und Naturwissenschaften

der Carl von Ossietzky Universität Oldenburg

zur Erlangung des Grades und Titels eines

Doktors der Naturwissenschaften (Dr. rer. nat.)

angenommene Dissertation

von

Frau Dipl.-Chem. Irina Lokteva

geboren am 27.08.1985
in Woronesch, Russland

Erstgutachter: Jun.-Prof. Dr. Joanna Kolny-Olesiak

Zweitgutachter: Prof. Dr. Jürgen Parisi

Tag der Disputation: 30.06.2010

Abstract

In the first part of the thesis, the kinetics of a novel colloidal synthesis of nearly monodisperse CdSe and CdS QDs involving *in situ* formed Cd^0 particles was studied. Reactions with different types of Se and S precursors, Cd to Se and S ratio, and different amount of the stabilizer (oleic acid) were characterized by UV-Vis absorption spectroscopy. The Cd and Se/S precursor solutions were investigated by means of atomic absorption spectroscopy (AAS) as well as ^{1}H and ^{13}C nuclear magnetic resonance (NMR) spectroscopy and mass-spectrometry (MS). Transmission electron microscopy (TEM) was used to determine the size distribution of as-synthesized CdSe and CdS NCs. Formation of magic-sized nanoclusters (MSNCs) during the synthesis (at the early stages of the reactions) and storage of CdS QDs was observed.

In the second part, a surface modification of originally oleic acid-capped CdSe QDs with pyridine molecules was carried out. Three successive steps of the pyridine treatment were applied to achieve better ligand exchange. The pyridine-treated NCs were characterized by UV-Vis absorption spectroscopy, TEM and high resolution TEM (HRTEM), ^{1}H NMR spectroscopy, X-ray diffraction (XRD) and thermal gravimetric analysis (TGA). Then the pyridine-treated CdSe QDs were used for the fabrication of hybrid P3HT/CdSe solar cells. Additionally, a cross-linking procedure of the pyridine-treated NCs was applied to enable more efficient charge transfer between nanoparticles in the hybrid blends.

Zusammenfassung

Im ersten Teil dieser Arbeit wurde die Kinetik einer neuen kolloidchemischen Synthese von monodispersen sphärischen CdSe- und CdS-Nanopartikeln (QDs) untersucht, deren Wachstum in Gegenwart von *in situ* gebildetem Cd^0 erfolgt. Reaktionen mit verschiedenen Se- und S-Ausgangsverbindungen, Cd- zu Se- und S-Verhältnissen und Mengen des Stabilisators (Ölsäure) wurden mit UV-Vis-Absorptionsspektroskopie charakterisiert. Die Cd- und Se/S-Ausgangslösungen wurden mit Atomabsorptionsspektroskopie (AAS) sowie ^{1}H- und ^{13}C-Kernresonanzspektroskopie (NMR) und Massenspektrometrie (MS) analysiert. Mit Transmissionselektronenmikroskopie (TEM) wurde die Größenverteilung der CdSe- und CdS-Nanopartikel untersucht. Die Bildung von Nanoclustern mit magischen Größen (MSNCs) wurde während der Synthese (am Anfang der Reaktion) und Lagerung der CdS-Nanopartikel beobachtet.

Im zweiten Teil der Arbeit wurde die Modifikation der ursprünglich Ölsäure-beschichteten CdSe QDs mit Pyridinmolekülen durchgeführt. Für einen vollständigeren Ligandenaustausch wurden drei aufeinanderfolgende Schritte der Pyridinbehandlung angewendet. Die mit Pyridinliganden stabilisierten CdSe-Nanopartikel wurden mit UV-Vis-Absorptionsspektroskopie, TEM und hochauflösendem TEM (HRTEM), ^{1}H-Kernresonanzspektroskopie (NMR), Röntgendiffraktometrie (XRD) und Thermogravi-metrischer Analyse (TGA) charakterisiert. Anschließend wurden die mit Pyridin behandelten CdSe QDs für die Herstellung der P3HT/CdSe-Hybridsolarzellen verwendet. Zusätzlich wurde eine Quervernetzung der Pyridin-beschichteten Nanoteilchen

durchgeführt, um den Ladungstransfer zwischen Nanopartikeln zu verbessern.

Table of Contents

List of Figures

List of Tables

List of Abbreviations

AAS	Atomic absorption spectroscopy
BHJ	Bulk Heterojunction
CdSeOA	as-Synthesized Oleic Acid Capped CdSe QDs
CdSePy1	CdSe QDs after First Pyridine Treatment
CdSePy2	CdSe QDs after Second Pyridine Treatment
CdSePy3	CdSe QDs after Third Pyridine Treatment
COSY	Two-Dimensional Correlation NMR Spectroscopy
DAH	1,7-Diaminoheptane
EDX	Energy-Dispersive X-ray analysis
FF	Fill Factor
FFT	Fast Fourier Transform
FWHM	Full Width at Half-Maximum
HOMO	Highest Occupied Molecular Orbital
HRTEM	High Resolution Transmission Electron Microscopy
HWHM	Half-Width at Half-Maximum
ITO	Indium Tin Oxide
LUMO	Lowest Unoccupied Molecular Orbital
MEH-PPV	Poly(2-methoxy-5-(2-ethylhexoxy)-p-phenylenevinylene)
MS	Mass-Spectrometry
MSNC	Magic-Sized Nanocrystal

NC	Nanocrystal
NMR	Nuclear Magnetic Resonance
NP	Nanoparticle
OA	Oleic Acid
ODE	1-Octadecene
P3HT	Poly(3-hexylthiophene)
PCE	Power Conversion Efficiency
PEDOT : PSS	Poly(3,4-ethylenedioxythiophene) : Polystyrene Sulfonate
PL	Photoluminescence
PV	Photovoltaic
QD	Quantum Dot
QY	Quantum Yield
RNC	Regular-Sized Nanocrystal
TBP	Tri-n-butylphosphine
TBPS	Tri-n-butylphosphine Sulfide
TBPSe	Tri-n-butylphosphine Selenide
TEM	Transmission Electron Microscopy
TGA	Thermal Gravimetric Analysis
TMB	3,3',5,5'-Tetramethylbenzidine
TOP	Tri-n-octylphosphine
TOPO	Tri-n-octylphosphine Oxide
TOPS	Tri-n-octylphosphine Sulfide
TOPSe	Tri-n-octylphosphine Selenide
UV-Vis	Ultraviolet-Visible
v	volume
wt.	weight
XRD	Powder X-ray Diffraction

Chapter 1

Introduction

The research described in this thesis focuses on the characterization of optical and surface properties, composition of the ligand shell, and growth kinetics of CdSe and CdS semiconductor nanocrystals (NCs).

Nanocrystalline structures have attracted great interest over the past years because their properties are remarkably different from those of bulk materials and can be controlled by the particles composition, size, and surface [1][2][3]. Nanoparticles (NPs) possess these interesting characteristics due to several phenomena (such as quantum confinement of charge carriers, surface effects, and geometrical confinement of phonons, etc.) that turned them into promising materials for many applications, such as light-emitting diodes [4], photovoltaic devices [5], lasers [6], optical memories [7], miniaturized devices, and fluorescent probes in biological labeling [8][9]. To satisfy more complicated applications, various structured NCs such as core/shell, heterostructure, etc. have also been produced based on CdSe NCs in the past decade.

Nanoscaled materials possess a variety of properties depending on the chemical composition. The following list enumerates some examples of materials that can be produced in the nanometer range:

- Oxides: TiO_2 [10][11], ZrO_2 [12][13], CoO [14], WO_3 [15], ZnO [16], etc.

- Metals: gold [17][18], silver [19], platinum [20], cobalt [21], palladium [22].
- Semiconductors: II-VI compounds (CdSe [23][24], CdTe [25][26], CdS [27], ZnSe, ZnTe, ZnS [28]), III-V compounds (GaAs [29], GaP, InAs [30], InP), IV-VI compounds (PbS, PbSe [31], PbTe [32]) and silicon [33].

Nanoparticles can be prepared in various shapes such as quantum dots (QDs), rods, tetrapods, nanowires, nanobelts, nanotubes, etc. The quantum dots (QDs) are nanometer-scale semiconductor crystals and are defined as particles with physical dimensions smaller than the exciton Bohr's radius in the bulk material. It is reported that optimum size variation in CdSe nanocrystals due to quantum confinement is from 1 to 11 nm (this means the particle contains 10-10.000 atoms). With the decrease of sizes, the electronic structures of QDs could transform from bulk continuous bands into molecule-like discrete levels (Fig. 1.1), and the excitonic transition energy is apparently blue-shifted from the bulk band gap both in the absorption and the photoluminescence (PL) spectra. In other words, strong differences observed in fundamental optical and electrical properties of semiconductor NCs in comparison to bulk material arise from systematic variations in the density of electronic energy levels as a function of size. NCs lie between the atomic limit of discrete electronic energy states and extended crystalline limits of continuous bands as shown in Fig. 1.1. Since in semiconductors the Fermi level lies between two bands (Fig. 1.1), the edges of the bands dominate the low-energy optical and electrical behavior. Therefore, optical excitations across the gap and electrical transport depend strongly on size for semiconductor (e.g. CdSe) QDs. As a consequence, many useful size dependent phenomena are observed in nanoclusters that possess similar to the bulk solid structure, but have a substantial fraction of the total number of atoms on the surface [34].

Attractive optical properties of these nanoparticles, in particular, the wide absorption range in the visible region with the positions of the first excitonic maximum depend-

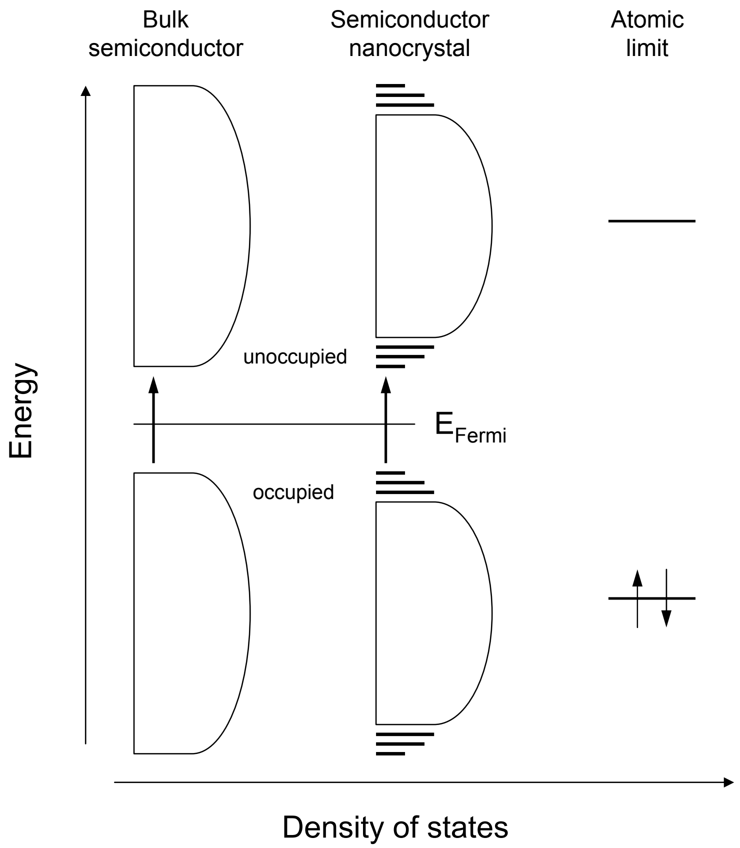

Figure 1.1: Schematic illustration of the density of states in bulk semiconductors and semiconductor nanocrystals (from [34]).

ing on the NCs size and a bright fluorescence emission from blue to red with very pure color, a high fluorescence quantum yield (QY) (up to 85 % for CdSe QDs [35]) and great photostability motivated much research on the NCs application in various fields. For instance, nanocrystal-based emitters can be used in light-emitting diodes [36] and quantum-dot lasers; due to their high QY and photostability, QDs find application in biomedical labeling [37]; the size dependent band gap allows to use them as a component in solar cells [38]. Thus, thanks to the effect of quantum confinement, it is possible to tune the optical and electrical properties of semiconductor nanocrystals by simply varying their size.

In this thesis, we are mainly concerned with CdSe and CdS semiconductor QDs synthesized by a hot-injection colloidal method in a solution in which the particles are covered by organic ligands to prevent aggregation and to control their size. The synthetic procedure used for the synthesis of CdSe and CdS QDs was originally developed by Kolny-Olesiak et al. for CdTe QDs [39][40] in which the nanoparticles synthesis includes formation of *in situ* crystalline 100-150 nm Cd^0 particles. The fabricated CdSe and CdS QDs have a very narrow size distribution; they are also highly soluble in most non-polar solvents, such as toluene, hexane, and chloroform, and have attractive optical properties, viz. intense fluorescence and tunable absorption in the visible spectral region (Chapter 4 and 5).

In Chapter 6, the investigation of the initial ligand shell of as-synthesized CdSe QDs with subsequent surface modification for photovoltaic applications is described. The pyridine molecules were chosen for ligand exchange of initially oleic acid capped CdSe NCs in order to reduce the ligand shell thickness and thus to enhance the charge transfer in the system nanoparticle/conjugated polymer. The analysis of the ligand cap after the surface modification revealed that besides pyridine molecules, still some amount of original oleic acid molecules was present, which encouraged us to fulfill repeated steps of the pyridine treatment. The application of pyridine-treated CdSe NCs for the fabrication of hybrid CdSe/P3HT solar cells is reviewed in Chapter 7. Supplementary material is provided in the Appendixes.

Chapter 2

Description of the experimental set-ups and methods of nanocrystals characterization

2.1 Sample preparation

CdSe and CdS colloidal nanocrystal quantum dots (QDs) were synthesized using the procedure previously described by Kolny-Olesiak et al. for CdTe QDs [39][40]. The samples were prepared using a well-known hot injection technique in a non-coordinating solvent at 300 ℃ with *in situ* formed crystalline Cd^0 particles.

Chemicals: cadmium oxide brown (CdO, 99 %, powder) was purchased from Fluka; tri-n-octylphosphine (TOP, 90 %), tri-n-butylphosphine (TBP, 97 %), oleic acid (OA, 90 %), and D-chloroform ($CDCl_3$, 99.8 atom % D) from Aldrich; 1-octadecene (ODE) from Merck; selenium (Se, 99.99 %, powder) from ChemPur; sulfur (S, powder) from Riedel-de Haën; regioregular poly(3-hexylthiophene) (P3HT) from Rieke Metals; poly(3,4-ethylenedioxythiophene) : polystyrene sulfonate (PEDOT : PSS) from H.C. Starck. All reagents were used as received without further purification. All solvents were obtained from commercial sources and used as received. Standard glove box technique was used where necessary for the manipulation of the materials under inert atmosphered conditions.

2.1.1 Synthesis of the CdSe nanocrystals

The scheme of the experimental set-up is represented in Fig. 2.1. The synthesis of the CdSe QDs was initiated by preparation of three Se precursor solutions. 1) A TOPSe injection solution containing 0.0790 g of Se (1.0 mmol) was prepared in a glove box by mixing Se powder with 2.1120 g of TOP (5.7 mmol), diluted with ODE to a total amount of 10 g and permanently stirred until all Se dissolved and the solution looked optically clear; 2) A TBPSe injection solution was prepared in a glove box by mixing 0.0790 g of Se (1.0 mmol) with 1.1528 g of TBP (5.7 mmol), diluted with ODE to a total amount of 10 g and permanently stirred until all Se dissolved and the solution looked optically clear; 3) A Se/ODE injection solution (0.18 M) was prepared by dissolving 0.3555 g of Se powder (4.50 mmol) in 25 mL of ODE without adding TOP

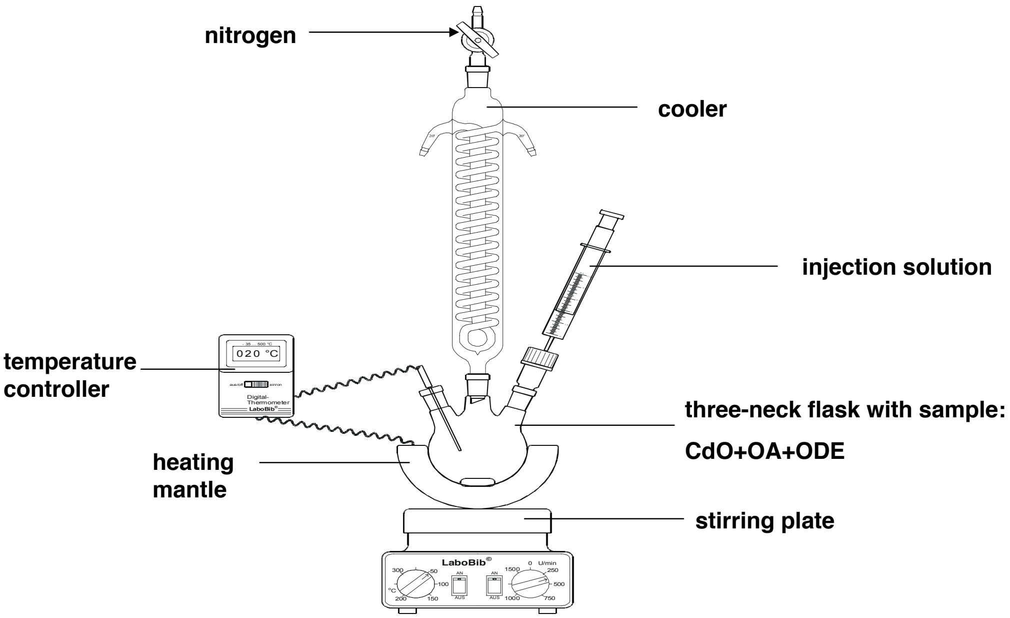

Figure 2.1: Scheme of the experimental set-up for the synthesis of NCs.

or TBP. This solution was heated under standard air-free conditions to 200 ℃ for 2 h. During this time, the color of the ODE/Se mixture changed from colorless to light red and finally to canary yellow. The resulting transparent yellow solution was cooled to room temperature where it remained stable for months.

A mixture of CdO (0.0256 g, 0.20 mmol), OA (200 µl, 0.63 mmol), and ODE (10 mL) was heated in a three-neck flask to 100 ℃ under a vacuum for 30 min while constantly being stirred to obtain a homogenous red mixture.

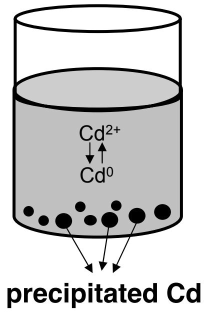

Figure 2.2: *In situ* formed Cd^0 particles.

Then the system was turned to nitrogen flow and heated to 300 ℃ until all CdO dissolved in the OA-ODE mixture. The colorless solution of Cd-oleate complex in ODE at 300 ℃ was allowed to boil without restriction. After 30-90 min (depending on the OA concentration) a grayish precipitate of Cd^0 particles started to form (Fig. 2.2). The Se solution was injected right away after first observing the precipitation. The color of the reaction solution changed almost immediately (from light yellow to wine red) upon injection of the TOPSe, TBPSe, or Se/ODE stock solution, which indicated fast nucleation and growth. Aliquots were taken out at different reaction times to monitor the reaction process by measuring the UV-Vis absorbance. Size-selective precipitation was not necessary to further narrow the size distribution.

2.1.2 Synthesis of the CdS nanoparticles

The synthesis of the CdS QDs was fulfilled analogous to the synthesis of the CdSe QDs with the only difference that one of three S precursors (S/ODE, TOPS, or TBPS) was injected instead of the Se precursors. S precursors were prepared as follows: 1) A TOPS injection solution containing 0.0320 g of S (1.0 mmol) was prepared in a glove box by mixing S powder with 2.1120 g of TOP (5.7 mmol), diluted with ODE to a total amount of 10 g and constantly stirred at room temperature until all S dissolved and the solution looked optically clear; 2) A TBPS injection solution was prepared in a glove box by mixing 0.0320 g of S (1.0 mmol) with 1.1528 g of TBP (5.7 mmol), diluted with ODE to a total amount of 10 g and constantly stirred until all S dissolved and the solution looked optically clear; 3) A S/ODE injection solution (0.2 M) was prepared by dissolving 0.3200 g of S powder (10 mmol) in 50 mL of ODE without adding TOP or TBP. This solution was heated under standard air-free conditions to 200 ℃ for 20 min until the sulfur dissolved and the solution appeared as a light or canary yellow. This resulting transparent yellow solution was cooled to room temperature where it remained stable. Under identical synthetic conditions to CdSe nanoparticles, introduction of the TOPS, TBPS, or S/ODE stock solutions resulted in changes of the reaction mixture from colorless to canary yellow over a 2100 s period.

For the reactions without *in situ* formed Cd^0 precipitate, a S precursor was injected after a colorless solution of Cd-oleate complex in ODE reached the temperature of 300 ℃.

2.1.3 Purification process

The purification procedure including extraction and precipitation steps was adopted from reference [41]. The fractions taken from the reaction vessel were centrifugated immediately in order to separate the nanocrystal solution from Cd^0 particles. Then the aliquots were mixed with an equal volume mixture of hexane and methanol (1:2 v/v) by vigorous shaking and centrifugated again to extract free ligands and excess of reagents. The colored nanoparticles layer was separated; the nanocrystals in the hexane-ODE phase were precipitated with excess acetone and methanol (5:1 v/v ratio to the extracted hexane-ODE solution) and redissolved in hexane. The precipitation/redissolution procedure was repeated several times. The final nanocrystal pellet on the bottom of the vial could be redissolved in a desired solvent (toluene, chloroform, or hexane).

2.1.4 Pyridine treatment of OA-capped CdSe QDs

For the preparation of solar cells, in order to fulfill the ligand exchange of the originally oleic acid coated CdSe NCs, a synthesis of CdSe QDs with initial molar ratio of Cd : Se = 1 : 2 and TOPSe as a Se precursor was carried out. The synthesis was scaled up four times to obtain a bigger quantity of nanoparticles, which were purified and then redissolved in 7 ml of pure pyridine. For a complete exchange of the ligands, the purified CdSe QDs redissolved in pyridine were heated in a water bath for 3 hours at 65 ℃ under constant stirring. Afterwards, the nanocrystal/pyridine solution was stirred overnight at room temperature. Excess hexanes were added to the nanocrystal/pyridine solution to precipitate the CdSe QDs. The nanocrystal precipitate was isolated by centrifugation and decantation and finally redissolved in 0.65 mL of pyridine (in order to obtain a final concentration of the CdSe QDs in pyridine of 215 mg/mL). The solution obtained at this step will be further referred to as CdSePy1 QDs. Part of this CdSePy1 QDs solution was subjected to a second and a third pyridine treatment step if needed (samples further referred to as CdSePy2 and CdSePy3 QDs, respectively) and carried out analogous to the first one. In this way, a series of samples were generated and treated three times with pyridine.

2.2 Analytical methods of characterization of the nanocrystals and the precursors

UV-Vis spectroscopy. Due to the quantum confinement effect, UV-Vis spectroscopy allows to determine the size and concentration as well as to predict the size distribution of the nanocrystals. UV-Vis spectra were recorded in hexane or pyridine on a Carry 100 absorption spectrophotometer using 1 cm path length quartz cells. The absorbance values were used to calculate the nanocrystal diameters and the molar nanocrystal extinction coefficients, together with the nanocrystal concentrations according to reference [42]. Peng et al. determined the following equations for nanoparticle sizes and molar nanocrystal extinction coefficients:

$$\begin{aligned} \text{For CdSe:} \quad D &= (1.6122 \times 10^{-9})\lambda^4 - (2.6575 \times 10^{-6})\lambda^3 + \\ &\quad +(1.6242 \times 10^{-3})\lambda^2 - (0.4277)\lambda + (41.57) \end{aligned} \tag{2.1}$$

$$\begin{aligned} \text{For CdS:} \quad D &= (-6.6521 \times 10^{-8})\lambda^3 + (1.9557 \times 10^{-4})\lambda^2 - \\ &\quad -(9.2352 \times 10^{-2})\lambda + 13.29 \end{aligned} \tag{2.2}$$

In the above equations, D (nm) is the diameter or size of a given nanocrystal sample, and λ (nm) is the wavelength of the first excitonic absorption peak of the corresponding sample.

$$\text{For CdSe:} \quad \epsilon = 5857\ (D)^{2.65} \tag{2.3}$$

$$\text{For CdS:} \quad \epsilon = 21536\ (D)^{2.3} \tag{2.4}$$

Here, ϵ is the extinction coefficient of semiconductor nanocrystals and D is the diameter of the nanocrystals. Then from Lambert-Beer's law one can calculate the molar concentration of the nanoparticles:

$$A = \epsilon C L \tag{2.5}$$

In this equation, A is the absorbance of the first exciton absorption peak for a given sample, ϵ is the extinction coefficient per mole of nanocrystals (L/(mol cm)), C is the molar concentration of the nanocrystals (mol/L), and L is the path length of the radiation beam used for recording the absorption spectrum (cm) (in our experiments,

L was fixed at 1 cm). Calculating C from Eq. 2.5 one should take into account the dilution of the measured NCs solution.

The absorbance A in Eq. 2.5 should be calibrated if the size distribution of the nanocrystals is significantly broader than that of the standard samples used for determination of the extinction coefficient (i.e. half-width at the half-maximum (hwhm) of the absorption spectrum is equal to 14 for CdSe and 11 for CdS). In this case the following equation should be used:

$$A = \frac{A_m (hwhm)_{UV}}{K} \tag{2.6}$$

A and A_m are the calibrated absorbance and the measured absorbance, respectively. $(hwhm)_{UV}$ is the half-width at the half-maximum on the longer wavelength side of the first absorption peak. K is the average $(hwhm)_{UV}$ of the standard samples used for the measurements of ϵ (K=14 for CdSe and K=11 for CdS).

Photoluminescence (PL) spectroscopy. PL spectra were measured at the experimental set-up constructed in the group of Prof. Lienau in the Physics Department at the University of Oldenburg. Shortly, in this set-up, a Xenon-lamp emits white light which is focused by a lens onto the entry slit of excitation monochromator. Bandwidth and light intensity are controlled with two slits. The second lens behind the monochromator makes the monochromatic light again parallel, and the third lens focuses the light onto the sample. PL spectra of the samples are collected by a lens in 90° geometry and then again decomposed by a monochromator and detected by a photomultiplier. The solution spectra were taken with an optical density below 0.05-0.1 at the excitation wavelength. This low absorption value should keep reabsorption of the emitted light by the sample at a negligible level.

Transmission electron microscopy (TEM). TEM is a valuable technique to study size, size distribution, shape, and morphology of CdSe QDs. HRTEM provides determination of individual crystalline morphology and internal structure. TEM images were obtained with EM 902A transmission electron microscope (Zeiss) operating at 80 kV, and HRTEM images were obtained using a Philips CM 20 FEG transmission electron microscope operating at an acceleration voltage of 200 kV. TEM specimens were prepared by putting a 10 µl aliquot drop of a very dilute hexane or pyridine solution onto a carbon-coated copper grid and subsequently dried at room temperature.

Nuclear magnetic resonance (NMR) spectroscopy. NMR spectroscopy is a widely used analytical method for the analysis of nanocrystals ligands since it allows both the analysis of the composition of the ligand shell and distinguishing between bound and free ligands. ^{1}H, ^{13}C, and ^{31}P NMR spectra were recorded on a Bruker DRX 500 and Bruker Avance III 500 NMR spectrometers operating at 500, 125.722, and 202.772 MHz, respectively. The spectra were referenced to as tetramethylsilane (TMS) at δ 0.0 or in the scale relative to $CDCl_3$ using the residual proton signal of $CDCl_3$ at δ 7.24 in the case of ^{1}H NMR spectra, to an internal $CDCl_3$ reference at δ 77.0 in the case of ^{13}C NMR spectra, or to an external phosphoric acid standard set at δ 0.0 in the case of ^{31}P NMR spectra. ^{1}H, ^{13}C, and ^{31}P NMR analyses were carried out either by dissolving a powder of a nanocrystal sample in $CDCl_3$ or by using recovered ligands dissolved in $CDCl_3$. To obtain the recovered ligands, purified nanocrystals were first digested by a DCl-D_2O solution in an ultrasonic bath to obtain optically clear solutions. Then the organic ligands were extracted by adding $CDCl_3$ to the DCl-D_2O solution and vigorous shaking [26].

X-ray powder diffraction (XRD). XRD was used to determine crystal structure and phase purity as well as to estimate the size of the NCs. The diameter of spherical particles can be estimated from the full width at half-maximum of a given Bragg's reflection from the Debye-Scherrer formula [43][44][45]:

$$d = \frac{4}{3} \cdot \frac{0.9\lambda}{B cos\theta} \tag{2.7}$$

Here, d is the mean diameter of the crystallite (nm), λ is the wavelength of the X-ray radiation (nm), B is the full width at half maximum (fwhm) of the peak (rad), and θ is the Bragg's angle of diffraction.

XRD patterns were collected on a Philips X'Pert-MPD diffractometer using Cu K_α radiation ($\lambda = 1.5406$ Å); samples were deposited onto special glass slides suitable to avoid contribution from the sample holder to the diffraction pattern.

Thermal gravimetric analysis (TGA). In the nanocrystal characterization, TGA enables access to information on the composition of the ligand shell, as one can observe the presence of several steps in the weight loss curve which correspond to different ligands. TGA measurements were performed under N_2 atmosphere on a TGA/SDTA-851e instrument from Mettler-Toledo, using a heating rate of 2.5 ℃/min up to a temperature of 500 ℃.

Energy-dispersive X-ray analysis (EDX). EDX spectroscopy was used for the elemental qualitative and quantitative analysis of the NC sample. EDX measurements were performed using concentrated samples deposited onto aluminum substrates with a Hitachi S-3200N scanning electron microscope operating at low vacuum (1-270 Pa).

Mass-spectrometry (MS). MS was used to determine the structure of organic compounds by observing the signals corresponding to their molecules and fragments. In our work, MS was applied for the analysis of the crude colloidal solutions of CdSe QDs in ODE and the injection precursors (Se/ODE and S/ODE). MS analysis was fulfilled on a Finnigan MAT 95 instrument with electron ionization (EI) at 70 eV.

Atomic absorption spectroscopy (AAS). AAS was used to investigate the concentration of *in situ* formed Cd^0 nanoparticles in the course of the reaction. AAS measurements were carried out on a Perkin Elmer AAS instrument 4100. The calibration was made with Cadmium AAS standard solution, Specpure (Cd 1000 µg/mL) from Alfa Aesar. Cd^0 particles were digested with concentrated H_2SO_4 and then treated with concentrated HNO_3 to obtain optically clear solutions. For measurements, these solutions were diluted with ultra pure water (final resistance of 18.2 MΩ cm^{-1}) obtained using a Millipore-Q System (Millipore Co. Ltd.).

2.3 Preparation and characterization of laboratory solar cells

Fabrication of solar cells

Hybrid nanoparticle/polymer blends of CdSe and regioregular poly(3-hexylthiophene) (P3HT) were prepared as follows. Colloidal solutions of pyridine-treated CdSe NCs dissolved in pyridine were blended with P3HT dissolved in chlorobenzene. The weight ratio of CdSe : P3HT was 10 : 1, and the volume ratio of chlorobenzene : pyridine was 4 : 1 in all measurements. The polymer/nanoparticle solution was stirred overnight for efficient mixing. Laboratory solar cells were prepared with a bulk heterojunction layer of the CdSe/P3HT blends sandwiched between a glass substrate (15 × 15 mm) coated with indium tin oxide (ITO) (which was covered with a layer of poly(ethylenedioxythiophene) doped with polystyrenesulfonic acid (PEDOT : PSS)[1]) as anode and an Al layer as cathode (Fig. 2.3a).

To avoid short circuits, half of the ITO coating was etched away with concentrated HCl and zinc powder. Subsequently, the substrates were cleaned with acetone (for

---

[1] The PEDOT : PSS layer improves the surface quality of the ITO electrode, reducing the probability of shunts, and facilitates the hole injection/extraction as well. Moreover, the work function of this electrode can be changed by chemical/electrochemical redox reactions of the PEDOT layer [46].

15 min) and isopropyl alcohol (2 times per 15 min) in an ultrasonic bath. The last cleaning step was O_2 plasma etching. The interfacial layer of PEDOT : PSS (Clevios ph, H. C. Starck) between the active layer and ITO was spin-coated from an aqueous solution on the cleaned substrate and dried at 180 ℃ under nitrogen atmosphere for 20 min. The active layer was deposited by spin coating solutions of CdSe and P3HT on top of the PEDOT : PSS layer under inert atmosphere. Thermal annealing of the composite thin films of CdSe/P3HT was applied at 140 ℃ for 20 min under inert atmosphere as well. Finally, the devices were completed by thermal evaporation of about 100 nm Al on top as cathode (Fig. 2.3b).

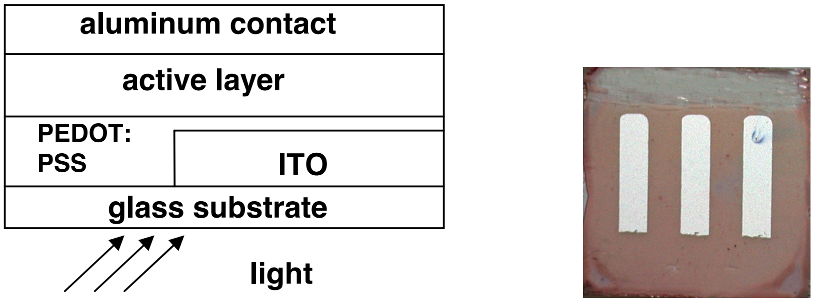

(a) (b)

Figure 2.3: Fabrication of the laboratory solar cells: (a) Schematic representation of a laboratory solar cell; (b) Photograph of a laboratory solar cell.

Cross-linking procedure

Two different cross-linking methods with each of the two cross-linker compounds (viz. 1,7-diaminoheptane and 3,3',5,5'-tetramethylbenzidine) were applied to modify the solar cells:

1. First, a cross-linker was added to the *a priori* prepared mixture of CdSe QDs in pyridine and P3HT in chlorbenzene (the molar ratio of the cross-linker to CdSe QDs was about 50 % (one cross-linker molecule per two nanoparticles)). The mixture was stirred at room temperature for a minimum of 3 hours. Then this solution was used to spin coat the active layer.
2. The active layer of the commonly prepared CdSe/P3HT mixture was spin coated

onto the glass/ITO/PEDOT:PSS layer. Then the substrate with the film was dipped into the dilute solution containing a cross-linker with successive electrode evaporation. The solvent of the cross-linker solution was chosen in such a way, that it could not dissolve both the NCs and the polymer: hexane for 1,7-diaminoheptane and acetone for 3,3',5,5'-tetramethylbenzidine. The used concentrations of these solutions were 10 mM for 1,7-diaminoheptane and 5 mM for 3,3',5,5'-tetramethylbenzidine. The immersing time was varied from 10 to 60 min.

For both methods, annealed and not annealed films were compared (annealing within 20 min at 140 ℃ before evaporation of the Al cathode was applied). The presence or absence of the annealing step is indicated during the discussion of the results for each sample (Chapter 7).

It should be pointed out that addition of a cross-linker to the solution of pure CdSe QDs in pyridine (i.e. without polymer) leads to the immediate coagulation of nanoparticles (indicating a strong effect of the linker molecules), which makes the NCs inappropriate for further processing.

Characterization of solar cells

Current-voltage (I-V) measurements carried out on a K. H. Steuernagel class B solar simulator were used to characterize the performance of the laboratory solar cells under AM1.5G[2] illumination (“Air Mass 1.5 Global”). The intensity of the solar simulator (1000 W/m^2) was calibrated using a calibrated Si (mono-Si, Fraunhofer ISE, Freiburg) reference solar cell; a spectral mismatch was not taken into account. All measurements were done at room temperature.

---

[2] AM1.5 approximates the intensity of sunlight that would be received on a tilted plane surface on a clear day, and for the model atmosphere containing specified concentrations of e.g. water vapor, and aerosol [47].

Chapter 3

Nucleation and growth of colloidal nanocrystals

This chapter describes the overview of theoretical models of nucleation and growth of spherical nanoparticles synthesized in colloidal solutions.

3.1 Nucleation of nanocrystals

3.1.1 LaMer model of NC nucleation and growth

Burst of nucleation concept

Research on the production of uniform colloidal particles dates back to the 1940s, when LaMer and colleagues [48] investigated various oil aerosols and sulfur hydrosols. The classic studies of LaMer and Dinegar [49] show that the preparation of monodisperse colloids requires a "burst of nucleation" where many nuclei are generated at the same time and no additional nucleation occurs during the growth of the existing nuclei. In the homogeneous nucleation process, nuclei appear without any seed for heterogeneous nucleation (dust, particles, or bubbles) and therefore, the energy barrier to nucleation in a homogeneous solution is extremely high [50]. Fig. 3.1 depicts the scheme of the influence of an energy barrier on “nucleation burst”. In stage I, no precipitation is observed even under the supersaturated conditions due to the high energy barrier of homogeneous nucleation. In stage II, the system can overcome this barrier when the degree of supersaturation is high enough, which results as a quick formation of stable nuclei. In stage III, the growth stage starts where no new nuclei are formed and the particles keep growing as long as the solution is supersaturated. At this stage, the number of NPs stays constant or decreases. The beginning of the growth relates to the decrease of the monomer concentration since the rate of monomer consumption by the nucleation and growth process exceeds the rate of monomer supply. If no growth of NPs occurs during nucleation, the resulting NCs will possess narrow size distributions. Hence, the concept of “burst of nucleation”, which separates nucleation and growth stages, is the key to the synthesis of monodisperse NCs.

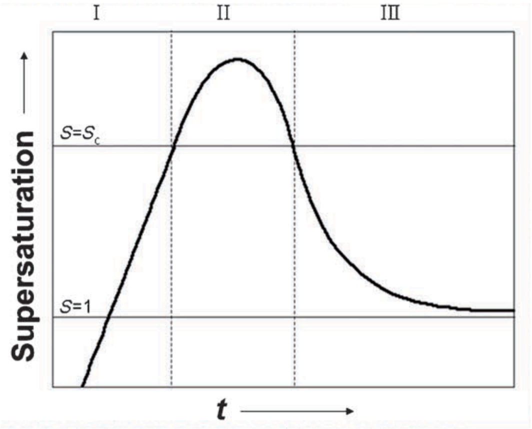

Figure 3.1: LaMer plot [50]: change of degree of supersaturation as a function of time [49].

Application of the LaMer model to the hot-injection method

Introduction of the hot-injection method for the synthesis of high quality II-VI semiconductor nanoparticles allowed to separate the nucleation and growth stages which resulted in improved quality of the obtained NCs (the size dispersion is <10 % [51][52]). Briefly, the hot-injection process can be described as a rapid injection of the precursor(s) at 300 ℃ with quick formation of relatively monodisperse nuclei; a drop in temperature to 250-270 ℃ due to the injection of the room temperature reactant(s) which leads to quenching of nucleation; growth of the nuclei to larger nanocrystals at the temperature at which the formation of new nuclei does not occur [53].

The nucleation stage, characterized by a rapid increase in the NP concentration, is very short, and sometimes it is difficult to observe it during the experiment. After the nucleation stage is completed, the maximum concentration of NCs is reached and then the concentration stays the same or starts to decrease. Thus, the experimental data give evidence that the crystallization process in the hot-injection method is likely to start at stage II in the LaMer plot (Fig. 3.1) when the critical level of supersaturation (see Eq. 3.6) is achieved [50].

However, the LaMer model does not predict the "focusing" and "defocusing" stages during the growth of NCs, which are often observed in the experiments. According to the mechanism of NC formation proposed by Peng et al. [54], after injection, a nucleation stage, which takes place rather quickly and is difficult to study, is followed by a growth stage. For the diffusion-controlled growth of spherical NCs, at any given monomer concentration there exists a critical size which is at equilibrium. NCs smaller than the critical size dissolve in the course of the reaction while larger ones grow at rates strongly dependent on size. Focusing of the size distribution occurs when the NCs present in the solution are all slightly larger than the critical size. Under these conditions, the small NCs grow faster than the large ones. Later, because of the depletion of the monomer concentration, the critical size becomes larger than the average size of NCs. That is why some small NCs begin to shrink in the solution while big ones keep growing, consuming from the small ones. This is the so-called "Ostwald ripening process", a concept in which the particle number decreases and the size distribution defocuses.

Thus, the LaMer model has some limitations for the hot-injection technique since it assumes that the nucleation burst does not alter the value of supersaturation significantly and that all of the seeds created during the nucleation stage may grow for extended times into much larger particles in the absence of competing reactions such as fresh nucleation or Ostwald ripening [55].

3.1.2 Thermodynamic considerations of NC nucleation

The energy barrier to the homogeneous nucleation is explained thermodynamically as follows [50]: the Gibbs free energy of the formation of spherical NPs ΔG with a radius r from the solution with a supersaturation S, in which γ is the surface free energy per unit area and ΔG_v is the free energy change between the monomers in solution and unit volume of bulk crystal, is given by

$$\Delta G = 4\pi r^2 \gamma + \frac{4}{3}\pi r^3 \Delta G_v \tag{3.1}$$

where

$$\Delta G_v = \frac{-RT \ln S}{V_m} \tag{3.2}$$

Here V_m is the molar volume of bulk crystal. ΔG_v has a negative value as long as the solution is supersaturated.

The value of r at the maximum ΔG is called a critical radius r_c and represents the minimum radius of the nucleus that can grow spontaneously in the supersaturated solution. Setting $d\Delta G/dr = 0$ allows to determine r_c:

$$r_c = \frac{2\gamma V_m}{RT \ln S_c} \tag{3.3}$$

Because r_c is a minimum radius that will persist and not dissolve in the solution, the critical supersaturation S_c should be as high as possible to induce the homogeneous nucleation. The sizes of the nuclei are estimated to be less than 1 nm [50].

Substitution of Eq. 3.3 into Eq. 3.1 (with consideration of Eq. 3.2) provides the critical free energy, which is necessary to form a stable nucleus:

$$\Delta G_c = \frac{16\pi\gamma^3 V_m^2}{3(RT\ln S_c)^2} \tag{3.4}$$

If the rate of nucleation is defined as the rate of increase of the number of particles N, it can be written in the Arrhenius form in terms of ΔG_c [50]:

$$\frac{dN}{dt} = A\exp\left(-\frac{\Delta G_c}{kT}\right) = A\exp\left(\frac{16\pi\gamma^3 V_m^2}{3k^3T^3N_A^2(\ln S_c)^2}\right) \tag{3.5}$$

Rewriting Eq. 3.5 to express S_c, the following equation can be obtained:

$$\ln S_c = \left(\frac{16\pi\gamma^3 V_m^2}{3k^3T^3(\ln(A/(dN/dt))}\right)^{1/2} \tag{3.6}$$

In contrast to the simple LaMer model, it is difficult to define exactly the critical supersaturation level S_c at which the stable nuclei are formed. It should be pointed out that together with NC precipitation, there is always redissolution of the formed particles as the system tries to attain equilibrium. At S_c, the rate of nucleation is higher than the rate of dissolution and the effective number of nuclei starts to increase (even while smaller nuclei still dissolve).

In this thermodynamic model, it is assumed that γ and ΔG_v are constants which is not applicable to nanosized crystals. In nanometer regime, these parameters are strongly size dependent. For example, as particle size decreases, the ratio of the surface atoms to the bulk significantly increases. Presumably, the aspiration of NPs to minimize the surface free energy leads to the changes of the crystal structure of NPs in comparison to bulk material (e.g. zinc blende structure of CdSe QDs vs. wurtzite structure of bulk CdSe; see Chapter 4) and plays a big role in the formation of very small and stable "magic-sized" clusters (e.g. CdS clusters described in Chapter 5).

3.2 Growth of nanocrystals

3.2.1 Reiss model of the growth of uniform NCs

The first theoretical studies of growth of monodisperse NCs were carried out by Reiss [56]. His model assumes "growth by diffusion", where the growth rate of spherical particles is determined by the flux of monomers to NPs (J):

$$J = \frac{4\pi r^2}{V_m}\frac{dr}{dt} \tag{3.7}$$

The diffusion layer of each spherical particle can be considered to be undisturbed in a homogeneous medium if the distance between particles is big enough. In this case, a single particle has a concentration gradient with spherical symmetry and the flux J of monomers diffusing through the spherical surface enclosing the particle can be described by the Fick's law:

$$J = 4\pi x^2 D\frac{dC}{dx} \tag{3.8}$$

where D is the diffusion coefficient, C is concentration, and x is a distance from the center of the particle to the surface of the sphere enclosing the particle. Assuming that J is constant for x, the integration of $C(x)$ from r to $r+\delta$ (δ is the thickness of the diffusion layer) with respect to x provides:

$$J = 4\pi D\frac{r(r+\delta)}{\delta}(C(r+\delta) - C_s) \tag{3.9}$$

C_s=$C(r)$ is the concentration at the surface of the particle. For very large values of δ, Eq. 3.9 is reduced to the following equation:

$$J = 4\pi r D(C_{bulk} - C_s) \tag{3.10}$$

where C_{bulk} is the concentration of the bulk solution. Combining Eq. 3.7 and Eq. 3.10, one can obtain:

$$\frac{dr}{dt} = \frac{V_m D}{r}(C_{bulk} - C_s) \tag{3.11}$$

This equation suggests that if C_s and C_{bulk} are constant for all particles, the growth rate of the particle is inversely proportional to its radius. In other words, the growth rate of the particles decreases as the radius increases. Hence, the size distribution of the ensemble of particles becomes narrow regardless of the initial size distribution as long as all of the particles are growing and no additional nucleation occurs.

Thus, Reiss demonstrated theoretically that diffusion-controlled growth in colloidal systems can lead to the narrowing of size distribution with time by considering the diffusion area vs. size. In this sense, the Reiss model explains the experimentally observed narrowing of the size distribution in the initial stages of the NC growth [54][57][58]. However, this model cannot explain the defocusing or Ostwald ripening stage, since it does not consider the dependence of crystal growth on the particle size and equilibrium that exists in the system between the particles and monomers responsible for the precipitation and dissolution processes.

3.2.2 Gibbs-Thomson effect on the NC growth

The Oswald ripening process of NCs can be explained in terms of the Gibbs-Thomson effect since the surface energy of the particles changes during the growth and the kinetics of crystal growth responds to this change [50]. Change in chemical potential of a spherical crystal with a radius r with respect to that of the bulk crystal can be expressed as the Gibbs-Thomson equation:

$$\Delta\mu = \frac{2\gamma V_m}{r} \tag{3.12}$$

Taking into account this equation and the equilibrium between precipitation and dissolution of NCs, the reaction rate constants for precipitation and dissolution can be written in terms of the activated complex theory as:

$$k_p = k_p^0 \exp\left(-\alpha\frac{\Delta\mu}{RT}\right) = k_p^0 \exp\left(-\alpha\frac{2\gamma V_m}{rRT}\right) \tag{3.13}$$

$$k_d = k_d^0 \exp\left((1-\alpha)\frac{\Delta\mu}{RT}\right) = k_d^0 \exp\left((1-\alpha)\frac{2\gamma V_m}{rRT}\right) \tag{3.14}$$

Here, α is the transfer coefficient, k^0 is the rate constant for the bulk crystal, and k_p and k_d are the reaction rate constants for precipitation and dissolution, respectively. The last two equations signify that the smaller the radius of the particle is, the harder it is to grow, but the easier it is to dissolve due to its higher chemical potential. This statement is controversial to the focusing mechanism where smaller crystals grow faster.

In the Reiss model, it was considered that C_s was constant for all particles which is an oversimplification and should be modified. Rewriting C_s with respect to the precipitation-dissolution equilibrium and combining this expression with Eq. 3.11, the following equation of NC growth can be obtained:

$$\frac{dr}{dt} = V_m D C_{s,eq}^0 \left(\frac{S - \exp(\frac{2\gamma V_m}{rRT})}{r + \frac{D}{k_p^0}\exp(\alpha\frac{2\gamma V_m}{rRT})}\right) \tag{3.15}$$

Here, $C^0_{s,eq}$ is the equilibrium surface concentration of the bulk crystal ($C^0_{s,eq} = \frac{k^0_d}{k^0_p}$) and S is supersaturation ($S = C_{bulk}/C^0_{s,eq}$). This equation can be further rewritten in a dimensionless form:

$$\frac{dr^*}{d\tau} = \frac{S - \exp(1/r^*)}{r^* + K\exp(\alpha/r^*)} \tag{3.16}$$

where $r^* = \frac{RT}{2\gamma V_m} r$, $\tau = \frac{R^2T^2DC^0_{s,eq}}{4\gamma^2 V_m} t$ and $K = \frac{RT}{2\gamma V_m}\frac{D}{k^0_p}$. Thus, Eq. 3.16 represents a modified version of Eq. 3.11, where both the mass transport and the reaction kinetics are considered.

Talapin et al. performed Monte Carlo simulations of the evolution of an ensemble of growing NCs during the Ostwald ripening stage using Eq. 3.16 [59]. According to their calculations, the growth of NCs in the diffusion controlled regime results in better final size distributions as compared to those grown in the reaction controlled regime. In other words, the most narrow size distributions are achieved if NC growth occurs under strong diffusion control. Moreover, it was concluded that the Ostwald ripening process takes place when the supersaturation is low and the final relative standard deviation is independent of the initial size distribution under the diffusion controlled growth. Based on their model, the authors suggested two general strategies to improve the size distribution of NCs. First, to carry out the synthesis under the diffusion controlled regime, e.g. by decreasing the diffusion or mass transfer coefficient of the system. Second, to increase the surface tension at the solvent-NC interface, e.g. by a proper choice of ligands.

3.2.3 Growth through interparticle diffusion

All previous models considered the growth of NCs in the initial stages of the reaction only through the addition of monomeric species. However, there is experimental evidence that particle coalescence or even oriented attachment can also play a role in

NC growth. Hence, the particle-particle interactions are also important during the synthesis of NCs. The group of Peng investigated the dissolution/ripening processes of CdS and CdSe NCs by analyzing the size distribution of a series of UV-Vis absorption spectra using Monte Carlo simulation [60]. Their results suggest that for a diffusion controlled process, the interparticle diffusion in addition to the well-known solution-particle diffusion might also play a big role in determining the size growth rate of NC in solution. A similar conclusion was drawn for the MnO NCs, since their experimental results revealed some contradictions to the traditional "focusing of size distribution" model [61]. In this traditional model, the focusing of the size distribution is characterized by the constant NC concentration during the particle growth, which occurs through monomer accretion from solution. However, for the systems with drastic decrease in the particle concentration during the growth process, the synthetic scheme should be different. Thus, the authors proposed a tentative alternative mechanism for the formation of monodisperse NCs ("self-focusing of the size distribution"), where the monomers are driven from small NCs to larger ones by interparticle diffusion, owing to solubility gradients between neighboring NCs (Fig. 3.2).

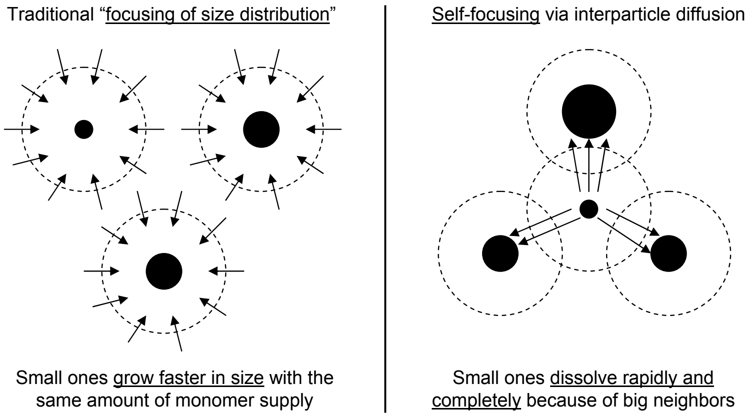

Figure 3.2: Differences between traditional focusing of size-distribution and self-focusing via interparticle diffusion [61]. The dashed circles represent the diffusion spheres for each NC. The solid arrows show the diffusion flux.

Quantitatively, the size growth rate (dr/dt) of a NC in solution under simultaneous solution-particle and interparticle diffusion is described by Eq. 3.17 [60] as:

$$\frac{dr}{dt} = 4D/d([M] - S_d) + 10D\pi q^2(S_{ave} - S_d)[P] \tag{3.17}$$

where ($[M] - S_d$) is the monomer concentration gradient between the bulk solution and a NC, ($S_{ave} - S_d$) is the mean interparticle diffusion gradient, D is the diffusion coefficient of monomers, d is the NC size, q is the radius of the diffusion sphere, and $[P]$ is the particle concentration.

Eq. 3.17 indicates that as size-dependent solubility becomes insignificant for large particles, the interparticle diffusion becomes negligible because ($S_{ave} - S_d$) approaches zero. Presumably, that is why interparticle interaction is observable in a nanosize range. To sum up, this preliminary model can explain concentration-dependent transition of dissolution to ripening [60], focusing of size distribution in ripening (which was, for example, reported by Talapin et al. [59]), and formation of a bimodal size distribution (for details concerning bimodal size distribution see Chapter 4).

3.3 Modeling of simultaneous nucleation and growth

All models of nucleation or growth discussed above took into account the assumption that nucleation is a very fast process and is followed by the growth of NCs, without overlapping of these stages. However, there are experimental results indicating that the early stages of the NC synthesis involve simultaneous nucleation, growth, and coarsening. In 2009, van Embden et al. [62] and Rempel et al. [63] independently fulfilled modeling of simultaneous nucleation and growth in colloidal solutions of NCs. After the generation of monomers from precursors, both models successfully replicate four main aspects of NC evolution observed experimentally [55][57][61]: formation of small clusters due to combination of monomers to form dimers, trimers, and larger clusters[1]; fast growth of the ensemble due to monomer depletion; the quasi-equlibrium phase, characterized by almost invariant mean size; classical Ostwald ripening of the ensemble after complete monomer depletion with an increase in NC size.

From these simulations performed on NC nucleation and growth, it may be concluded that the evolution of NCs in the liquid phase (in particular, by hot-injection technique) must process via highly reaction limited kinetics and not diffusion limited as it was commonly believed. When the process is *diffusion limited*, the reaction rate is determined by the rate at which monomers diffuse to nuclei. On the contrary, in *reaction limited* growth, the relatively low rate of reaction at the surface limits the incorporation of monomers into the particle.

To effectively model NC growth, van Embden et al. established a form of the growth rate for a single particle in the steady state that can be tuned between the reaction and diffusion limits [62]:

$$\Gamma_r = \frac{dr}{dt} = \frac{DV_m\left([C_{bulk}] - [C_{infin}]\exp\left(\frac{2\gamma V_m}{rRT}\right)]\right)}{\left(r + \frac{D}{k_r}\right)} \tag{3.18}$$

where Γ_r is the instantaneous size-dependent growth rate, $[C_{infin}]$ is the concentration of monomer in equilibrium with an infinitely flat surface, k_r is the rate constant which controls the incorporation of monomer into the particle (particle growth). Converting Eq. 3.18 into dimensionless units, the following equation can be obtained:

$$\frac{d\beta}{d\tau} = \frac{(S - \exp(1/\beta))}{(\beta + \varepsilon)} \tag{3.19}$$

where dimensionless radius (β), supersaturation (S), and time (τ) are represented as: $\beta = r\phi$, $S = \frac{[C_{bulk}]}{[C_{infin}]}$, $\tau = t\psi$ with $\phi = \frac{RT}{2\gamma V_m}$ and $\psi = \phi^2 DV_m[C_{infin}]$. ε is the ratio

---

[1] which is in agreement with the experimentally observed formation of magic-sized nanoclusters (for details see Chapter 5).

of diffusion to reaction rates and is given by the dimensionless Damköler number: $\varepsilon = \frac{D\phi}{k_r}$. If $k_r \ll d$, then $\varepsilon \ll 1$ and the growth kinetics is reaction limited, if $\varepsilon \gg 1$, the process is diffusion limited.

The authors varied the value ε to study the growth kinetics both under diffusion and reaction limited conditions and found a time scale of the simulation and experiment to be similar under reaction limited process. The simulation has also shown that under reaction control the full width at half-maximum (fwhm) remains constant at early reaction times, whereas for the diffusion limited case, the fwhm narrows during the early stages of NC growth. The fact of narrowing may be a contributing factor to the misinterpretation that NC growth proceeds under diffusion limited kinetics. This model does not include the particle-particle interactions operating through a mean diffusion field, however, the authors expect that under reaction limited conditions, it would not influence the growth significantly. Similarly, Rempel et al. [63] noticed that the diffusion limited growth rate estimated from their model was several orders of magnitude higher than those observed experimentally, putting into question the validity of this hypothesis. Additionally, their model showed that focusing can be achieved under pure reaction control in the absence of diffusion limitation. Thus, both models predicted similar reaction stages in good agreement with experiment, and contrary to the common understanding revealed that the growth of monodisperse NCs takes place under reaction limited conditions.

Chapter 4

Investigation of growth kinetics of CdSe nanocrystals

This chapter presents a new synthetic route for the formation of high quality zinc blende CdSe colloidal quantum dots (QDs). The synthesis was carried out using *in situ* formed Cd^0 particles as a Cd precursor[1] and Se dissolved in tri-n-octylphosphine (TOP), tri-n-butylphosphine (TBP), or 1-octadecene (ODE) as a Se precursor. The preparation of the Se/ODE solution was found to be crucial to obtain a Se precursor with an activity comparable with TOPSe and TBPSe. The reactions with different Cd : Se ratio (1 : 0.2, 1 : 0.4, 1 : 0.8, 1 : 1, and 1 : 2) and oleic acid (OA) concentrations (200, 300, and 400 µl) have been investigated to observe the changes in reaction kinetics and to optimize the synthesis conditions. A variety of techniques such as UV-Vis absorption and photoluminescence (PL) spectroscopy, powder X-ray diffraction (XRD), nuclear magnetic resonance (NMR) spectroscopy, two-dimensional correlation NMR spectroscopy (COSY), mass spectrometry (MS), atomic absorption

---

[1] The term “precursor” is used to indicate the species containing Cd or Se prior to the hot-injection [64].

spectroscopy (AAS), energy-dispersive X-ray analysis (EDX), thermal gravimetric analysis (TGA), transmission electron microscopy (TEM), and high resolution TEM (HRTEM) were used to carry out structural and spectroscopic characterizations of the CdSe nanoparticles as well as the Cd and Se precursors.

4.1 Motivation and review of the literature

The synthesis of colloidal semiconductor nanocrystals (NCs) has been a rapidly developing research area in recent years with a particular emphasis on II-VI semiconductor systems such as CdSe [65][66][67]. This work has led to significant improvements in particle size tunability, size homogeneity, reproducibility, production of particles with high luminescence quantum yields, adjustment of surface and electronic properties, as well as reduction of environmental hazards and safety problems. Nevertheless, further improvements in material quality and monodispersity are still possible and desirable in all of these areas (viz. for improvement in the performance of NC-based devices). More importantly, continued research on the synthesis of CdSe NCs will yield a more complete understanding of this important model system, and this improved understanding will form the basis for synthetic optimization of a broader range of semiconductor NCs.

There are many different methods of nanoparticles synthesis which can be broadly classified into two categories: top-down approach and bottom-up approach. In the top-down approach, one starts with a macroscopic piece of material out of which a nanostructure device is made, whereas in the bottom-up approach, quantum dots are made by growing, for instance, semiconductor NCs as colloidal particles starting from molecular precursors. In the 1980s, CdSe QDs were prepared mainly by top-down techniques (for example, lithography). However, several disadvantages such as size variations, crystal defects, poor reproducibility, and poor optical properties of these

QDs made them unsuitable for advanced applications. Introduction of bottom-up synthesis of CdSe QDs in the 1990s brought remarkable changes in the properties and applications of semiconductor NCs. The bottom-up approach can be divided in turn into two groups: gas-phase synthesis and liquid-phase synthesis. Although gas-phase synthesis methods can produce large quantities of nanoparticles, they are not applicable to the synthesis of high quality NCs sizing between 1 and 10 nm due to agglomeration and non-uniformity of particles size and shape. These problems can be avoided using various liquid-phase synthetic routs which allow to produce nearly monodisperse and unagglomerated NCs.

In this thesis, we will consider the methods of CdSe NCs synthesis in solution and, in particular, in organic medium since the quality of nanocrystals resulting from low-temperature aqueous-based synthetic methods is not as good as that obtained from the high-temperature organic-based methods.

Originally, the synthesis of high quality semiconductor NCs CdE (E = S, Se, Te) was developed by Murray and colleagues in 1993 [51], based in a large part on earlier studies of CdSe particles conducted by groups of Brus [68][69] and Steigerwald [70], as well as the studies of CdS nanoparticles by Henglein [71] and Spanhel et al. [72], who together supplied the fundamental principles concerning synthesis, as well as the understanding of electronic structure of semiconductor nanoparticles. Murray et al. produced colloidal suspensions of II-VI semiconductor nanocrystals (CdS, CdSe, and CdTe QDs) passivated with tri-n-octylphosphine oxide (TOPO) via an organometallic precursor route, which involved the reaction of cadmium organometallic precursor $Cd(CH_3)_2$ with a chalcogenide precursor: bis(trimethylsilyl) chalcogenide $(TMS)_2E$ (E = S, Se, Te) or TOPSe and TOPTe. In the case of CdSe NCs, $Cd(CH_3)_2$ and TOPSe were rapidly injected into hot TOPO (at 300 °C) in an atmosphere of argon to produce a short burst of homogeneous nucleation. The growth of CdSe QDs was carried out at ca. 230-260 °C. This method provided good quality CdSe nanoparticles with a bright luminescence and clearly resolved optical transitions. The synthesized crystalline nanoparticles that ranged from 1.2 to 11.5 nm exhibited a wurtzite structure. The different sizes were separated by size-selective precipitation[2] from a mixture of 1-butanol and methanol.

In 1994, Alivisatos and co-workers [73] markedly improved the colloidal synthesis of CdSe QDs, proposed by Murray et al. They replaced trioctylphosphine (TOP) with tributylphosphine (TBP), increased the injection temperature to 350 ℃, and minimized Ostwald ripening by separating the spontaneous nucleation process from the relatively slow nanocrystal growth process. Thus, the group of Alivisatos found out that by selection of the injection and growth temperatures, one can produce good quality NCs avoiding time-consuming size-selective precipitation.

In 1996, Trindade and O'Brien modified the Murray's method substituting $Cd(CH_3)_2$ and TOPSe with a single-source molecular precursor (i.e. $[CH_3CdSe_2CN(C_2H_5)_2]_2$) [74][75], which would act as a precursor simultaneously for both Cd and Se and would bring about the formation of CdSe nanoparticles during the thermolysis of these precursors in TOP/TOPO. However, the produced nanoparticles were not of excellent quality (poor size and shape distribution, as well as poor luminescence properties), which explains why their approach was not widely used further.

Thus, the synthesis of CdSe nanocrystals through the organometallic route originally developed by Murray and colleagues had led the synthesis of high quality semiconductor nanocrystals for several years. However, it is generally acknowledged that $Cd(CH_3)_2$ is expensive, extremely hazardous, unstable at room temperature, and explosive at elevated temperatures by releasing a large amount of gas material. Due to these reasons, the $Cd(CH_3)_2$-related schemes require very restricted equipment

---

[2] The size-selective precipitation is based on the fact that on the addition of a non-solvent to the colloidal solution of nanocrystals, the largest particles are the first to precipitate due to the stronger van der Waals interactions. Using this procedure it makes possible to obtain initial solid fractions richer in larger particles as compared with the later fractions.

and conditions and are not suitable for large-scale synthesis. In 2000, Peng et al. [76] described a much simpler and safer nonorganometallic precursor route to produce CdSe QDs (as well as CdS and CdTe QDs) using inexpensive and little toxic cadmium oxide CdO (or also cadmium acetate $Cd(OAc)_2$ ($OAc = O_2CCH_3$) [77] and cadmium carbonate $CdCO_3$ [78]) instead of $Cd(CH_3)_2$ together with hexylphosphonic acid (HPA) or tetradecylphosphonic acid (TDPA), which led to the intermediate formation of a cadmium HPA/TDPA complex. By injecting selenium that is dissolved in trioctylphosphine or tributylphosphine, this approach is safer and yields nearly monodisperse quantum dots without a need for post-reaction size sorting. As a high-boiling-point solvent, technical grade tri-n-octylphosphine oxide (TOPO) is used for this procedure. The authors managed to synthesize a broad range of the NCs sizes (from 1.5 to 25 nm) and controllably vary the crystal structure (from zinc blende to wurtzite) using different synthetic schemes. A major drawback of the latter method, however, is that it renders small NCs (between 2 and 4 nm) together with relatively large-sized CdSe NCs (4-25 nm) because of low nucleation yield and rapid growth. Thus, the reaction cannot be quenched quickly and reproducibly enough to isolate small, monodisperse particles.

More recently, it has been demonstrated that less hazardous noncoordinating solvents such as octadecene (ODE) can be used instead of coordinating solvents such as trioctylphosphine oxide (TOPO) [52]. ODE has significant design advantages in the preparation of nanocrystals because it allows the reactivity and nucleation rate of precursor monomers to be tuned by diluting the coordinating ligands present in a solution. Thus, the use of ODE enables systematic investigations of the effects of different precursors on the nucleation and growth of nanocrystals to be carried out. Furthermore, ODE is a liquid at room temperature rather than a solid as many coordinating solvents are, thereby contributing to the excellent processability of this synthetic system. Yu et al. [52] reported that with ODE as a noncoordinating solvent and an appropriate amount of oleic acid as a ligand, the size of CdSe NCs can range from approx. 1.5 to 20 nm in a controllable fashion. The group of Mulvaney (Bullen [58] and van Embden [55]) investigated nucleation and growth kinetics of CdSe NCs nucleated from TOPSe and cadmium oleate in ODE. They showed that the capping agent oleic acid (OA) can be used to tune the activity of the dissolved metal during synthesis of colloidal CdSe particles, hence, it influences the primary nucleation steps during the formation and growth process of CdSe NCs. Although this method yields quasi monodisperse nanoparticles, some improvements of the synthesis are still possible and desirable in order to avoid fast depletion of the monomer in solution and therefore produce nanoparticles with even better characteristics.

In general, the formation of monodisperse nanoparticles nuclei is successful at high temperatures. Thus, a hot injection technique method involving the injection of a "cold" (room temperature) solution of precursor molecules into hot liquid (120-350 ℃) has become one of the most successful methods for the synthesis of high quality II-VI nanocrystals [51][77][65][67]. However, in a usual synthesis of nanoparticles by the hot injection technique, the concentration of the monomers[3] in solution decreases during the growth of nanoparticles. Consequently, the growth conditions of the particles change continuously during the synthesis, leading at long reaction times to a broadening of the size distribution or to a change of nanoparticles shape from elongated or branched to spherical. Finding a way to assure a constant monomer concentration during the whole reaction could improve the quality of synthesized nanoparticles and enhance the control over the results of the synthesis. A possible way to achieve a quasi constant monomer supply at least in the beginning of the reaction is the use of high initial monomer concentrations. It has been demonstrated, both experimentally and

---

[3] The term "monomer" means in this context the same as the term "cationic monomer" proposed by Peng et al. and refers to all cadmium species in a solution that are not in the form of nanocrystals [79][52].

theoretically [65][59], that high precursor concentrations are important in achieving fast size focusing and slow defocusing, which are the key factors for a narrow size distribution of the fabricated NCs. A drawback of this method is that the concentration of the monomers has an influence on the size and shape of the synthesized particles. Another possible way is the use of a precursor system consisting of a monomer in the solution that stays in equilibrium with a solid and big enough surface for ensuring a constant monomer supply when required. The depletion of monomers in the solution can be avoided in this way, and therefore fast size focusing and slow defocusing are provided, which results in the production of high quality NCs.

In this work, a new synthetic method for CdSe QDs is suggested, based on the previously reported by Kolny-Olesiak et al. synthesis for CdTe, where *in situ* formed Cd^0 particles are used as a Cd precursor [39][40]. The Cd^0 particles regulate the monomer supply for the growth of CdSe NPs and therefore influence the reaction kinetics allowing to obtain monodisperse quantum dots.

Usually, the reaction media in a hot injection synthesis involve at least three components, namely, the solvent (TOPO or ODE), the Cd precursor solution, and the Se precursor solution (TOPSe or TBPSe). The costs of large-scale NCs synthesis are very high for using expensive substances such as TOP (or TBP). In addition, TOP (or TBP) is hazardous, unstable, and not an environmentally friendly solvent. In 2005, Deng et al. synthesized zinc blende CdSe NCs via “non-TOP-based route” involving Se powder dissolved in paraffin liquid as a Se precursor, which is reduced to H_2Se gas [80]. H_2Se then reacts with $Cd(OA)_2$ to form CdSe NCs. A drawback of this method is, however, the high toxicity of gaseous H_2Se, which makes this method inappropriate for the large-scale synthesis. The photoluminescence (PL) full width at half-maximum (fwhm) of as-prepared CdSe nanocrystals was in the range of 29 to 48 nm and controlled size from 2 to 5 nm. Almost simultaneously, Sapra et al. developed the synthesis of CdSe nanoparticles using Se powder dissolved in olive oil [81];

however, their particles were not of the best monodispersity. Jasieniak and colleagues reported the development of a nonorganometallic phosphine-free selenium precursor that comprises a homogeneous solution of selenium dissolved in ODE [82], analogous to the sulfur dispersion reported by Yu et al. [52]. They have also demonstrated that TOP does influence the kinetics of CdSe formation, but it does not introduce any additional nonradiative surface states. This synthetic approach allows to tune the nucleation and growth of CdSe by altering the reactivity of selenium and to probe more clearly the role of the chalcogenide precursor in the CdSe nanocrystal synthesis, as well as the role of an alkylphosphine (TOP) in surface passivation. Although a Se/ODE precursor has been successfully used in the synthesis of CdSe NCs, the chemical interactions occurring in this Se precursor solution during its reparation have not been investigated. To our knowledge, there is no information in the literature about chemical bonds between Se and ODE during its heating at 200 ℃ for 2 hours, which makes the solution to exhibit the reactivity comparable with the more common Se precursors – TOPSe and TBPSe. This motivated us to investigate the nature of the Se/ODE solution by means of different analytical methods in detail. Moreover, the quality of as-prepared CdSe nanocrystals with phosphine-free techniques could still not reach the level of widely used selenium phosphine methods. This drawback can be eliminated in the reaction with *in situ* formed Cd^0 particles as a Cd precursor, which was achieved in the present study.

4.2 Results and discussion

In the first step, the formation of the Cd and Se precursors was studied. Then the influence of various parameters such as Cd to Se ratio ($1:0.2$, $1:0.4$, $1:0.8$, $1:1$, and $1:2$), a type of Se precursor solution (TOPSe, TBPSe, and Se/ODE), and different amount of oleic acid (OA) (200, 300, and 400 µl) on the formation of nanoparticles was investigated. The reactions were monitored by UV-Vis absorption spectroscopy and photoluminescence (PL) spectroscopy. The wavelength of the first excitonic absorption peak was utilized to calculate the mean diameter and concentration of the obtained CdSe NCs by the empirical fitting function presented by Peng's group [42]. The half-width at half-maximum (hwhm)[4] on the longer wavelength side of the first maximum of the absorption spectra was taken as a measure of a size distribution of the samples.

4.2.1 Cd precursor: formation of Cd^0 particles

The synthesis of CdSe NCs in our work can be divided in two steps: the formation of Cd^0 particles and the growth of CdSe QDs. First, CdO dissolves in the mixture of ODE and OA, forming cadmium oleate Cd(OA)$_2$. ODE has several advantages which

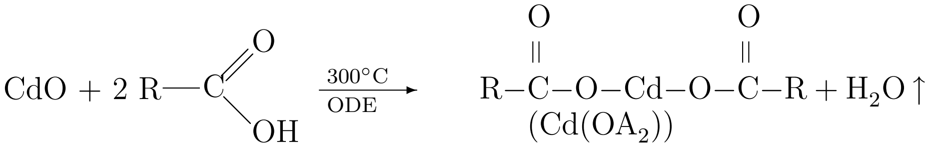

$$\mathrm{CdO} + 2\,\mathrm{R{-}C({=}O)OH} \xrightarrow[\mathrm{ODE}]{300^\circ\mathrm{C}} \underset{(\mathrm{Cd(OA_2)})}{\mathrm{R{-}\overset{\overset{\displaystyle O}{\|}}{C}{-}O{-}Cd{-}O{-}\overset{\overset{\displaystyle O}{\|}}{C}{-}R}} + \mathrm{H_2O}\uparrow$$

make it an ideal solvent for the growth of high quality NCs. First, a relatively low melting point (below 20 ℃) enables easy handling at room temperature. Second, its relatively high boiling point (above 320 ℃) allows to perform the synthesis at high temperatures. Third, it is inexpensive and has a low toxicity level. Finally, it exhibits low reactivity to precursors and excellent dissolving power for many compounds at elevated temperatures. OA was used as a ligand for its excellent performance in

---

[4] The half-width at half-maximum (hwhm) of the absorption spectra and full-width at half-maximum (fwhm) of the PL spectra are usually used as a guide to measure the quality of nanocrystals because they reflect their size distribution; a narrow hwhm or fwhm means a narrow size distribution of the particles.

surface capping of the CdSe NCs leading to the formation of nearly monodisperse QDs. During further heating of $Cd(OA)_2$ solution to 300 ℃, metallic Cd^0 particles are formed due to a partial decomposition of the $Cd(OA)_2$ [83].

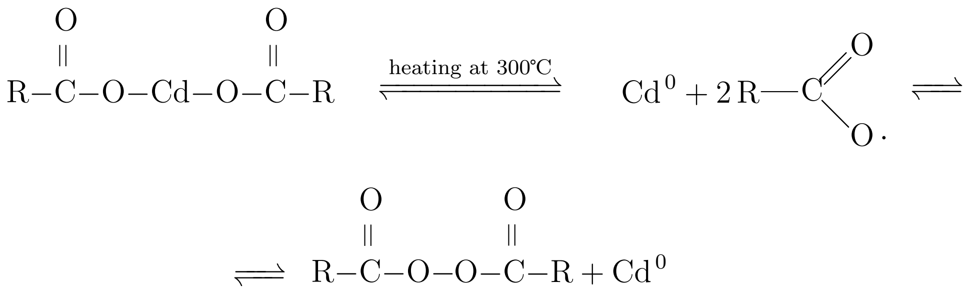

These Cd^0 particles are crystalline and have sizes between 100 and 150 nm. The colloidal solutions of the synthesized NCs should be centrifugated in order to separate the precipitate. The presence of oleate peroxide (ROO-OOR) in fresh crude solutions of CdSe QDs was proved by mass-spectrometry measurements. However, in older solutions (3-6 month), this compound is no longer present due to its instability. In the second stage of the reaction, during the formation of CdSe particles, Cd^0 particles regulate the monomer supply for the growth of the QDs and therefore influence the reaction kinetics.

$$\mathrm{Cd}^0 \overset{-2e}{\rightleftharpoons} \mathrm{Cd}^{2+}$$

$$\mathrm{Cd(OA)_2} + \mathrm{Se{-}precursor} \longrightarrow \text{CdSe QDs (stabilized with OA ligands)}$$

Mass-spectrometry analysis of the crude CdSe NC solutions revealed the presence of TOPO and unreacted TOPSe molecules.

Both reactions with and without Cd^0 formation [58] yield spherical particles. According to the absorption spectra of the crude solutions, the particles formed in the first case are highly monodisperse (Fig. 4.1), since a constant monomer supply by the Cd^0 particles provides better growth conditions resulting in samples with a narrow size distribution. The absorption spectra show the presence of up to four excitonic transitions, and the shift of the absorbance to longer wavelength with the increase in the particle size implies the quantum confinement effect in these nanoparticles.

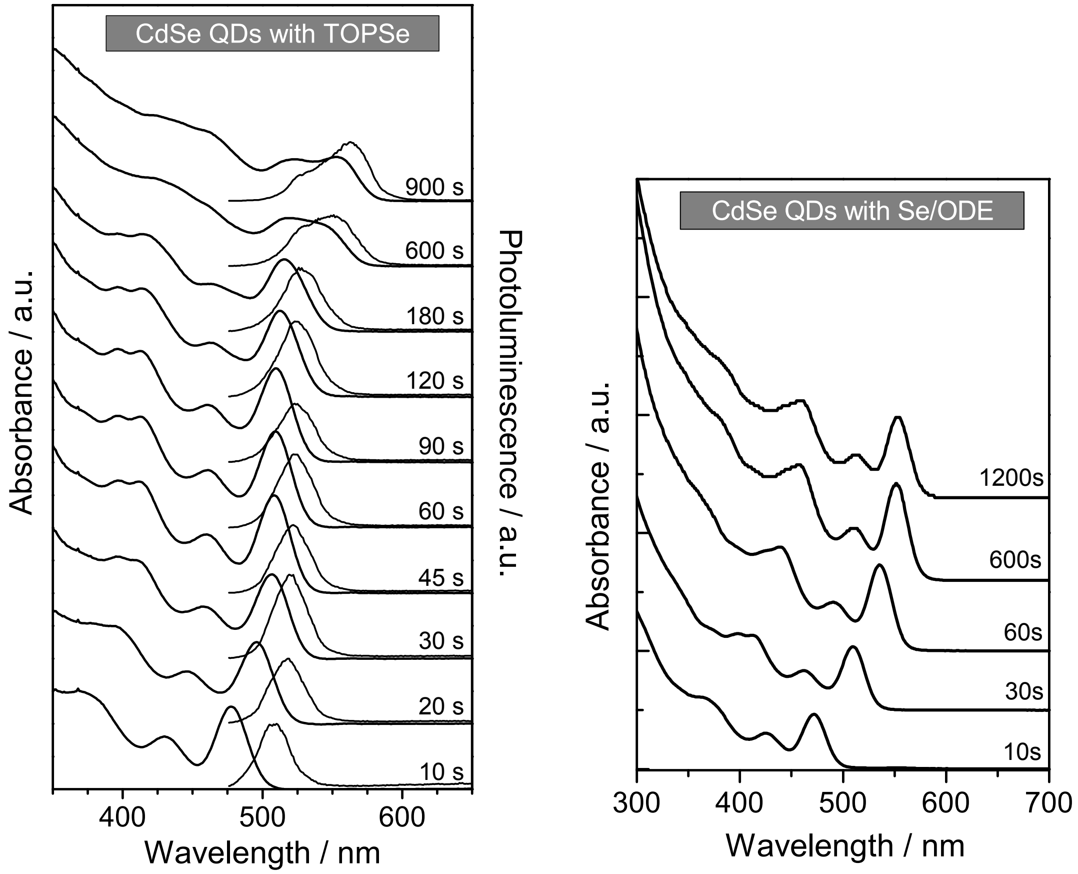

(a) (b)

Figure 4.1: Representative UV-Vis absorption and PL spectra of differently sized CdSe QDs prepared by the method described in this thesis: (a) UV-Vis and PL spectra of CdSe QDs synthesized with TOPSe; (b) UV-Vis spectra of CdSe QDs synthesized with Se/ODE. The spectra were collected after different reaction times indicated at the curves.

4.2.2 Se precursors: TOPSe, TBPSe, and Se/ODE

Three different Se precursors were used: TOPSe, TBPSe, and Se/ODE. Elemental Se can be dissolved both in TOP and TBP, as well as in ODE. In TOP and TBP, Se is dispersed molecularly and forms TOPSe or TBPSe, respectively [84]. Both TOPSe and TBPSe are widely used in the synthesis of CdSe QDs, and their reactions with different cadmium monomers have already been studied in detail. Although Se/ODE has been successfully used in the CdSe synthesis [82][85], the exact nature of this Se precursor has not yet been studied. In the present thesis, the nature of the Se/ODE precursor was investigated in detail by means of mass spectrometry (MS), ^{1}H and ^{13}C nuclear magnetic resonance (NMR) spectroscopy, as well as ^{1}H-^{1}H and ^{1}H-^{13}C correlation NMR spectroscopy (COSY).

Investigation of chemical composition of the Se/ODE precursor

It has been reported that heating Se with ODE results in thermal dissolution of crystalline selenium powder into its various allotropes [81], however, no experimental results have been shown to support this assumption. The preparation of the Se solution in ODE seems to be crucial to obtain a Se precursor with an activity comparable with TOPSe and TBPSe. The reactivity of the Se precursor solution in reaction with $Cd(OA)_2$ depends on how long the Se/ODE solution was heated. It was observed that while the reactivity of the Se precursor heated for 2 hours in ODE is comparable to the reactivity of TOPSe and TBPSe precursor solutions, Se/ODE solution that is not heated long enough (less than 2 hours) results in much lower activity. Thus, using the latter Se precursor (Se/ODE solution heated for 1 hour) also results in CdSe formation, but the seed formation starts only after heating the reaction mixture for about 1 hour. Nanoparticles synthesized by this method have lower concentrations compared to the analogous reactions with other Se precursors (TOPSe, TBPSe, or Se/ODE heated for 2 hours). On the contrary, heating the Se/ODE precursor solution for more than 4 hours results in polymerization of Se [82]. Moreover, the concentration of the Se/ODE precursor solution during its preparation was found to play a big role in its activity. In other words, a little amount of Se dissolved in ODE produced a Se precursor that could not form highly monodisperse NCs. Differently, using the Se/ODE solution with initial higher concentration resulted in good quality CdSe QDs. Thus, a comparison of 0.18 M and 0.04 M solutions revealed that the 0.18 M solution was more reactive and led to the formation of CdSe NCs with several absorption features in the UV-Vis spectra, and was therefore as good as with TOPSe and TBPSe precursors. Unlike 0.18 M solution, the 0.04 M solution yielded the nanoparticles with worse absorption characteristics, smaller concentrations, and later seed formation (in 30-90 s after the injection).

The strong dependence of the results of the reaction on the way of the Se/ODE precursor preparation motivated us to characterize the Se/ODE solution in detail. The dissolution process of Se in ODE was investigated by taking aliquots every 10 min and examining them by mass spectrometry (MS), ^{1}H and ^{13}C NMR spectroscopy, as well as two-dimentional ^{1}H-^{1}H, ^{1}H-^{13}C correlation NMR spectroscopy (COSY). During preparation of the Se precursor solution in ODE, its color changed from light red to canary yellow. Cooling down the red colored solution results in formation of a red selenium precipitate. Red selenium is composed of rings of 8 and more Se atoms. These selenium species or any other pure Se_x molecules cannot be found in the remaining yellow solution. It contains only Se-ODE adducts. During the heating process, some of the ODE molecules polymerize to form dimers, trimers, and tetramers (Fig. 4.2a). In the mass spectra of the studied Se/ODE aliquots, peaks corresponding to ODE$-$Se, ODE$-$Se$_2$, ODE$_2-$Se, ODE$_2-$Se$_2$, ODE$_3-$Se, ODE$_3-$Se$_2$, and ODE$_3-$Se$_3$, as well as their decomposition products can be found (Fig. 4.2b).

The nature of these ODE-Se adducts as well as pure ODE was studied using NMR spectroscopy. Several solutions, viz. ODE before and after heating (under nitrogen conditions), the Se precursor used for the synthesis (0.18 M Se in ODE heated for 2 hours), and a highly concentrated 1.5 M Se in ODE solution, were compared. The ^{1}H and ^{13}C NMR spectra of pure ODE changed after heating due to partial polymerization, which could also be detected with MS. In the ^{1}H and ^{13}C NMR (Fig. 4.3c,

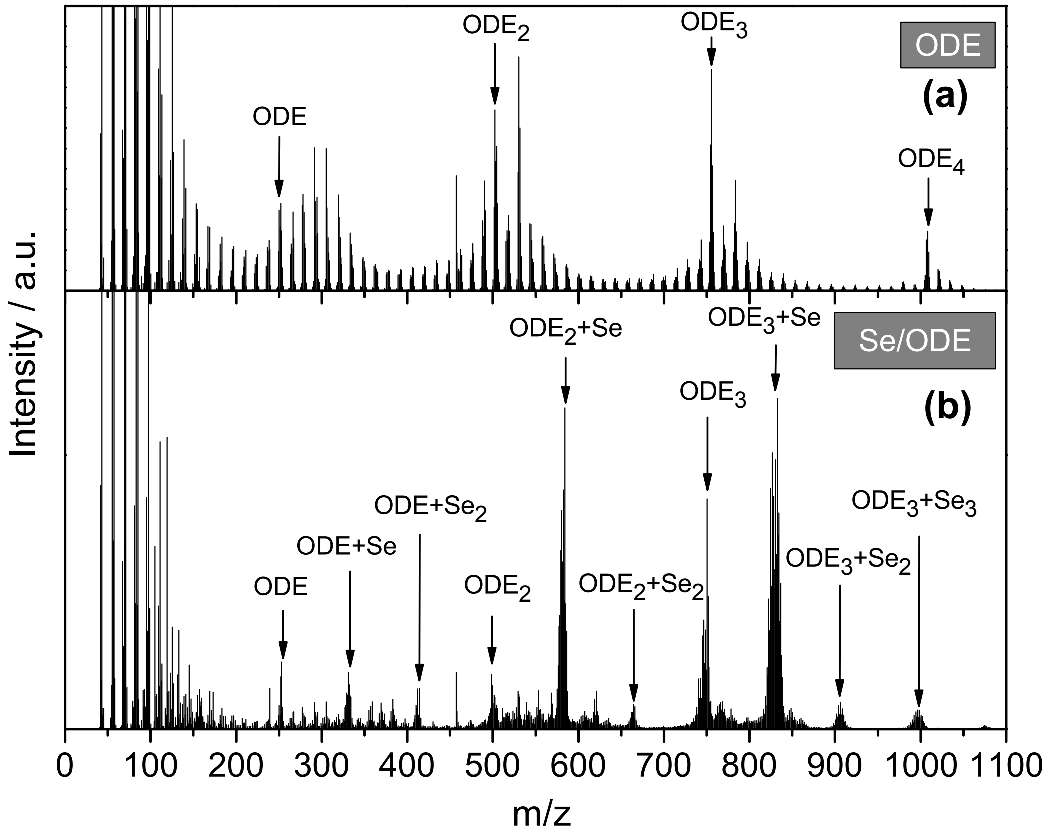

Figure 4.2: MS spectra of (a) heated under N_2 ODE; (b) 1.5 M solution of Se/ODE.

d) as well as in the ^{1}H-^{1}H and ^{1}H-^{13}C COSY spectra of the solution containing Se (Fig. 4.4b and not shown, respectively), several additional signals could be found that did not occur in pure ODE after heating (Fig. 4.3a, b and Fig. 4.4a). Due to considerable changes in the ^{1}H and ^{13}C NMR spectra of Se/ODE (Fig. 4.3c, d) in comparison to heated ODE, one can conclude that the reaction of dissolution of Se powder in ODE brings about the formation of covalent bonds between Se and ODE molecules. Obviously, Se reacts with the double bond of ODE, since in a comparable experiment with octadecane (ODA) instead of ODE, dissolution of Se could not be observed. Additionally, two peaks in the ^{1}H NMR spectrum of ODE at 4.96 and 5.79 ppm corresponding to the double bound disappear in the Se/ODE solution, and instead only one signal at 5.39 ppm can be observed. This indicates that the double bond is likely to have moved to another position in the ODE molecule, so that the

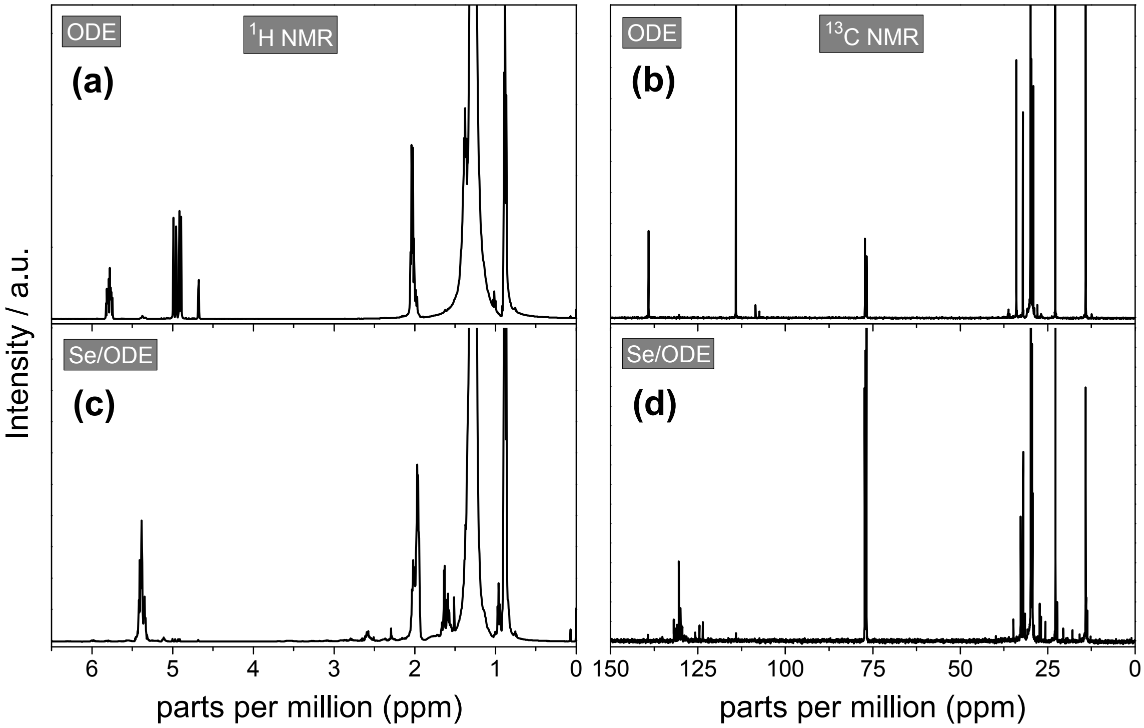

Figure 4.3: ^{1}H and ^{13}C NMR spectra of (a, b) heated under N_2 ODE; (c, d) 1.5 M solution of Se/ODE, respectively.

hydrogen atoms at both sides of the double bond are equivalent and give the only signal. Moreover, the peak at 1.64 ppm appears in the Se/ODE solution which is not present in pure ODE. From the ^{1}H-^{1}H COSY spectrum, it is possible to obtain the information about coupling of protons, evidenced by appearance of cross-signals. Fig. 4.4b depicts the ^{1}H-^{1}H COSY spectrum of 1.5 M Se/ODE solution, and it is obvious that the hydrogen atom at 1.64 ppm is coupled to the hydrogen atoms at 2.59 and 5.39 ppm. These signals are not present in the ^{1}H-^{1}H COSY spectrum of ODE (Fig. 4.4a) indicating a new coupling structure in the Se/ODE solution. The observing of the coupling between these protons shows that they are located close to each other (maximum two or three bonds apart). The signal at 2.59 ppm can be assigned to the hydrogen atoms in the direct neighborhood of selenium atom(s). A similar investigation was done in reference [86] where a signal at 2.5 ppm in the ^{1}H NMR spectrum was observed both in diethyl selenide $CH_3{-}CH_2{-}Se{-}CH_2{-}CH_3$

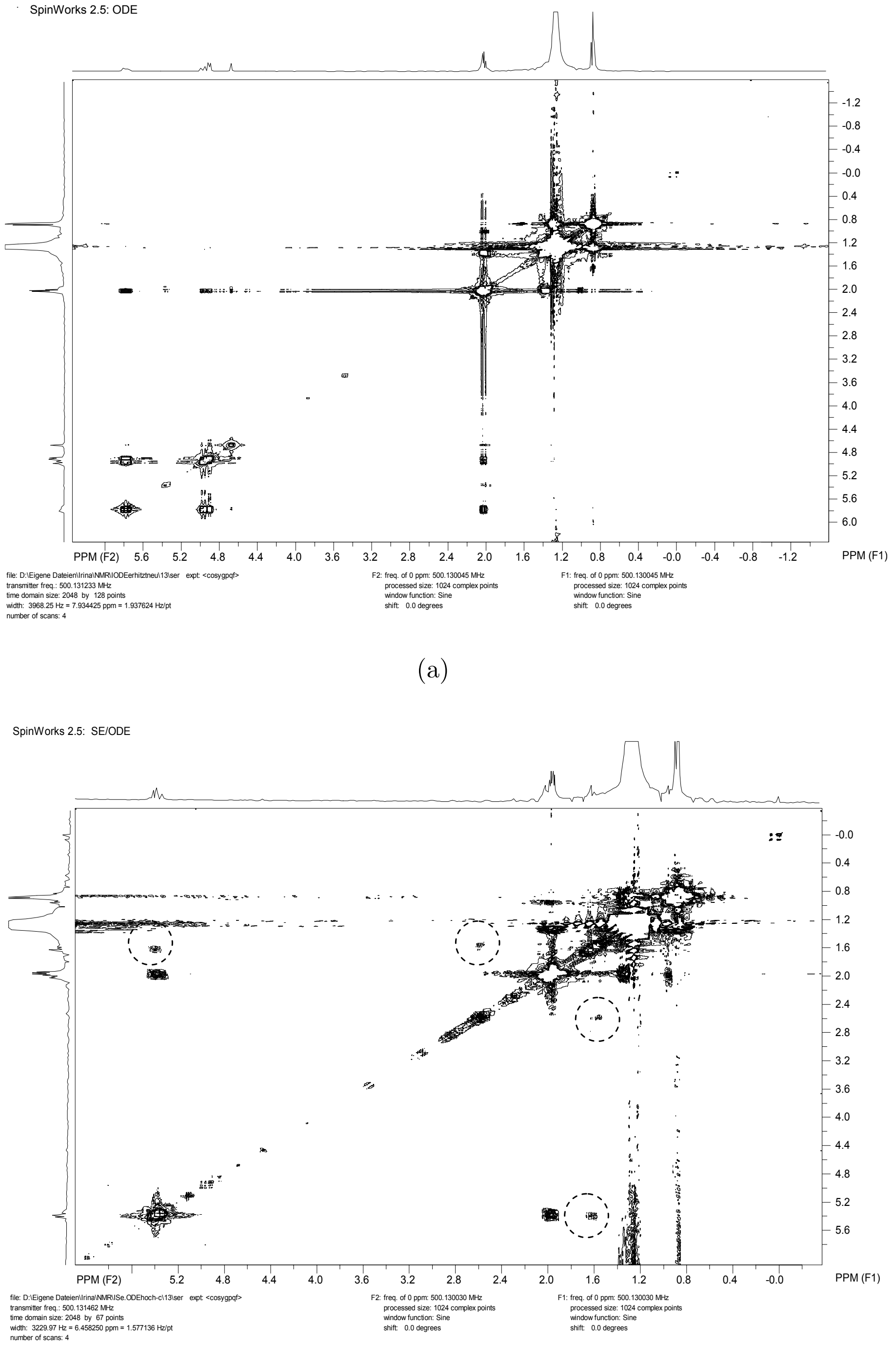

```
file: D:\Eigene Dateien\Irina\NMR\IODEerhitztneu\13\ser   expt: <cosygpqf>
transmitter freq.: 500.131233 MHz
time domain size: 2048  by  128 points
width:  3968.25 Hz = 7.934425 ppm = 1.937624 Hz/pt
number of scans: 4

F2: freq. of 0 ppm: 500.130045 MHz
    processed size: 1024 complex points
    window function: Sine
    shift:   0.0 degrees

F1: freq. of 0 ppm: 500.130045 MHz
    processed size: 1024 complex points
    window function: Sine
    shift:   0.0 degrees
```

(a)

```
file: D:\Eigene Dateien\Irina\NMR\ISe.ODEhoch-c\13\ser   expt: <cosygpqf>
transmitter freq.: 500.131462 MHz
time domain size: 2048  by  67 points
width:  3229.97 Hz = 6.458250 ppm = 1.577136 Hz/pt
number of scans: 4

F2: freq. of 0 ppm: 500.130030 MHz
    processed size: 1024 complex points
    window function: Sine
    shift:   0.0 degrees

F1: freq. of 0 ppm: 500.130030 MHz
    processed size: 1024 complex points
    window function: Sine
    shift:   0.0 degrees
```

(b)

Figure 4.4: ^{1}H-^{1}H COSY spectra of (a) heated under N_2 ODE; (b) 1.5 M solution of Se/ODE. The dashed circles highlight new coupling signals in Se/ODE in comparison to pure ODE.

and dimethyl diselenide $CH_3-Se-Se-CH_3$. Thus, the signal at 1.64 ppm is likely to represent the hydrogen atoms between the end hydrogen atoms close to selenium atom(s) (2.59 ppm) and the double bond (5.39 ppm).

The ^{13}C NMR spectrum also shows significant changes in the Se/ODE precursor (Fig. 4.3d) as compared to the ODE solution (Fig. 4.3b), evidenced by several new signals. In particular, the signals between 120 and 140 ppm which can be assigned to the carbon atoms forming the double bond are different for the Se/ODE and ODE solutions. This confirms the conclusion drawn from the ^{1}H NMR spectrum that interaction of Se with ODE does not result in complete disappearance of the double bond, but due to formation of new bonds with selenium, the double bond is shifted. This shift can take place in different positions in the ODE molecule because of the presence of several new signals in the 120-140 ppm region of the ^{13}C NMR spectrum of the Se/ODE solution.

4.2.3 Investigation of growth kinetics of CdSe QDs

Admittedly, many factors influence a colloidochemical synthesis of NCs. Among them are the nature and concentration of the initial materials (precursors), the stabilizer that prevents the colloids from agglomerating or further growing, the solvent, the reaction time, the temperature, and the atmosphere, etc. Adjustment of these parameters is of utmost importance for production of high quality NCs with desirable properties. In the present study, reactions with different initial conditions were investigated to observe the changes in the reaction kinetics and to optimize the synthesis conditions. It should be noted that increasing the OA concentration from 200 to 400 µl leads to the longer times of the formation of Cd^0 precipitate. Consequently, adding more than 400 µl of OA would be unpractical due to big time consumption. The growth dynamics of CdSe nanocrystals was monitored by removing samples from the reaction mixture at different instants of time. For every sample, absorption spectra were measured and diameters, concentrations, total volumes (concentration multiplied by the volume of one particle), growth rates (increment in the nanoparticle's volume in a certain time period), and half-width at half-maximum (hwhm) were calculated and plotted (Fig. 4.5 and Fig. 4.6) (hwhm is depicted a bit later).

Figure 4.1a shows the UV-Vis absorption and photoluminescence spectra of several samples of CdSe QDs with different particle sizes obtained using TOPSe as a Se precursor. Absorption spectra of the particles synthesized with Se/ODE as a Se precursor are represented in Figure 4.1b. This set of data demonstrates the wide tunability of a particle size that is possible using OA as a capping ligand. The narrow absorption and emission peaks in these samples attest to the nearly monodisperse size distribution within the individual samples.

The method described in the present thesis provides three different means to control particle size. First, changes in growth time allow for adjustments of particle size with longer times favoring larger particles. However, after some time, the growth stops and the broadening of the absorption spectra can occur. Second, the Cd : Se precursor molar ratio also affects the size of the resulting particles, although in some reactions with different Cd : Se ratio, the QDs of the same size could be obtained. Third, the use of different Se precursors influences the diameters of the nanoparticles during the synthesis. Thus, it was noticed that the biggest CdSe nanoparticles can be obtained with TBPSe. The effect of the OA amount used in the synthesis on the size of the produced nanocrystals was not easy to observe due to the complicated influence of OA on the reaction kinetics in the presence of Cd^0 nanoparticles (see page 61). The injection temperature was not varied in the present work and was always 300 ℃. The growth temperature was set at 280 ℃, since it is generally acknowledged that the growth should take place at a bit lower temperature than the injection in order to obtain more monodisperse NCs. This is connected with the fact that the injection of the precursor(s) at 300 ℃ results in quick formation of relatively monodisperse nuclei

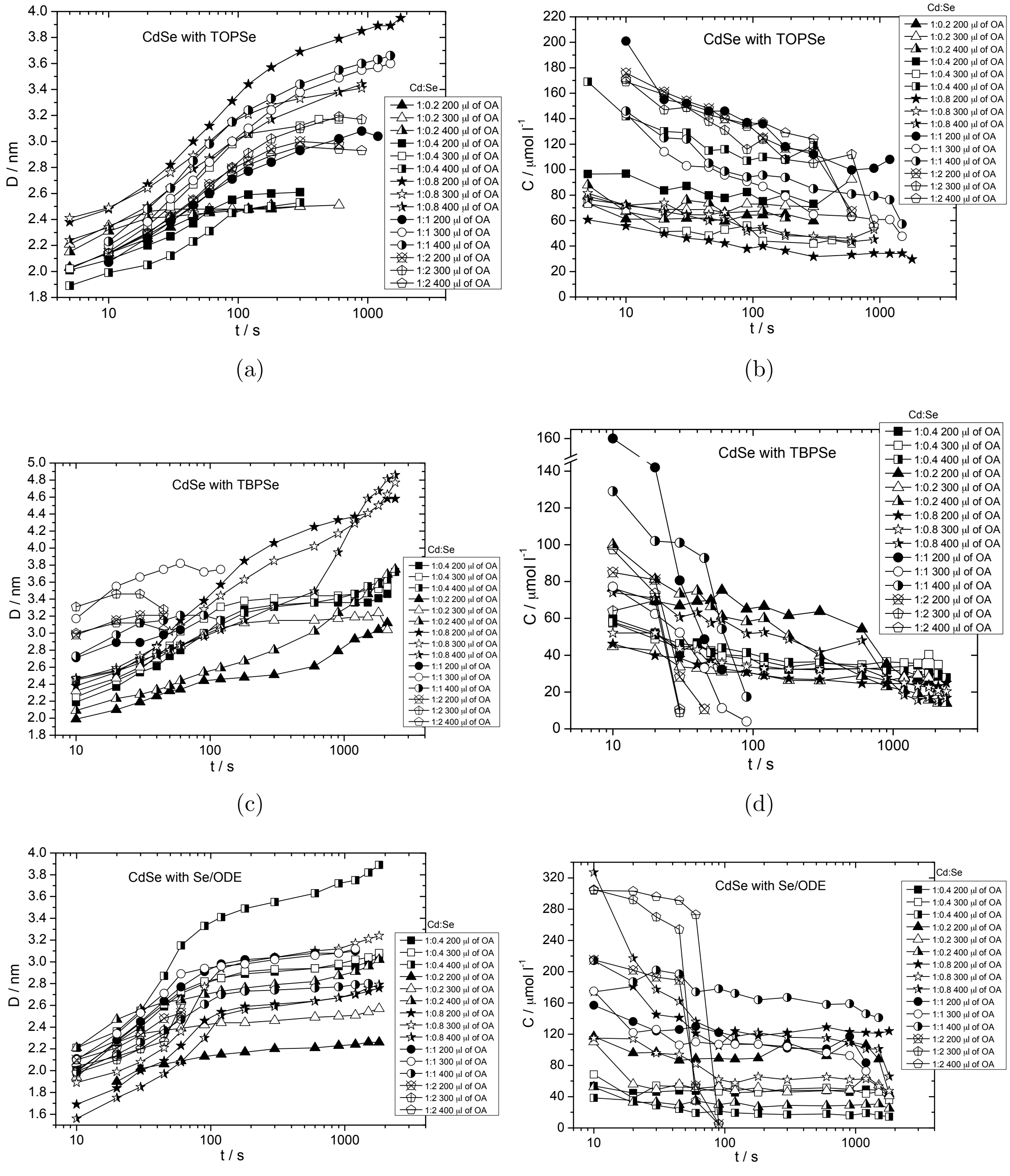

(a) (b)

(c) (d)

(e) (f)

Figure 4.5: Calculated from the absorbance NC diameters and concentrations for different reactions: (a), (c), and (e) CdSe NC diameters obtained using TOPSe, TBPSe, and Se/ODE, respectively; (b), (d), and (f) CdSe NC concentrations obtained using TOPSe, TBPSe, and Se/ODE, respectively.

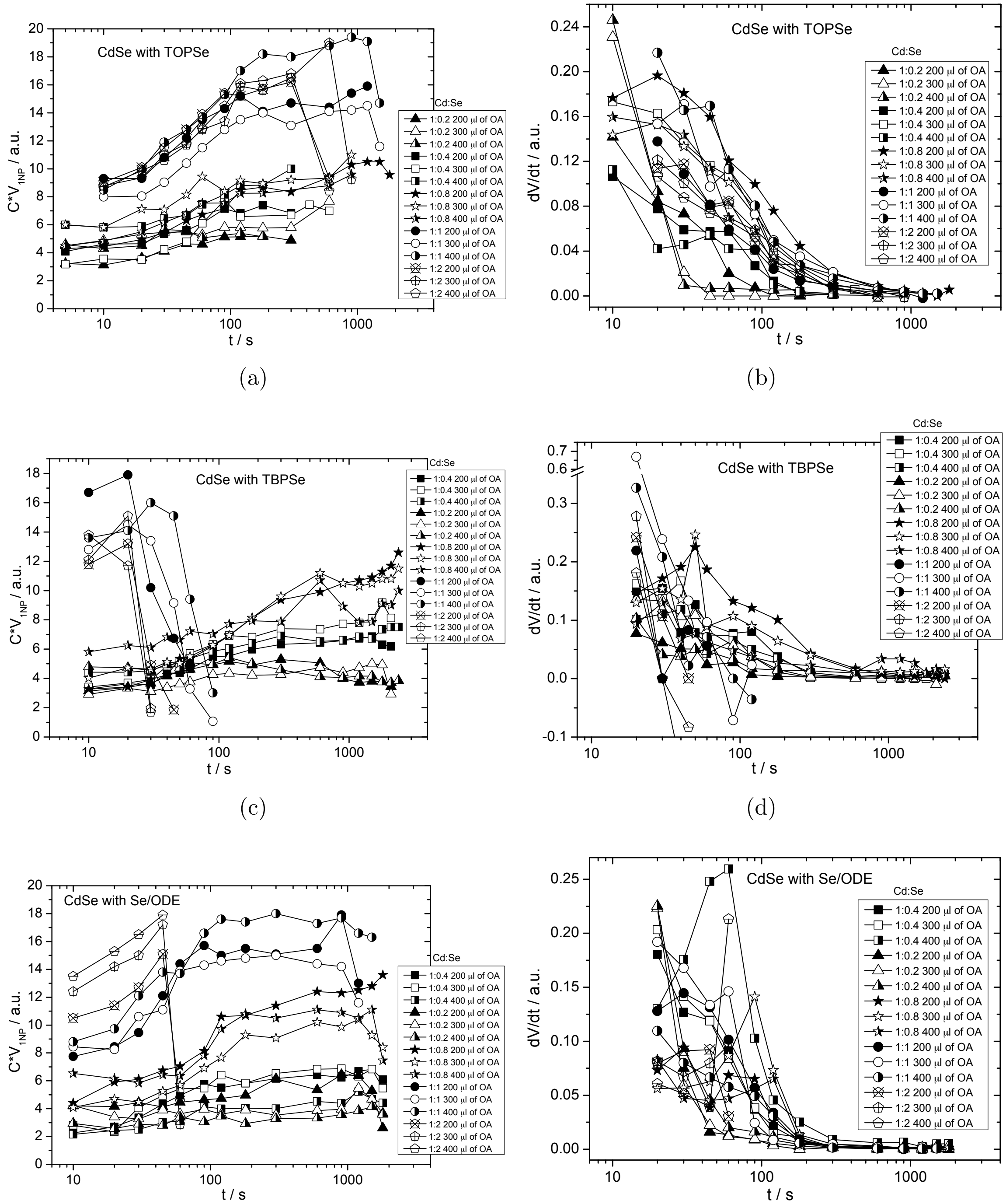

(a) (b)

(c) (d)

(e) (f)

Figure 4.6: Calculated from the absorbance NC total volumes and growth rates for different reactions: (a), (c), and (e) CdSe NC total volumes obtained using TOPSe, TBPSe, and Se/ODE, respectively; (b), (d), and (f) CdSe NC growth rates obtained using TOPSe, TBPSe, and Se/ODE, respectively.

and the drop of the temperature due to injection of the room temperature reactant(s) leads to quenching of nucleation. With these conditions, growth of the nuclei to larger NCs takes place at the temperature at which the formation of new nuclei does not occur [53], which brings about the formation of QDs with a narrow size distribution.

Comparison of three different Se precursors

To compare the activity of TOPSe, TBPSe, and Se/ODE precursors, nanocrystals diameters, concentrations, and hwhm were collected from the absorption spectra by the empirical fitting function [42] for the reactions 1 : 0.4 and 1 : 1 (Cd : Se) with 300 µl of OA (Fig. 4.7, 4.8). It can be seen (Fig. 4.7a, 4.8a) that almost for all reactions the sizes of synthesized CdSe QDs are very close to each other. This fact indicates that in the presence of *in situ* formed Cd^0 nanoparticles, the size of the produced QDs can be only slightly tuned using different Se precursors. In fact, the diameters obtained for various Cd : Se ratio and the amount of OA ranged from 1.9 till 4.0 nm for TOPSe, from 2.0 till 4.9 nm for TBPSe, and from 1.5 till 3.9 nm for Se/ODE (Fig. 4.5a, c, e). With all Se precursors, changing the growth time from 10 to 90 s led to about 1.0 nm size variation in the average diameter (corresponding to the shift of the absorption peak ca. to 70-80 nm). The concentration was the highest for 1 : 1 and 1 : 2 (Cd : Se) reactions (Fig. 4.5b, d, f) and reached 200, 160, and 320 µM for TOPSe, TBPSe, and Se/ODE, respectively, which is easily explained by presence of a bigger amount of a Se precursor. It should be noticed that to achieve different molar ratio of Cd to Se, the amount of a Se precursor was varied at the constant amount of a Cd precursor. As a result, the more selenium precursor existed in the initial stage, the faster the nucleation process occurred, and the more nuclei were generated in the nucleation stage.

Jasieniak et al. reported that the Se/ODE precursor culminated in poorer nucleation in comparison to TOPSe, since TOPSe facilitates nucleation by providing a more

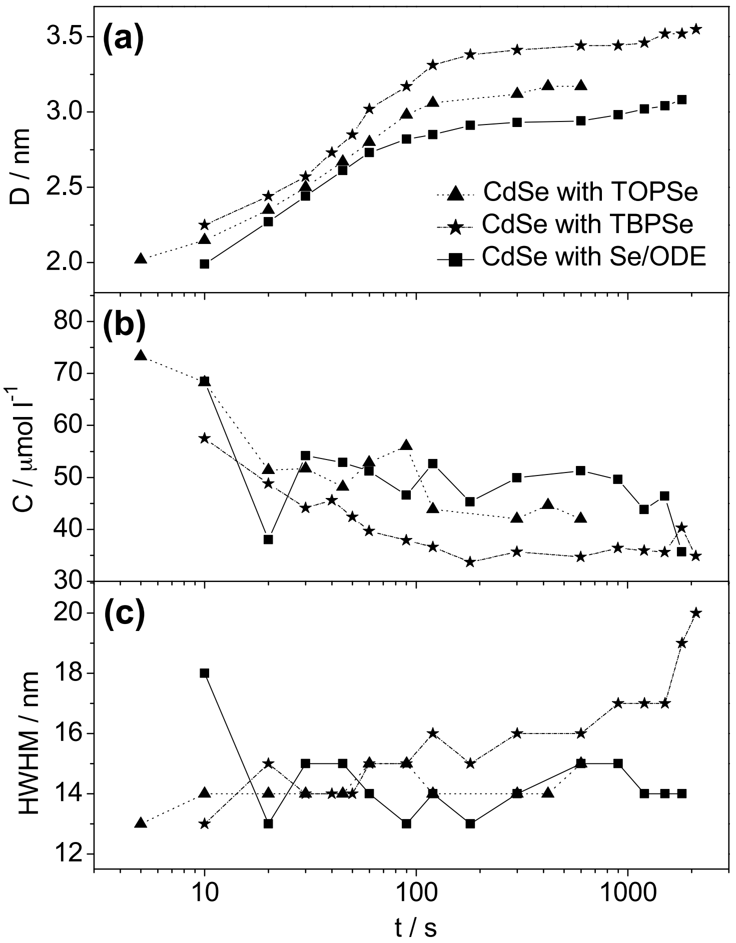

Figure 4.7: Calculated from absorbance diameters, concentrations, and hwhm of the CdSe NCs in the reaction Cd : Se = 1 : 0.4 with 300 µl of OA.

readily available source of selenium than Se/ODE [82]. Using TOPSe they obtained twice the concentration of CdSe NCs (approx. 50 µM) than using Se/ODE (approx. 25 µM). However, this dependence was not observed in our studies. As it can be seen both from Fig. 4.7b and Fig. 4.8b, the concentration of CdSe QDs synthesized using Se/ODE is not lower than using TOPSe and in some cases even a bit higher than the concentration of CdSe QDs synthesized using TOPSe (and also TBPSe). This can be explained by the fact that initial concentration of the stock Se/ODE solution during its preparation plays a crucial role for its activity (see page 43). Thus, for example, 0.18 M Se/ODE stock solution diluted to 0.04 M concentration was found to be much more reactive than the initially prepared 0.04 M Se/ODE solution. That

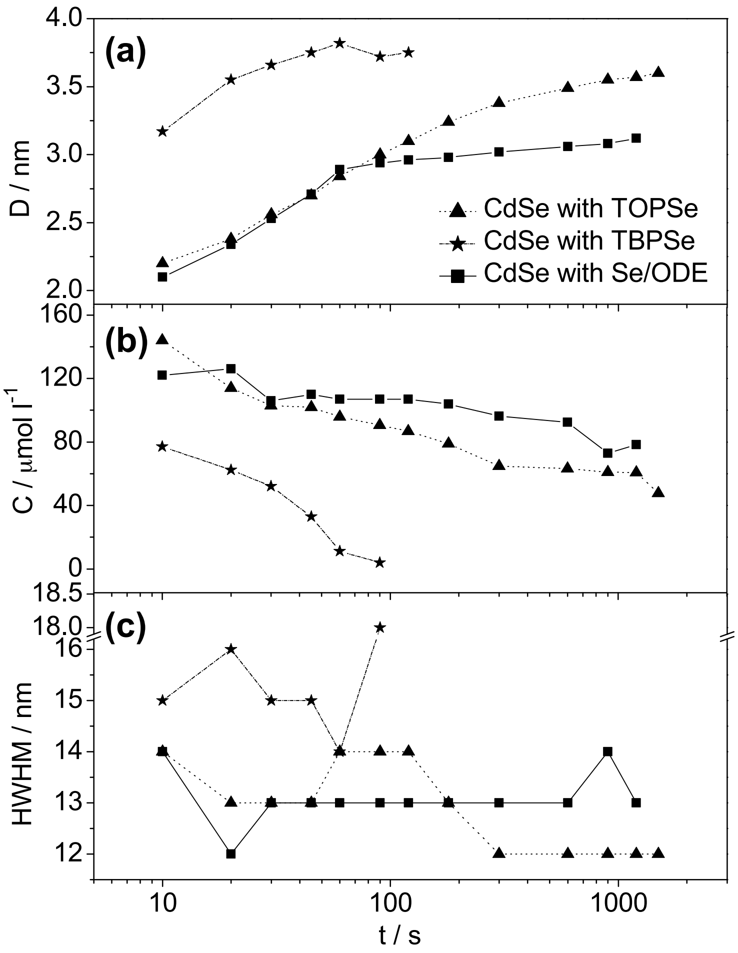

Figure 4.8: Calculated from absorbance diameters, concentrations, and hwhm of the CdSe NCs in the reaction Cd : Se = 1 : 1 with 300 μl of OA.

is why taking a high reactive Se/ODE solution as a Se precursor (with initial high concentration) results in production of a big quantity of CdSe QDs.

Role of TOP in the dissolution of CdSe QDs

In the course of the reactions with TOPSe, TBPSe, and Se/ODE precursors, CdSe nanoparticles grow continuously in the size, whereas their concentration decreases. Interestingly, the dissolution of CdSe QDs is not so pronounced in the reactions with Se/ODE as compared to TOPSe and TBPSe. To elucidate the precise role of TOP during the synthesis of CdSe NCs, we conducted an experiment which included the synthesis of CdSe QDs using Se/ODE with subsequent injection of TOP (amount of injected TOP was the same as in typical reactions using TOPSe as a Se precursor). From absorption spectra (not shown here) it is evident that the injection of TOP leads to a significant broadening of the size distribution. A summary of the effects of TOP on the final particles diameter, concentration, and half-width at half-maximum (hwhm) is shown in Fig. 4.9. The diameter of the nanocrystals increases and their concentration decreases much faster than without TOP injection. This means that TOP plays a big role in the dissolution of the nanoparticles. Presumably, TOP molecules go to the surface of nanoparticles to react with free Se sites which causes the NCs to dissolve.

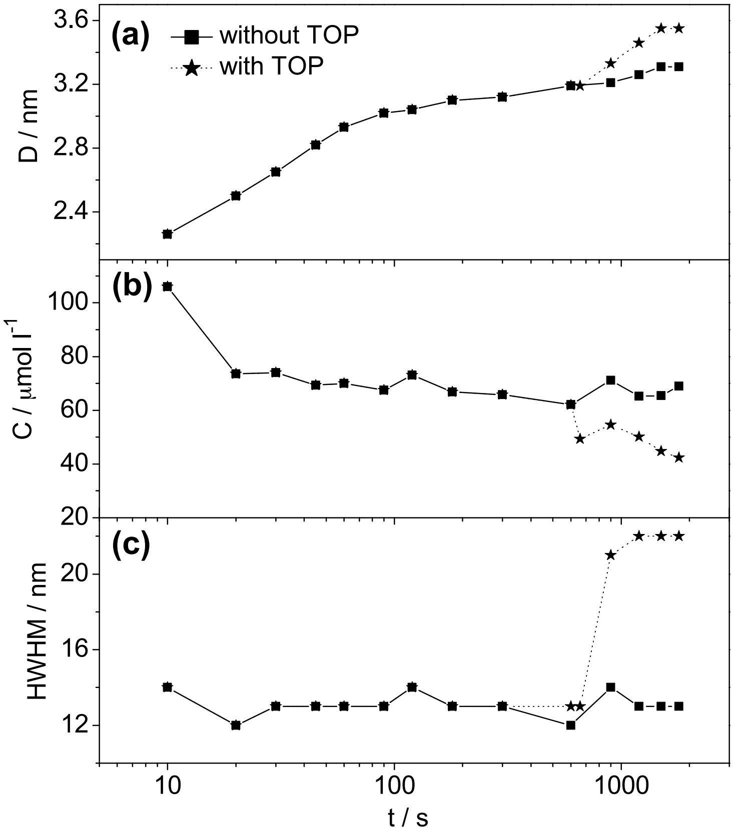

Figure 4.9: Calculated from absorbance diameters, concentrations, and hwhm of the CdSe QDs synthesized using Se/ODE followed by TOP addition after 600s of the growth (Cd : Se = 1 : 0.8, 200 μl of OA).

Effect of Cd : Se molar precursor ratio

Some previous studies showed that the initial precursor ratio can dramatically influence the behavior of CdSe synthesis [54][87][78][35]. For example, the group of Alivisatos [54] reported that with higher cadmium amount (Cd : Se = 1.9 : 1) the nanocrystals are "focused" after reaching the certain size and this focusing maintains at the growth temperature for hours before defocusing occurs. On the contrary, almost an equal initial molar ratio of Cd to Se (1.1 : 1) leads to rapid defocusing, and the size distribution of so-produced nanoparticles becomes far from ideal. To observe the influence of the initial molar precursor ratio in our study, reactions with different molar monomer concentrations (Cd : Se = 1 : 0.2, 1 : 0.4, 1 : 0.8, 1 : 1, and 1 : 2) were performed under the same reaction conditions. Energy-dispersive X-ray spectroscopy (EDX) (the intensity patterns are not shown here) of CdSe QDs with various initial molar ratio of Cd to Se and different Se precursors was used to determine the real surface ratio of Cd to Se in the synthesized nanocrystals (Table 4.1). The results showed that our method allows to control the Cd : Se surface ratio in the product. Thus, the final surface ratio of Cd : Se = 1 : 1 could be achieved only in Se rich reactions in the case of TOPSe, i.e. with the precursor molar ratio of Cd : Se = 1 : 2. In all other reactions, obtained CdSe QDs possessed excess of Cd. Knowing nanoparticles diameters (from absorbance), we have calculated the number of all surface atoms. Then taking into account the real ratio of Cd to Se from EDX measurements, we specified the percentage (%) of Cd and Se surface atoms separately (Table 4.1) according to the formulas summarized in Appendix A.

Nanoparticles formed in Se rich reactions (Cd : Se = 1 : 2) are not stable in solution. They precipitate after 1 min of growth for reactions with TBPSe and Se/ODE and after 10 min in the the case of TOPSe (Fig. 4.5 and 4.6). From a very fast precipitation of the CdSe NCs in the case of TBPSe and Se/ODE in comparison to TOPSe, we assumed that this may be due to the bigger amount of selenium on the surface

Table 4.1: Percentage of Cd and Se surface atoms calculated from the EDX measurements and NC diameters. All reactions were carried out with 200 µl of OA.

Precursor molar ratio Cd:Se	Growth time, s	Size of CdSe QDs, nm	Cd : Se ratio from EDX	Number of surface Cd+Se atoms	% of surface Cd atoms	% of surface Se atoms
Cd:Se = 1:2, TOPSe	300	3.04	1.02	226	51	49
Cd:Se = 1:2, Se/ODE	60	2.71	1.13	176	56	44
Cd:Se = 1:2, TBPSe	30	2.8	1.36	190	66	34
Cd:Se = 1:1, TOPSe	300	2.91	1.30	206	65	35
Cd:Se = 1:0.4, TOPSe	300	2.94	1.61	210	76	24
Cd:Se = 1:0.4, Se/ODE	300	2.74	1.60	180	74	26
Cd:Se = 1:0.4, TBPSe	300	3.08	1.30	234	65	35

of a nanoparticle. To prove this assumption, we resorted to the EDX measurements (Table 4.1), which surprisingly revealed the opposite trend, i.e. the smallest Cd : Se ratio on the surface is in the case of TOPSe and then increases to Se/ODE and finally to TBPSe (for Cd : Se = 1 : 2 reactions).

Thus, it was found that CdSe QDs with different precursor ratio of Cd to Se possess different reaction kinetics. In the case of TOPSe, in 1 : 0.2 (Cd : Se) reactions with 300 or 400 µl of OA and in a 1 : 0.4 (Cd : Se) reaction with 400 µl of OA, a development of a bimodal size distribution at later stages of the reaction, after several minutes of a very slow or even no growth, is observed. According to the absorption spectra, the CdSe QDs in the reaction 1 : 0.2 (Cd : Se) with 400 µl of OA after 900 s of growth form two sizes of the bimodal distribution – 2.6 and 3.1 nm. In these reactions, the growth rates are high in the beginning, but then decrease to almost zero after the first 60 s. The high growth rates lead to fast monomer depletion in the bulk solution. After the monomer concentration in the solution reaches values below approx. 20 % of the initial concentration, the first absorption maximum does not shift for the next 2 to 5 min, and then it becomes broader, the intensity decreases gradually, and the formation of a second fraction of nanoparticles with a bigger size begins. This can be seen both in the absorption and PL spectra (Fig. 4.1a). The bimodal size distribution, however, is not present in 1 : 0.8, 1 : 1, and 1 : 2 (Cd : Se) reactions. In these reactions, the first absorption maximum shifts continually for the first 5-10 min of the growth without any broadening in the absorption spectra. Thus, the formation of a bimodal size distribution is observed in some Cd rich reactions and only in the case of TOPSe. Our experiments showed the precise role of TOP in the broadening of the absorption spectra (see page 53). The possible explanation of the simultaneous presence of different NC sizes is given below, however, further investigations are required to understand exactly the mechanism of the formation of a bimodal size distribution.

The literature review suggests that often the absorption spectra broaden at later stages of the reaction without exhibiting any distinct features [88][89]. For the synthesis of bi- and trimodal size distributed CdSe QDs, Chen et al. proposed a one-pot method involving a series of injections of monomers in a low concentration [90]. However, sometimes the formation of a multimodal size distribution with two or more sharp absorption and PL peaks at later stages of the growth can be observed without additional injections (like in our case and [91][92]). This indicates that distinct types of CdSe NCs develop from the initial nearly monodisperse ensemble and special conditions are required for different sizes to be produced on their own. There is not much information about this phenomenon in the literature since more efforts have been directed to investigate and find conditions for the sharpest focusing of the size distribution and less attention has been paid to the defocusing stage. Thus, for instance, the selection of certain sizes of CdSe NCs during Ostwald ripening phase (i.e. at the end of the colloidal synthesis) and the possible mechanisms of their formation were reported by Tonti et al. [93]. The authors describe four main mechanisms that could take place in the reaction and lead to separated features in optical spectra: renucleation, freezing, ripening, and coalescence. All of these proposed schemes result in different evolution of the absorption and PL spectra at the ripening stage. Analyzing these mechanisms with the impact on our system, we came to the conclusion that the coalescence/aggregation scheme is the most possible in our reactions. Presumably, due to aggregation of particles to larger ones after 600 and 900 s of the growth, a new peak appears on the red side of the main maximum in both absorption and PL spectra (Fig. 4.1a). The intensity of the low energy component increases at the expense of the high energy component, which is seen by comparing the 600 and 900 s samples. This provides some confirmation of the presumed aggregation scheme.

Influence of Cd^0 particles on the reaction kinetics

The formation of nanoparticles can be divided into two major steps: nucleation and growth. The separation of the nucleation and growth stages is of utmost importance since only in this case a high degree of monodispersity can be achieved without using post-synthesis size-selective techniques. Usually in experiments, both the nucleation and the growth speed of the ensemble of nanocrystals in the reaction solution are affected by many factors. In the growth stage, the number of nuclei formed in the nucleation stage would strongly affect the growth speed of nanocrystals. If more nuclei are formed in the nucleation stage, the less residual monomers are left in the solution, and the monomer supply may not be enough to maintain a fast growth and *vice versa*.

In this sense, production of Cd^0 particles in the course of the reaction maintains the constant level of the monomer concentration in the solution and provides almost ideal conditions for the QDs growth. Thus, during the synthesis of semiconductor NCs, a burst of nucleation and a length of steady growth phase are important to obtain monodisperse particles.

Mulvaney and co-workers (Bullen [58] and van Embden [55]) examined the reaction kinetics for analogous system of CdSe NCs as used in our work but without *in situ* formed Cd^0 nanoparticles. In their experiments, the concentration of nanoparticles increased during the first 30-40 s of the reaction with a subsequent decrease. However, in our system, we observed no increment in the concentration during the first seconds of the NCs growth, but only continuous lowering or stagnation of the concentration during the entire reaction time (Fig. 4.5b, d, f). This means that *in situ* formed Cd^0 particles provide enough monomer for the immediate nucleation that ceases almost straightway after the injection of a Se solution (already in 5 s after the injection all nuclei are formed). The burst of nucleation is followed by further steady growth of the NCs. Consequently, Cd^0 particles bring about the formation of highly monodisperse NCs.

Van Embden et al. [55] studied the influence of OA concentration on the nucleation and growth of the NCs. They demonstrated that an overall faster growth rate is expected for systems with higher OA content, since the increase in the oleic acid concentration causes the maximum number of nucleated particles to be reduced and "early time ripening" (ERT) occurs. ERT is a combination of Ostwald ripening, ligand induced ripening, and normal growth through monomer accretion. It takes place due to a constant decrease in free monomer concentration, proving that monomer leached into the solution from dissolving particles was contributing to a net increase in the particle size. However, our reaction system is more complicated and there is no simple correlation between the OA concentration and the formation of CdSe QDs, as in the case observed by van Embden et al. [55]. In our system, the monomer supply is also provided by the dissolution of Cd^0 particles. Hence, the monomer concentration depends both on the initial Cd^{2+} concentration and on the dissolution rate of Cd^0. Moreover, the monomer activity, a parameter determining the reaction kinetics, depends on the ratio between Cd^{2+} and OA in solution. In the reaction without *in situ* formed Cd^0 particles, the formation of CdSe QDs decreases the Cd^{2+} monomer concentration and sets some OA molecules free. In the course of the reaction, the OA to Cd^{2+} ratio increases and consequently the activity of the monomers decreases. Thus, the amount of OA does not have a direct influence on the Cd^{2+} concentration and consequently a higher OA : Cd^{2+} ratio always means a lower Cd^{2+} activity.

In the reaction with *in situ* formed Cd^0 particles, OA not only has an influence on the activity of Cd^{2+} in solution, but it can also bring additional Cd^{2+} monomers by dissolving the Cd^0 particles (Fig. 4.10). Formation of Cd^0 particles without Se injection was investigated by AAS for different OA concentrations (Fig. 4.10). It can be seen that in the first 100 s the amount of precipitated Cd^0 grows linearly for all three OA concentrations and reaches 25 % of the used Cd. Then depending on

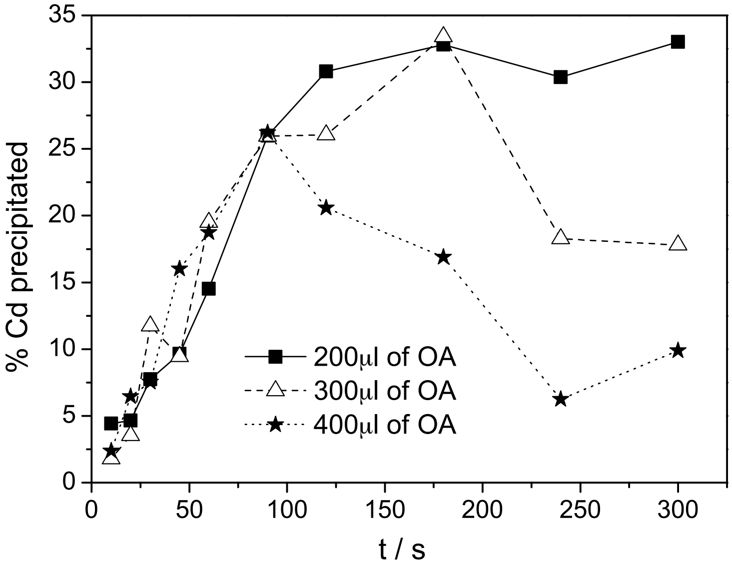

Figure 4.10: AAS measurements of Cd^0 precipitate without Se injection in the reactions with different OA concentrations: 200, 300, and 400 µl.

the OA concentration, the amount of precipitated Cd^0 stays constant (for the lowest OA concentration) or decreases. The higher the concentration of OA the more Cd^0 particles dissolve in the course of the reaction.

Thus, on the one hand, a bigger OA concentration reduces the Cd^{2+} monomer activity, but on the other hand, it increases the Cd^{2+} concentration leading to an increase of the Cd^{2+} monomer activity. To conclude, OA influences the Cd^{2+} activity in two opposed ways, therefore, no simple dependence of the reaction kinetics on the initial OA concentration can be found in our case.

Unfortunately, the synthesis due to formation of Cd^0 particles becomes less reproducible since it is rather difficult to notice the moment of formation of the first Cd^0 nanoparticles and do the injection at the same amount of Cd^0 particles present in solution. That is why despite the fact that our method brings about the production of highly monodisperse CdSe NCs, it still needs to be optimized, and further work in this direction is required. To illustrate the degree of reproducibility, Fig. 4.11 shows the results for two different syntheses carried out under the same reaction conditions (viz. Cd : Se = 1 : 0.8; 200 µl of OA and a Se/ODE precursor). The differences are quite flaring: the nanocrystal diameters vary from 2.3 to 3.3 and from 1.7 to 2.7 nm; the concentrations from 105 to 70 µM and from 180 to 120 µM, respectively. However, the general trends are the same in both cases: a continuous well-pronounced increase in the diameter and slow lowering of the concentration with the subsequent stagnation. This indicates that the course (or mechanism) of the reaction is reproducible enough in contrast to the exact magnitudes of diameters, concentrations, etc. of the obtained CdSe QDs. The reproducibility of the trends of the reactions allows us to draw general conclusions about the behavior of the nanoparticles and the reaction kinetics.

Analyzing curves of the growth rates in the volume per particle (Fig. 4.6b, d, f), one can conclude about the rate of monomer depletion from solution. Thus, the growth

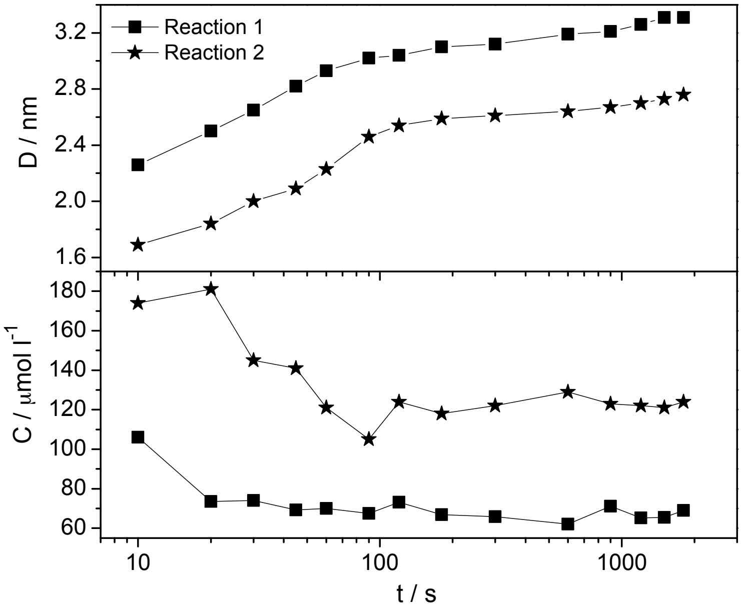

Figure 4.11: Two reactions with Se/ODE carried out under the same synthetic conditions Cd : Se = 1 : 0.8 and 200 µl of OA.

of the CdSe QDs in our system takes place mostly in the first 300 s of the reaction for all Se precursors, after that the growth rate reduces to zero due to the complete consumption of the Se precursor (Fig. 4.6b, d, f). Cd^0 particles are still present in the solution and need to be separated from the colloidal solution of NCs by means of centrifugation. For the reactions Cd : Se = 1 : 0.2 (with TOPSe and Se/ODE), the growth rates are the highest in the beginning (during first 45 s), but then the growth ceases very quickly due to fast depletion of a Se precursor. With a higher molar ratio of Cd to Se (1 : 0.8 and 1 : 1) for all Se precursors, growth is the slowest.

4.2.4 Size distribution of as-synthesized CdSe NCs

Presently, characterization of the size distribution of NCs is achieved by standard procedures, such as absorption and photoluminescence spectroscopy by measuring the hwhm or fwhm of the spectra, respectively; powder X-ray diffractometry (XRD); transmission electron microscopy (TEM) and high resolution TEM (HRTEM). In our system, seeds that formed in the beginning of the reaction already have a very narrow size distribution according to the absorption spectra (Fig. 4.1 on page 41). We do not observe a significant narrowing of the size distribution during the further growth. In addition, the narrowest observed hwhm (12 nm; Fig. 4.8c) proves a presence of a monodisperse ensemble comparable with samples after several stages of size-selective precipitation, although no post-preparative treatment was applied in the present case. This indicates that high quality nearly monodisperse CdSe QDs can be obtained in the system with ODE using *in situ* formed Cd^0 particles as a Cd precursor, and the presence of TOPO becomes in such case unnecessary to produce good quality CdSe NCs [94][95].

The narrow size distribution of the CdSe QDs synthesized in this work is also evidenced by TEM. A representative example is shown in Fig. 4.12. It can be seen that the nanoparticles with both the smallest and the biggest Cd : Se ratio investigated in the present study (viz. 1 : 0.2 and 1 : 2) are highly monodisperse and form on a TEM grid not only well-ordered two-dimensional superlattices, but even small facetted colloidal crystals (Fig. 4.12). The average sizes estimated from TEM micrographs were generally larger than those obtained from the absorbance since the size calculated from the TEM image takes the ligand shell into account. It is also possible that electron microscopy in the regime of extremely small sizes leads to an overestimation of the contribution of larger particles of the given size distribution in the ensemble[5]. Insets in Fig. 4.12a, b also represent the fast Fourier transforms (FFT) of the same area; the inset in Fig. 4.12b additionally shows a HRTEM image of a single CdSe particle. The existence of lattice fringes in the HRTEM image further confirms the high crystallinity of CdSe QDs.

The X-ray diffraction pattern (XRD) also indicates their crystallinity in bulk (Fig. 4.13). We have fulfilled the XRD analysis of the CdSe QDs with the initial molar

---

[5] The term "ensemble" describes the whole population of particles present in the colloidal solution at a given time [64].

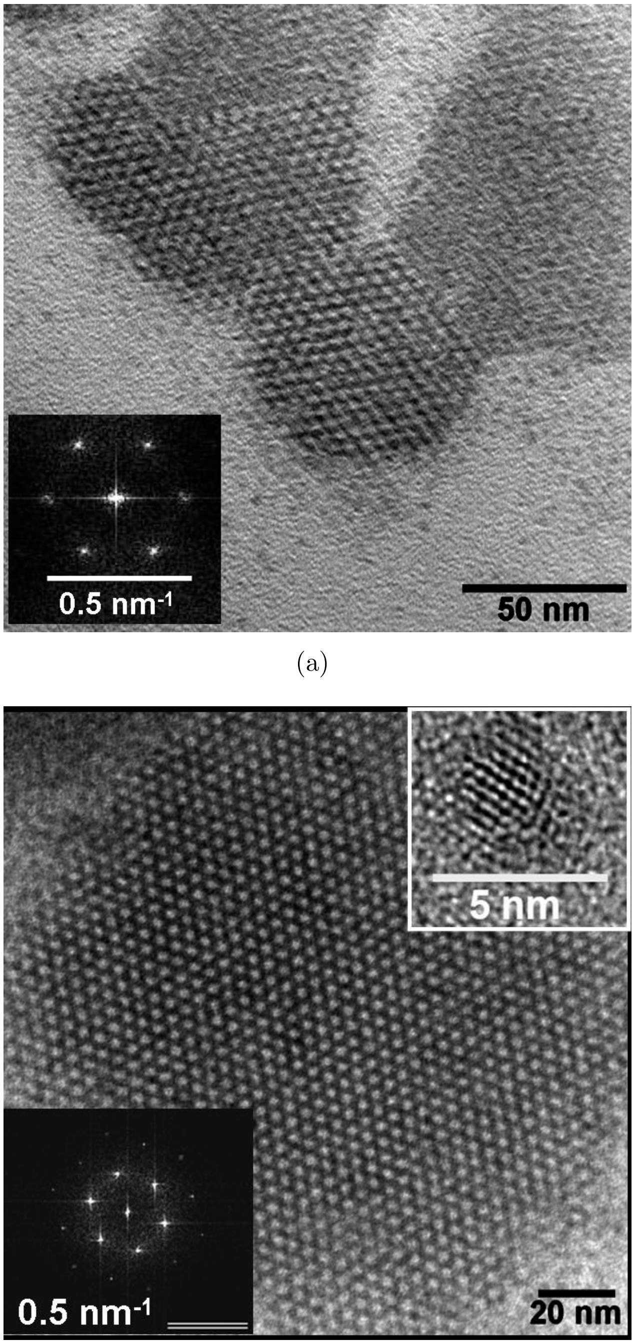

(a)

(b)

Figure 4.12: Representative TEM images of CdSe QDs show the formation of crystalline structures: (a) CdSe sample synthesized using TOPSe with the initial excess of Cd (Cd : Se = 1 : 0.2), 200 µl of OA and the growth time of 90 s; (b) CdSe sample synthesized using TOPSe with the initial excess of Se (Cd : Se = 1 : 2), 200 µl of OA and the growth time of 450 s. Insets in (a) and (b) show the FFT images of the same area and the inset in (b) a HRTEM image of a single particle.

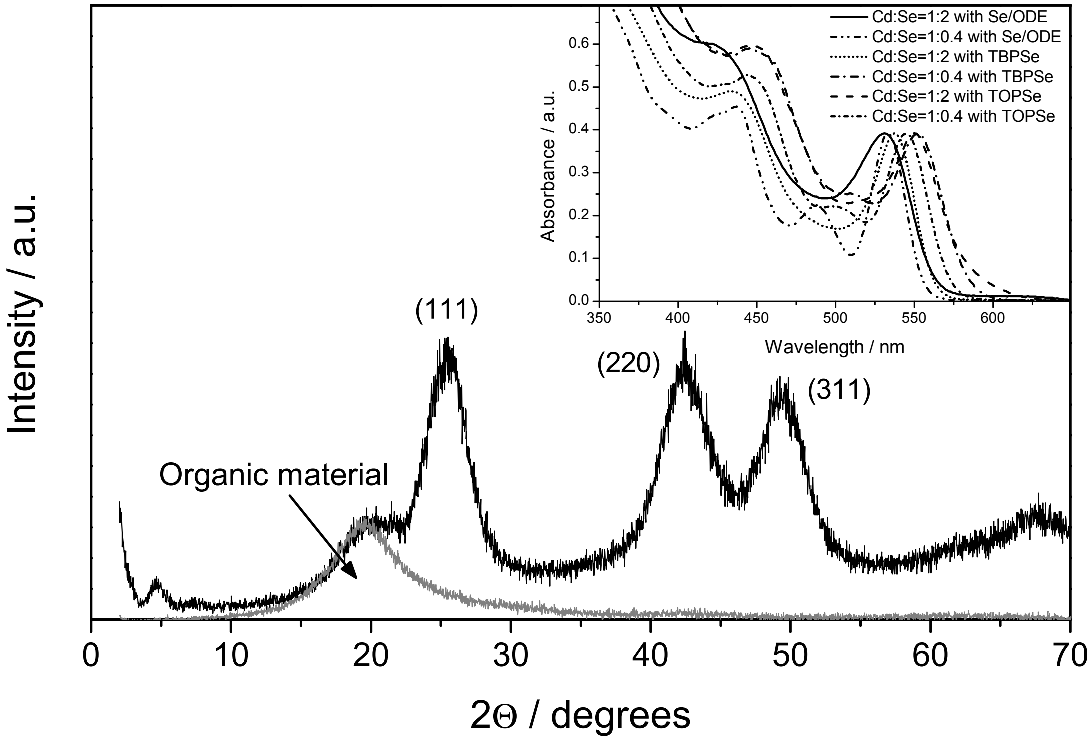

Figure 4.13: Representative XRD pattern of CdSe QDs typical for the precursor molar ratio Cd : Se = 1 : 0.4 and 1 : 2, 200 µl of OA and three Se precursors (TOPSe, TBPSe, and Se/ODE). Inset depicts the absorption spectra for different CdSe QD samples that exhibit the same crystallographic structure.

ratio of Cd : Se = 1 : 0.4 and 1 : 2, 200 µl of OA, obtained using TOPSe, TBPSe, and Se/ODE. All XRD patterns were collected from nanocrystal samples with similar sizes (from 2.7 till 3.1 nm in diameter), and the broad patterns correspond to small particle sizes. The XRD analysis revealed that all samples exhibit a zinc blende crystal structure[6] with three distinct features of Bragg's scattering summarized in Table 4.2. Moreover, for a wurtzite structure, two more typical reflections, i.e. the (102) reflection at $2\theta = 35°$ and the (103) reflection at $2\theta = 46°$, should be present which are not observed in the XRD pattern, thus providing further confirmation for a zinc blende structure. The sizes of NCs were calculated from fwhm of the reflection peaks

---

[6] The bulk crystals of CdS and CdSe commonly exhibit the wurtzite structure when prepared at high temperature [51].

using Eq. 2.7 on page 13. The mean diameter of nanoparticles from three crystallographic reflections is 2.79 nm which is in good agreement with the size calculated from absorbance (Eq. 2.1 on page 10), i.e. 2.71 nm.

Table 4.2: Determination of crystallographic reflections and corresponding crystalline diameters from the XRD pattern.

reflection	$2\theta(deg)$	$fwhm(rad)$	$d(nm)$
(111)	25.4	0.063	3.02
(220)	42.6	0.075	2.64
(311)	49.3	0.075	2.72

As it can be seen, the samples contain some organic impurities (reflection at $2\theta = 20°$) even after a very thorough cleaning procedure and therefore could only be obtained in a form of a viscous paste (Fig. 4.13). A small reflection maximum is also observed in the small-angle region of the XRD diffraction pattern (at $2\theta = 4.7°$) due to periodicity of the arrangement. The appearance of such a peak once again indicates the narrow size distribution of the nanoparticles. Since the XRD patterns look the same for the reactions with initial molar excess of Cd and Se and three different Se precursors, these parameters do not influence the resulting crystal structure of CdSe QDs. It has been reported that the form of the absorption spectrum can give information about the crystal structure of CdSe QDs [82]. Fig. 4.13 (inset) represents the absorption spectra of six investigated CdSe samples, all of which showed a zinc blende structure. These absorption spectra have different shapes, in particular, the position of the second excitonic maximum is different and it is more or less pronounced in different samples. Nevertheless, all samples exhibit the same zinc blende structure. This indicates that in the present case the shape of the absorption spectrum cannot be used to predict the crystallographic structure.

It has been pointed out that the wurtzite structure of CdSe nanocrystals is obtained at the injection temperature of ca. 300 °C [76][77][52], whereas the zinc blende structure is more typical to obtain at the temperature of 200-240 °C [80], since in thermodynamics it is notable that zinc blende and wurtzite forms are the most stable at lower and high temperatures, respectively. But in our study, the zinc blende nanocrystals were synthesized with the injection at 300 ℃. Thus, temperature cannot be the factor leading to the zinc blende crystal structure in the present case. Another explanation deals with the type of the used Se precursor: the zinc blende phase is favored by the elimination of phosphines [96] and wurtzite by the phosphines presence in the ligand shell of nanoparticles [51]. For instance, Sapra et al. reported that the presence of Se complexes, as in the case of TOPSe (or TBPSe), favors the wurtzite crystal structure, whereas the absence of phosphine ligands (such as TOP or TBP) leads to the formation of nanocrystals in the zinc blende phase [81]. Additionally, it has been reported that in the case of pure fatty acid ligands (such as oleic acid), the zinc blende crystal structure can stably exist at high temperatures [85]. As it was evidenced by ^{1}H NMR analysis, our as-synthesized CdSe NCs contain oleic acid molecules in the ligand shell. Moreover, ^{31}P NMR measurements revealed that no phosphorous compounds are present in the ligand shell not only in the synthesis with Se/ODE, but also with TOPSe (and TBPSe) as a Se precursor. Since NMR spectroscopy is a quite sensitive analytical method, the possibility that TOP molecules are the ligands of our CdSe QDs can be ruled out, and the only ligands in this case are oleic acid molecules[7]. Thus, due to the fact that our CdSe QDs are capped with OA molecules and there is no TOP in the ligand shell, the zinc blende crystal structure is stable in our reactions with the injection at 300 ℃ both for the synthesis involving phosphorous and phosphorous-free synthesis. To sum up, our synthesis allows to produce high quality zinc blende CdSe NCs, although before often high quality NCs for the CdSe system were limited to the wurtzite form [26].

---

[7] The composition of the ligand shell will be more thoroughly discussed in Chapter 6.

4.3 Conclusions

To conclude, highly monodisperse zinc blende CdSe QDs were synthesized using *in situ* formed from cadmium oleate Cd^0 particles that acted as a Cd precursor. The narrow size distribution was evidenced by UV-Vis absorption and PL spectra, as well as by TEM images. The reaction kinetics with three different Se precursors, different Cd to Se ratio and amount of OA, was studied. The nature of a phosphine-free Se/ODE precursor, which along with TOPSe and TBPSe resulted in high quality QDs, was investigated by means of MS and NMR spectroscopy. Additionally, it was found that injection of TOP leads to the broadening of the size distribution of the CdSe ensemble obtained with Se/ODE precursor. EDX measurements revealed that varying the precursor molar ratio of Cd to Se allows to control this Cd : Se ratio at the surface of the synthesized CdSe QDs. It was shown that the influence of the amount of OA on the reaction kinetics is more complicated in the reactions with *in situ* formed Cd^0 NPs than in the reactions without Cd^0 precipitate.

Chapter 5

Investigation of growth kinetics of CdS nanocrystals

This chapter discusses a novel synthesis for spherical CdS NCs involving *in situ* formed Cd^0 particles (from cadmium oleate) as a Cd precursor, which results in CdS QDs with a narrow size distribution. Reactions with different S precursors (S/ODE, TOPS, and TBPS), Cd : S ratio (1 : 0.2, 1 : 0.4, 1 : 0.8, 1 : 1, and 1 : 2), and OA concentrations (200, 300, and 400 µl) were studied to monitor the reaction kinetics. The ligand shell of CdS NCs obtained with different S precursors was analyzed by means of ^{1}H NMR spectroscopy. It was shown that independent of the used S precursor the synthesized by this method NCs are capped with oleic acid molecules. The appearance and disappearance of magic-sized nanocrystals (MSNCs) during the synthesis of regular-sized CdS NCs (RNCs) was investigated. Moreover, the dynamical transformations of RNCs into MSNCs during the storage of solutions at room temperature were observed. A tentative MSNC-associated nucleation-growth mechanism was proposed for the formation of CdS NC and the reverse transfer.

5.1 Overview of different synthetic methods for CdS nanoparticles

Semiconductor nanocrystals (NCs) are of great interest for both fundamental scientific research and technical applications as a result of the large ratio of surface atoms and quantum confinement of excitons. CdS NCs, belonging to the most important II-VI group of semiconductor materials, have attracted much attention and have been extensively studied due to their size-dependent photoluminescence in the visible spectral region and the advances in methods of their preparation. In 1982, Henglein observed a blue shift in the absorption spectra of a colloidal solution of CdS with respect to the bulk band gap [71]. This effect was explained by Brus in 1983, who discovered its quantum mechanical nature [68]. Today, CdS nanoparticles can be produced by a variety of techniques including both physical (top-down) and chemical (bottom-up) methods. Among them are sol-gel [97][98], ionic reactions in liquids [99], chemical bath deposition (CBD) route [100][101], electrodeposition (ED) [102], hydrothermal route [103][104][105], solvothermal methods [106][107], ultrasound irradiation [44], laser ablation [108], micelles [92][109], solid-state reaction [110][111], colloidal hot-injection [51][52] and non-injection methods [112][113], synthesis in aqueous milieu [114][115], etc. Whereas physical processes can produce large quantities of NCs, the uniformity of sizes is very difficult to achieve. On the contrary, colloidal chemical synthetic methods can be used to synthesize monodisperse nanocrystals with a controlled particle size. Thus, chemical colloid methods serve *prima facie* the purpose of fundamental research, because to fully exploit the potential of NCs with the desired properties it is essential that they are synthesized with uniform size and shape. A major breakthrough in the chemical synthesis of CdS NCs was done by Murray et al. in 1993 [51], where good quality wurtzite CdS QDs were obtained by the hot-injection technique from dimethyl cadmium ($Cd(CH_3)_2$) in a coordinating solvent (TOPO).

The next substantial improvement was the modification of their method by Peng et al. in 2001 [76], where the authors used a safer cadmium oxide (CdO) instead of $Cd(CH_3)_2$. Then in 2002, Yu et al. [52] proposed to substitute a hazardous TOPO solvent with a noncoordinating solvent (ODE) and produced high quality CdS QDs with oleic acid ligands from CdO as a Cd precursor and elemental sulfur dissolved in ODE (S/ODE) as a S precursor. The authors studied the influence of the amount of OA on the reaction kinetics and noticed the formation of magic-sized nanoclusters during the synthesis. The latter, however, was not further discussed.

5.2 Introduction to magic-sized nanoclusters

Research on small semiconductor nanoclusters that can be regarded as the smallest building units of semiconductor materials has been extensively carried out in the past years. In particular, binary cadmium sulfide clusters have been extensively investigated both experimentally [108][116][117] and theoretically [118][119][120] due to the variation of their electronic properties as a function of size. Theoretical studies of bare CdS nanoclusters (i.e. taking into account only core, without ligand shell) have revealed a strong correlation between the binding energies or stability of the clusters and their highest occupied molecular orbital (HOMO) – lowest unoccupied molecular orbital (LUMO) gaps [118][119]. Recently, Chu et al. studied the lowest energy structures and electronic properties of Cd_nS_n (n = 2–8) clusters using the generalized gradient approximation (GGA) method and found that the magic numbers of such stoichiometric small clusters are n = 3 and 6 [120]. The authors considered these magic clusters to be the most stable since they were found to exhibit the local maximal energy gap. Experimental results confirm the existence of magic-sized CdS nanoclusters or nanocrystals (MSNCs) that are formed independently in different syntheses [121][122][123].

MSNCs have different properties in comparison to the corresponding regular-sized nanocrystals (RNCs). Due to their stable and defined molecular structure, MSNCs always possess fixed sizes and can be detected by the appearance of sharp absorption peaks at certain wavelengths [124]. MSNCs have a local maximum in binding energy, and their formation is thermodynamically driven [125]. Several arguments exist as to why the formation of magic-sized quantum dots is energetically preferable. For example, it may be that due to the close-shell electronic structure, these magic-sized semiconductor nanoclusters are thermodynamically more stable than the clusters which are either a little smaller or a little bigger but without close-shell configuration [78][126]. Another explanation assumes that their large thermodynamic stability may originate from the delicate balance between the surface and the intrinsic energy of a nanoparticle [127]. The size of MSNCs usually lies in the range between 0.7 and 2 nm, and therefore, they have an even higher surface to volume ratio than RNCs. Crystallization of single-sized nanoclusters in three-dimentional superlattices makes it possible to study both the micro- and the macrostructure of such crystals. Thus, the CdS cluster core structure as well as the superlattice geometry can be reliably determined by means of XRD analysis. For instance, Vossmeyer et al. reported on a single-crystal structure in which CdS clusters are linked covalently to build up a superlattice that was best described as consisting of two enlarged and interlaced zinc blende lattices [128]. Although the formation of CdS MSNCs have been repeatedly reported, the knowledge about the properties of MSNCs is still limited and more research is required.

In this thesis, a novel method for the synthesis of high quality CdS QDs involving *in situ* formed Cd^0 particles as a Cd precursor (for details see Chapter 4) was applied, and the formation and disappearance of magic-sized nanocrystals in the synthesis and during the storage of CdS NCs were analyzed.

5.3 Results and discussion

5.3.1 Investigation of properties of as-synthesized CdS QDs

In our work, CdS QDs were synthesized using Cd^0 particles, *in situ* formed from cadmium oleate, as a Cd precursor and three different S precursors: S/ODE, TOPS, and TBPS. Cd^0 nanoparticles regulate the monomer supply (help to avoid fast monomer depletion from solution) for the growth of the CdS QDs and therefore lead to high quality NCs with a narrow size distribution. A comparison of reactions with and without *in situ* formed Cd^0 precipitate is represented in Fig. 5.1. It is evident that the CdS NCs in the reactions without Cd^0 particles grow faster and within approx. 2 min the monomer is depleted from the solution which results in broadening of the absorption spectra (Fig. 5.1a). On the contrary, *in situ* formed cadmium precipitate provides constant monomer supply, and CdS QDs grow during 1200 s of the reaction slowly and continuously, which better allows to tune the sizes of as-synthesized NCs (Fig. 5.1b). Although the size distribution of the CdS QDs in the beginning of the reaction obtained using S/ODE with and without cadmium particles is almost the same (Fig. 5.1a, b), for both TOPS and TBPS precursors there is a big difference in the shape of the absorption spectra. Thus, in the reactions with Cd^0 particles, a sharp first excitonic absorption peak and up to three higher excitonic transition states are clearly resolved (Fig. 5.1d, f), whereas without Cd^0 no sharp peaks can be observed (Fig. 5.1c, e). For all reactions with TOPS and TBPS, the CdS NPs grow gradually during the first 1200-1500 s and then the growth stops, because the absorption spectra do not change for the next 20 min. Additionally, as it can be seen from Fig. 5.1c-f, the CdS QDs which are formed in the reactions with cadmium precipitate have smaller sizes and higher concentrations.

The high monodispersity of the CdS QDs obtained by our method (i.e. with *in situ* formed Cd^0 particles) is further confirmed by TEM images (Fig. 5.2). Fig. 5.2a

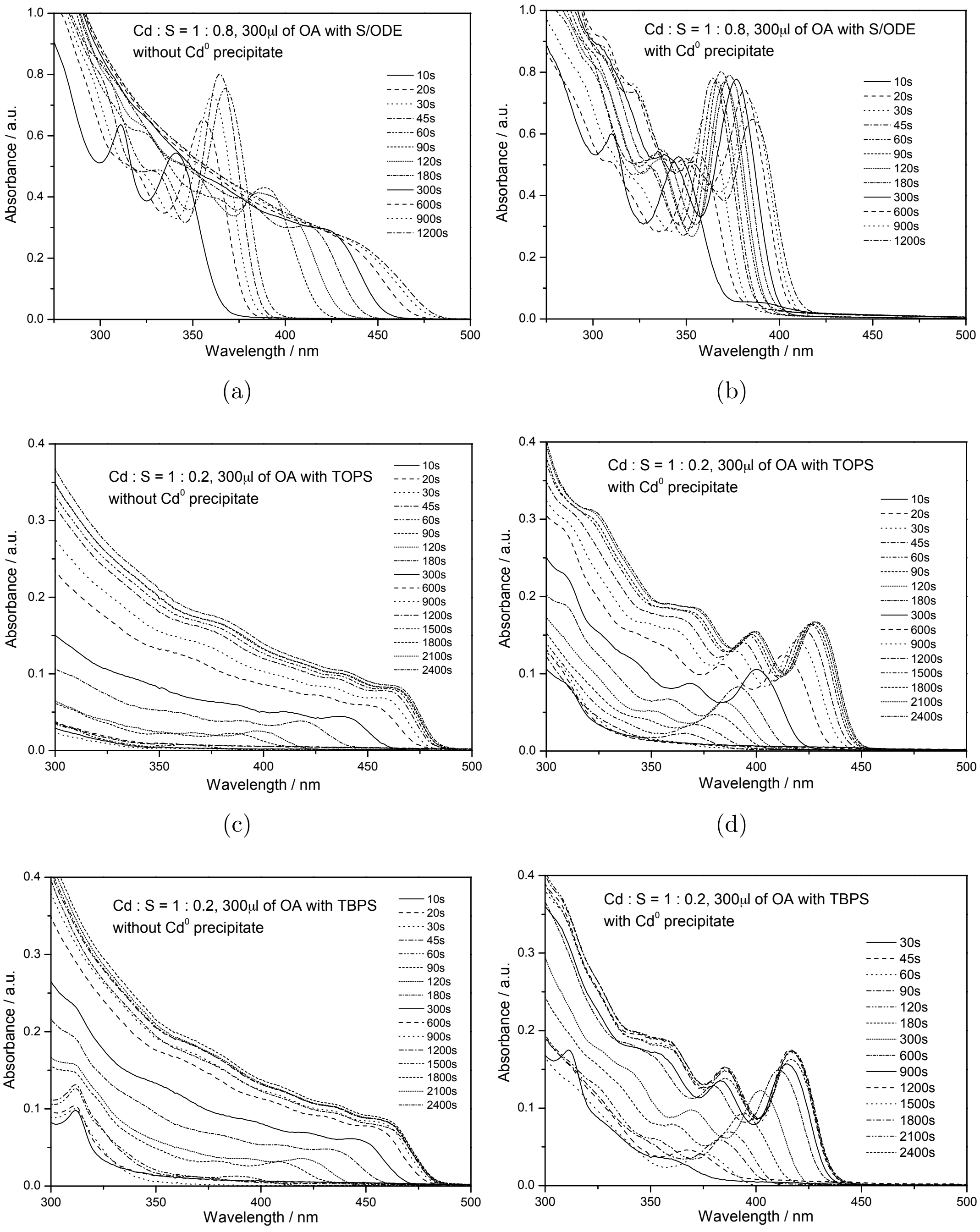

(a) (b)

(c) (d)

(e) (f)

Figure 5.1: Temporal evolution of the UV-Vis absorption spectra of CdS QDs synthesized without and with *in situ* formed Cd^0 particles (left and right column, respectively): (a) and (b) Cd : S = 1 : 0.8 with S/ODE; (c) and (d) Cd : S = 1 : 0.2 with TOPS; (e) and (f) Cd : S = 1 : 0.2 with TBPS. All reactions were carried out with 300 µl of OA.

shows CdS quantum dots of the biggest diameter (5.6 nm) that can be synthesized by our method with a very narrow size distribution. From Fig. 5.2b one can see that the monodispersity of as-synthesized NCs (the mean diameter of the nanoparticles is 4.3 nm) is so high that they form on TEM grids crystalline structures, which is additionally supported by the FFT image. It should be noted that no size-selective precipitation was applied after the synthesis.

Among three used S precursors, S/ODE solution possesses the highest activity which results in immediate NC formation after injection in comparison to TOPS and TBPS, where the seed formation takes up to 30-60 s (Fig. 5.1d, f). Moreover, S/ODE precursor brings about up to 12 times higher nanoparticle concentration than TOPS and TBPS. Thus, for the reactions with initial molar ratio of Cd to S $= 1:1$, the maximum concentration of CdS NCs reaches 120 µM for S/ODE and 11 µM for TOPS and TBPS. The TOPS and TBPS precursors seem to exhibit almost the same reactivity, since NC concentration varies for them from 2 to 11 µM in the reactions with different Cd : S ratio (the NC concentration increases in the row with ratio of Cd : S $= 1:0.2$, $1:0.4$, $1:0.8$, $1:1$, because the amount of a S precursor was varied at the constant amount of a Cd precursor). The concentration of NPs was calculated from the first excitonic absorption peak using Lambert-Beer's law (Eq. 2.5) [42]. The diameter of QDs and their concentration are connected through extinction coefficient of NCs by Eq. 2.3–2.5, and the bigger nanoparticle diameters result in lower concentrations. This explains why the higher NC concentration for S/ODE precursor causes the CdS QDs to be smaller in size (from 1.8 to 3.4 nm) and bigger in the case of TOPS and TBPS (from 2.3 to 5.0 and 5.6 nm, respectively), where the NP concentration is low. Thus, our method allows to tune the sizes of CdS QDs in quite a big range, varying their growth time up to 2400 s.

To obtain a clear representation of the initial ligand shell composition of CdS NCs synthesized using different S precursors, we have fulfilled the ^{1}H NMR analysis of

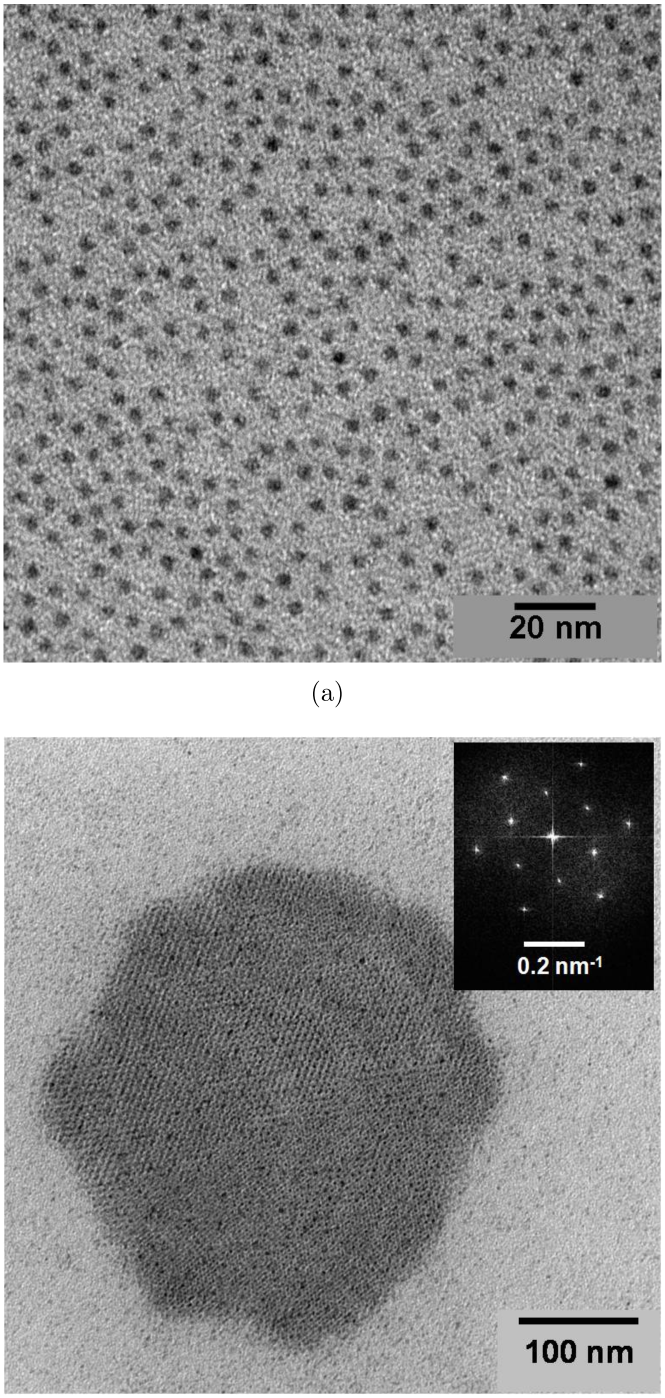

(a)

(b)

Figure 5.2: Representative TEM images of CdS QDs show monodisperse spherical nanoparticles and a small facetted crystal: (a) CdS NCs synthesized using TBPS (ratio Cd : S = 1 : 0.8), 400 µl of OA and the growth time of 2400 s; (b) CdS NCs synthesized using TBPS (ratio Cd : S = 1 : 0.2), 400 µl of OA and the growth time of 2400 s. Inset in (b) shows the FFT image of the same area.

the recovered ligands: the purified particles were destroyed by a DCl-D_2O solution and subsequently transferred into a $CDCl_3$ phase by vigorous shaking (see page 12) (Fig. 5.3). This method allows to investigate the ligands that are not bound to the surface. By comparing the ^{1}H NMR spectra of the recovered ligand shell from the as-synthesized CdS QDs (Fig. 5.3a, b, c) with pure oleic acid (Fig. 5.3d), one can clearly observe the presence of all typical OA peaks in the nanocrystal sample, i.e. at the same magnitudes of ppm as in pure OA. However, the integrals of the signals do

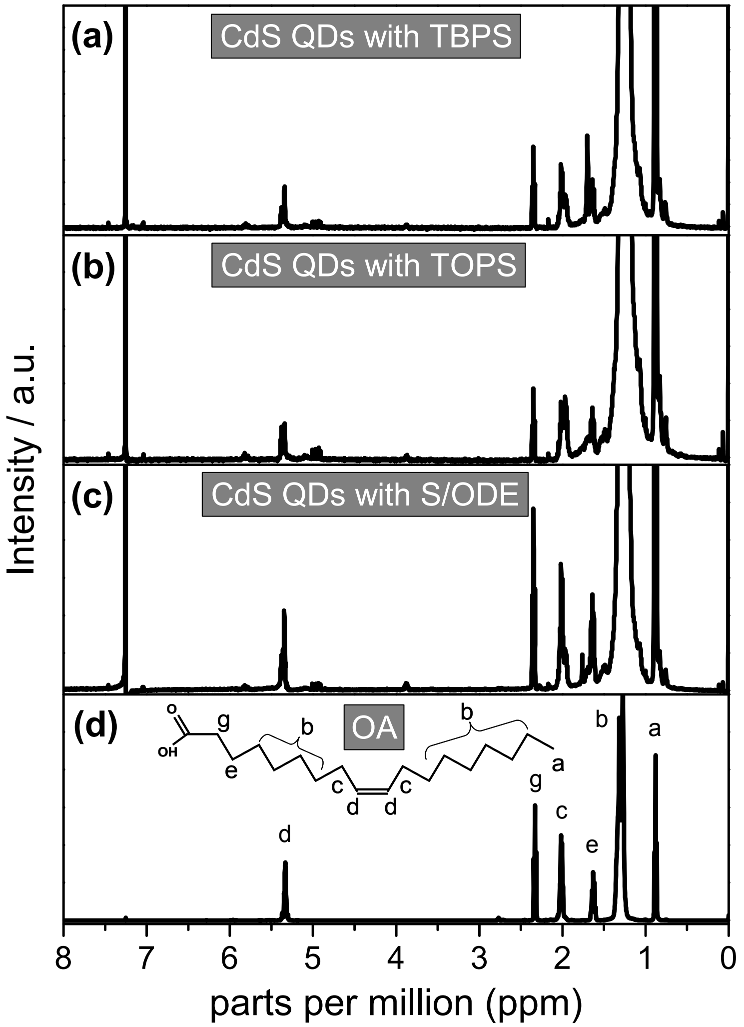

Figure 5.3: ^{1}H NMR spectra of the recovered ligand shell of (a) CdS QDs synthesized using TBPS; (b) CdS QDs synthesized using TOPS; (c) CdS QDs synthesized using S/ODE; (d) pure OA.

not match those of the pure OA. The intensity of the peak at 5.35 ppm corresponding to the double bond is much lower in the CdS samples in comparison to OA, which indicates the partial polymerization. This is consistent with the presence of oleic acid dimers in the mass-spectra of the cadmium oleate solution (not shown here). The ^{31}P NMR spectroscopy of the CdS nanoparticles produced using TOPS and TBPS detected no phosphorous compounds in the recovered ligand shell. Consequently, the CdS QDs independent of the used S precursor are capped only with oleic acid molecules.

A big reactivity of the S/ODE solution promoted us to investigate the nature of the chemical bonds in this precursor. The ^{1}H and ^{13}C NMR spectroscopy as well as mass-spectrometry measurements were used for its characterization. The mass spectrum revealed the presence of several compounds: ODE, ODE$-$S, ODE$-S_2$, ODE$-S_3$, ODE$-S_4$, ODE$_2-$S, ODE$_2-S_2$, ODE$_2-S_3$, ODE$_2-S_4$, as well as their decomposition products (Fig. 5.4a). However, the nature of chemical bonds between S and ODE is different from that in the Se/ODE solution. The ^{1}H NMR spectrum of a S/ODE precursor (Fig. 5.4b) clearly reveals the presence of the same structure as in the heated under N_2 ODE solution. The same concerns the ^{13}C NMR spectrum (not shown here), where peaks in the S/ODE precursor are located at the same magnitudes of ppm as in ODE. The integrals of the peaks at 4.96 and 5.79 ppm (Fig. 5.4b) belonging to the hydrogen atoms at the double bond of ODE do not change, which suggests that there are van der Waals forces between S and ODE molecules. For Se/ODE precursor solution it was different, one saw the obvious changes in both ^{1}H and ^{13}C NMR spectra, which implies the presence of covalent forces between Se and ODE molecules.

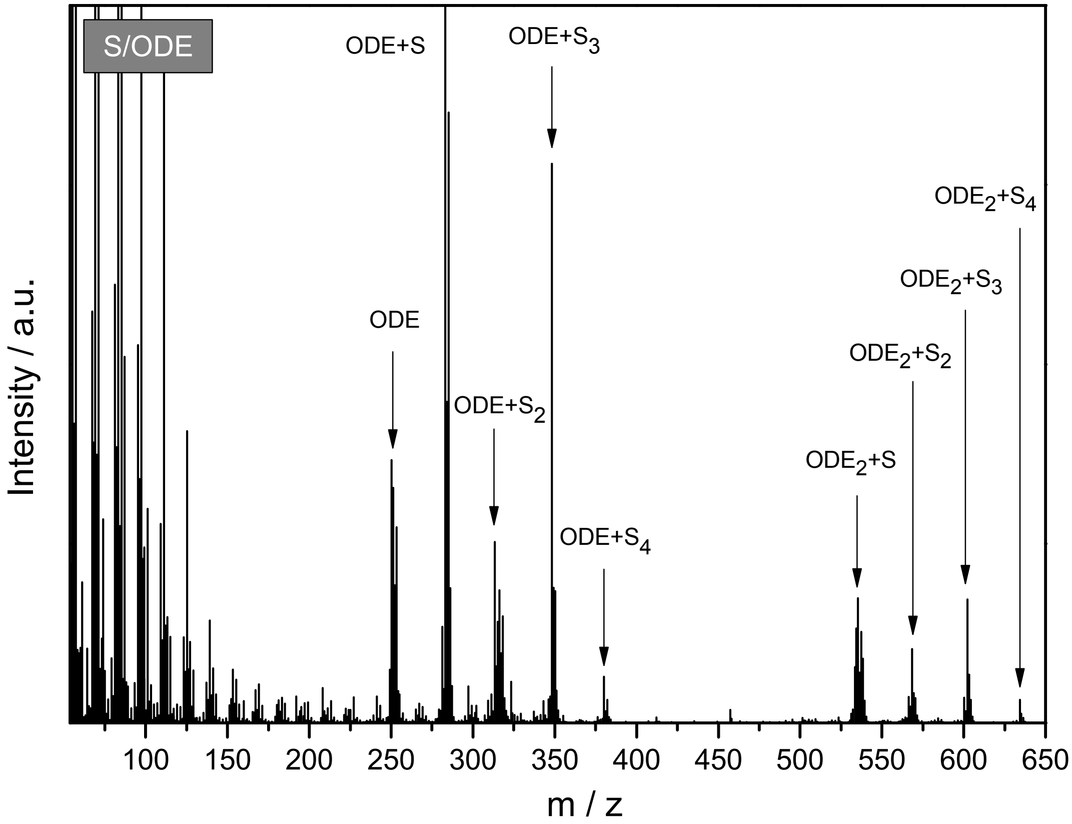

(a)

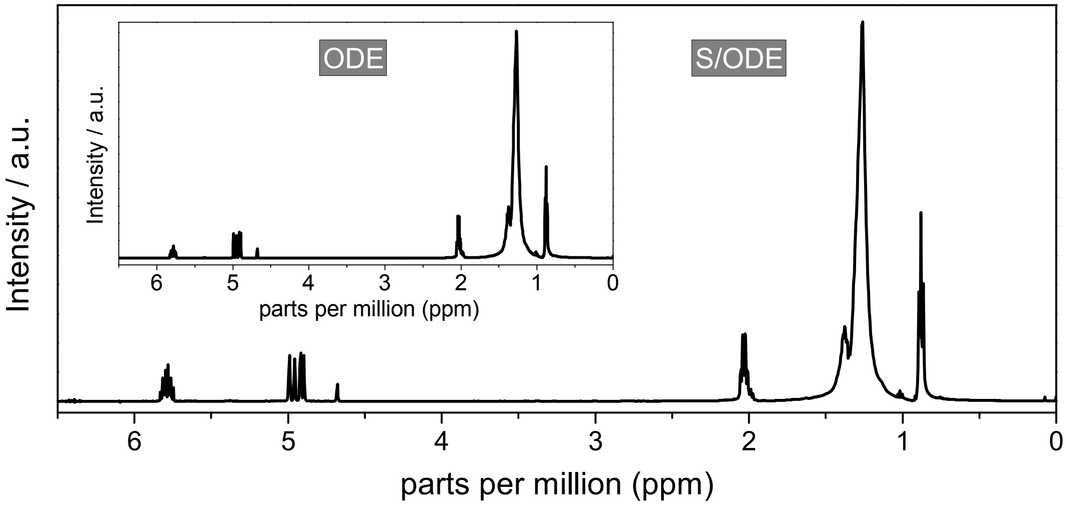

(b)

Figure 5.4: Investigation of the S/ODE precursor solution: (a) mass spectrum; (b) ^{1}H NMR spectrum. Inset in (b) depicts the ^{1}H NMR spectrum of heated under nitrogen ODE.

5.3.2 Study of magic-sized nanoclusters during the formation of CdS NCs

In our work, two well distinguishable persistent absorption peaks at 312 and 319-322 nm corresponding to MSNCs were repeatedly observed in the CdS system. The congeneric MSNCs species of CdS, having absorption maximum at 311-312 nm and 323-324 nm, have also been previously reported by Pan et al. [129][121], Yu et al. [130][122], Ouyang et al. [113] and Li et al. [123].

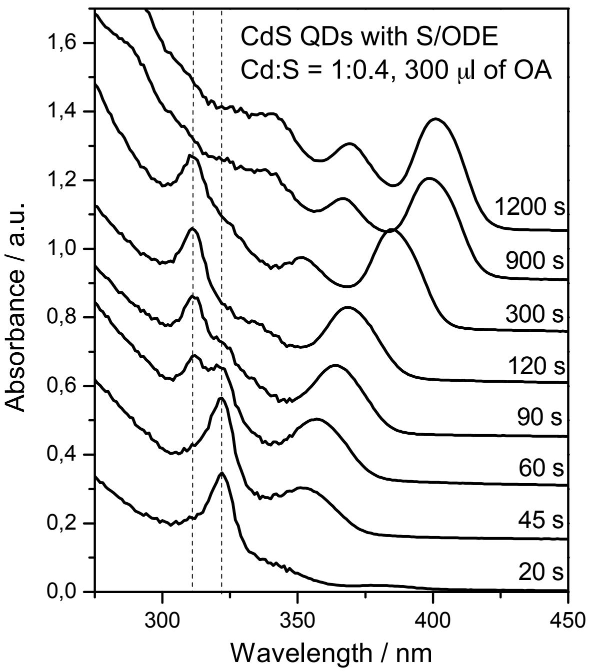

Figure 5.5: Temporal evolution of the absorption spectra in the reaction Cd : S = 1 : 0.4, 300 µl of OA with S/ODE. The two dashed lines are for visual guidance to show two families of MSNCs.

Fig. 5.5 depicts the temporal evolution of UV-Vis absorption spectra in the synthesis of CdS QDs with initial molar excess of Cd and S/ODE as a S precursor. In the beginning of the reaction, i.e after 20 s, one can clearly see the sharp peak at 322 nm corresponding to MSNCs. During the further heating, the formation of RNCs starts which is evident as appearance of the absorption above 350 nm. In this thesis, the term “nanocrystals (NCs)” only refers to those with regular sizes, to distinguish them from so-called magic-sized nanocrystals. The red-shift of the first absorption peak with increasing of the residence time indicates the growth of CdS NCs during synthesis. After 60 s of the growth, the additional peak at 312 nm corresponding to another family of MSNCs appears, accompanied by the decrease in the peak's intensity of the 322 nm MSNCs family. Then the 322 nm MSNCs family disappears completely, whereas the signal of MSNCs at 312 nm increases in its intensity. Such transfer from one MSNCs species to another indicates that the 322 nm CdS MSNCs possess lower stability than 312 nm CdS MSNCs, which is consistent with the results from literature [122]. However, after 900 s of the reaction (Fig. 5.5), no peak corresponding to MSNCs can be observed, which implies that all MSNCs grew into regular NCs. The fact that the MSNCs are present in the solution earlier (after 20 s) than regular NCs (after 45 s) indicates that they act as nuclei to initiate the growth of NCs. Thus, the MSNCs are intermediate species in the synthesis, which is evident by intensity variation of the 322 and 312 nm peaks and their complete disappearance at the later stages of the reaction. The life span of MSNCs depends on the reaction temperature and can be prolonged to over 2 hours at lower temperatures (e.g. 110 ℃) [122].

The nucleation and growth details can be studied by observing the mean absorption-derived NC characteristics during the synthesis, such as diameter, concentration, total volume (product of concentration and volume of a single particle), and growth rate (increase in the volume of a nanoparticle with time). Fig. 5.6 plots these values from 45 to 1200 s of the NC residence time. The mean diameter grows continuously throughout the whole recorded period (Fig. 5.6a). There is no significant increase in the concentration in the beginning of the reaction (Fig. 5.6c), which means that the nucleation stage is bypassed quickly and only the growth stage is monitored. The separation of the nucleation and growth stages is considered to be a prerequisite of producing highly monodisperse NCs, which was achieved in our experiments by using

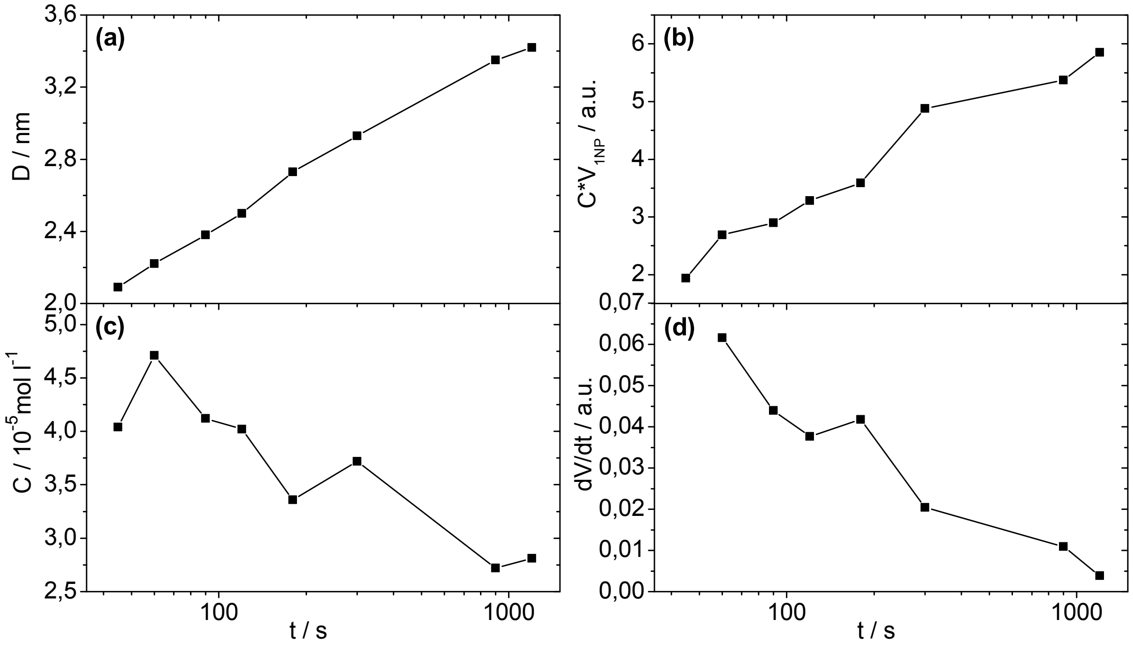

Figure 5.6: Temporal evolution of calculated from absorbance (a) diameters; (b) total volumes; (c) concentrations; (d) growth rates of regular-sized NCs in the reaction Cd : S = 1 : 0.4, 300 µl of OA with S/ODE.

higher injection (300 °C) and lower growth temperatures (270-280 °C). The concentration stays almost invariable in the first 300 s of the reaction and decreases slightly afterwards (Fig. 5.6c). However, it should be noted that it is not necessarily the Ostwald ripening stage since the absorption spectra do not broaden. On the contrary, the size distribution focuses to some extend during the course of the reaction: hwhm of the absorption spectra changes from 15 to 12 nm (not shown here) for the aliquots taken out after 45 and 1200 s of the growth, respectively. From the temporal evolution of total volume and concentration (Fig. 5.6b, c), it can be seen that the concentration does not decrease during the first 300 s of the reaction, whereas the total volume rises substantially. This indicates that the monomer concentration is high enough in the first 300 s and then reduces. Fig. 5.6d shows the gradual decrease of the NC growth rate with time, which is in agreement with the monomer consumption during the synthesis.

The PL spectra also provide some information about the reaction kinetics and quality of as-synthesized NCs. Fig. 5.7 represents the UV-Vis absorption and photoluminescence spectra of fresh synthesized CdS QDs. Two types of emission bands can be detected: the band-edge PL and the deep-trap PL (Fig. 5.7b). However, the latter is negligible in comparison to the former one, which indicates a high quality of the obtained NPs. The full width at half-maximum (fwhm) of the band-edge PL and half-width at half-maximum (hwhm) on the longer wavelength side of the absorption spectra, which can be used to estimate the QD size distribution, do not change significantly in the course of the reaction and are 16-20 and 12-14 nm, respectively. This indicates that the produced NCs are monodisperse, and that the Cd^0 precipitate used as a Cd precursor results in the formation of good quality CdS QDs without Ostwald ripening at the later stages of the reaction. From the PL spectra it can be also seen that the PL intensity, proportional to quantum yield, increases with residence time of NCs and reaches its maximum value after 300 s of the growth, which is maintained during the next 15 min of the reaction (Fig. 5.7b).

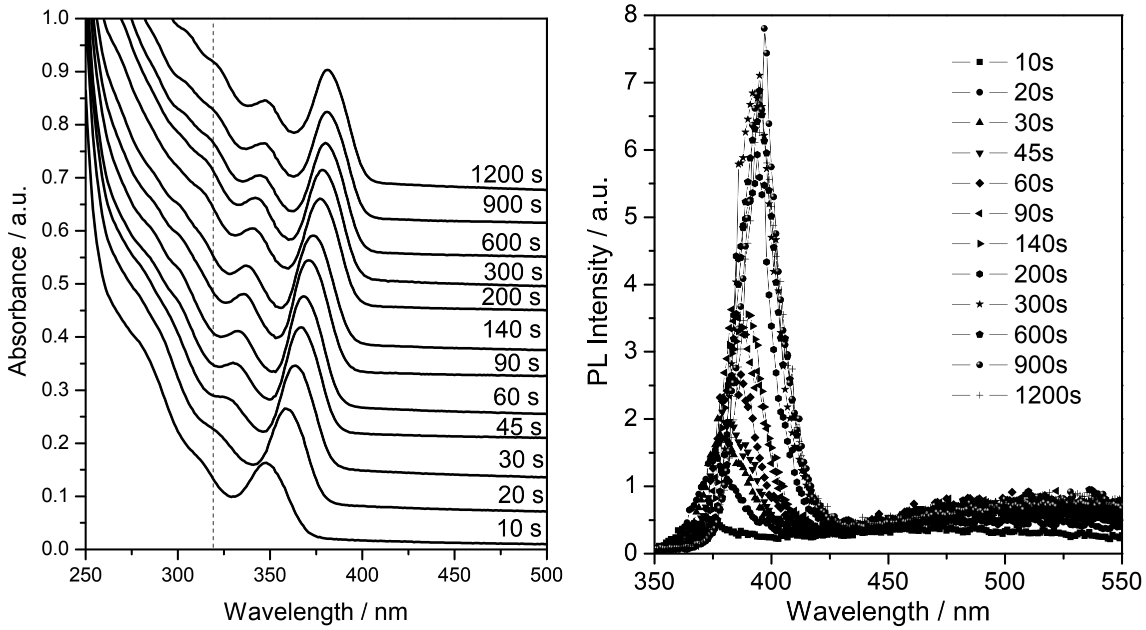

(a) (b)

Figure 5.7: Temporal evolution of (a) UV-Vis absorption; (b) PL spectra of fresh CdS QDs synthesized with S/ODE, Cd : S = 1 : 0.2, 400 µl of OA.

Due to their extremely small sizes, the MSNCs should only be stable at relatively high monomer concentrations. In other words, the existence of the nanoclusters can be considered as an indicator of the high monomer concentration in the reaction solution [78]. This assumption is proved by our results: the MSNCs are present only during the first 300 s of the reaction (Fig. 5.5), when the concentration of regular NCs is maintained at the same level (Fig. 5.6c), indicating that the monomer concentration is high enough. To investigate the change in the monomer concentration, an additional experiment was carried out, viz. AAS measurements of the amount of Cd^0 precipitate at the bottom of a vial with a CdS crude solution after the centrifugation (Fig. 5.8). It can be seen that for all investigated Cd : S ratio the amount of precipitated Cd^0 decreases in the first ca. 120 s of the reaction, which means that it dissolves producing additional monomers for the formation of CdS QDs. Then the concentration of Cd^0 increases substantially (from 4 to 36 %) after 120 s only in the reaction with a big excess of Cd, i.e. Cd : S = 1 : 0.2, since the S precursor is completely consumed at this stage in the synthesis of CdS NCs. As usual, in different Cd : S ratio reactions, the amount of the Cd precursor is kept constant while varying

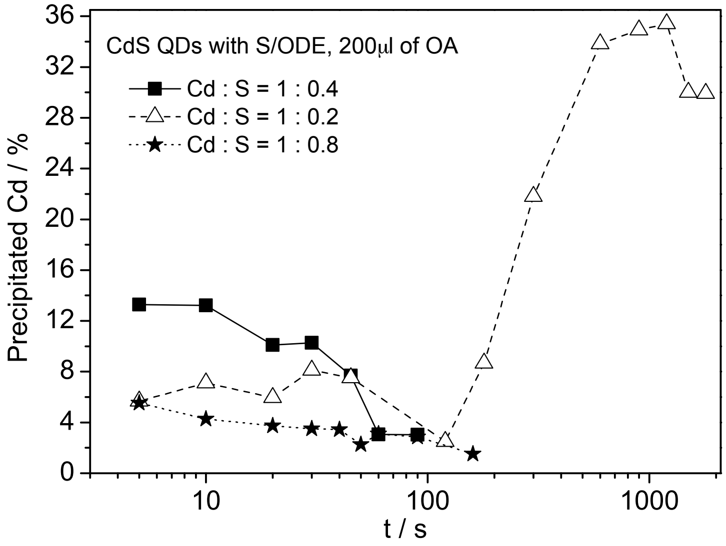

Figure 5.8: AAS measurements of Cd^0 precipitate in the reactions with S/ODE, 200 µl of OA and different Cd : S ratio (1 : 0.2, 1 : 0.4, and 1 : 0.8).

the amount of the S precursor. However, in the reactions Cd : S = 1 : 0.4 and 1 : 0.8, the Cd^0 precipitate is entirely used after 120 s of the reaction. This indicates that Cd^0 particles provide a constant monomer supply only in the first ca. 120 s of the NC growth, which is highly consistent with existence of MSNCs only in the beginning of the reaction.

Our systematic studies have shown that the formation of the CdS MSNCs is favored with high Cd : S (1 : 0.2, 1: 0.4, and 1 : 0.8) initial molar ratio, which is in agreement with the growth of CdS and other semiconductor MSNCs [123][131][132]. For instance, Li et al. also obtained two families of CdS MSNCs (with the absorption at 324 nm and 378 nm) under the 4Cd/1S feed molar ratio [123]. The species absorbing at 324 nm were intermediate, the same as in our synthesis, but then they grew into 378 nm magic-sized species. Such formation of MSNCs means that they possess the enhanced thermal stability under high Cd^{2+} concentrations. Additionally, Pan et al. studied 311 nm absorbing CdS MSNCs with EDX and revealed that they are composed of Cd and S with an atomic ratio of 2 : 1, because the outermost layer of the nuclei is composed mainly of Cd atoms [121]. In our reactions, CdS MSNCs were produced in Cd-rich reactions (at early stages) not only in the case of S/ODE as a S precursor, but also with TOPS and TBPS. This implies that independent of the used S precursor, CdS NCs were produced via the same synthetic mechanism, where intermediate CdS MSNCs acted as nuclei with a minimum critical size that could be formed.

In almost all previous reports concerning research on the magic-sized semiconductor nanocrystals, it was shown that the stages of their appearance can only take place at temperatures similar to those needed for the growth of regular NCs [122]. Surprisingly, the analysis of the absorption spectra of our CdS QD samples kept for some time has revealed that the formation of magic-sized CdS nanocrystals can be induced at room temperature. Fig. 5.9a shows absorbance of the same CdS samples as in Fig.

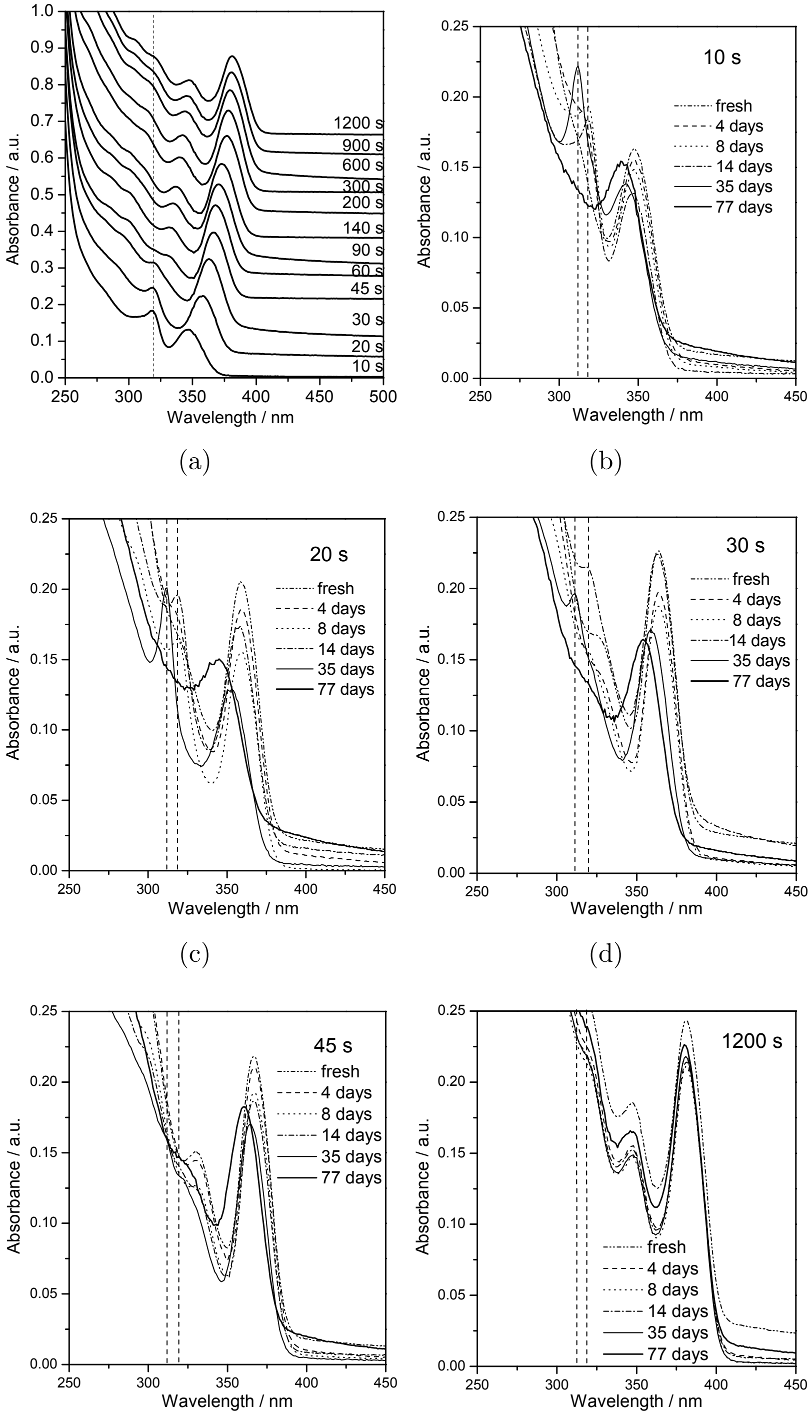

(a) (b)

(c) (d)

(e) (f)

Figure 5.9: Evolution of the UV-Vis absorption spectra at room temperature: (a) 14-days-old CdS QDs synthesized with S/ODE, Cd : S = 1 : 0.2, 400 µl of OA; (b), (c), (d), (e), and (f) CdS QDs for different dates of measurements and different residence time: 10, 20, 30, 45, and 1200 s, respectively.

5.7a, but after 14 days of storage at room temperature in the dark. It is evident that the spectra of the first 3 aliquots (10-30 s) changed with the formation of MSNCs with the absorption peak at 322 nm (the dashed lines are used for visual guidance). The detailed analysis of several CdS QD samples with growth times of 10, 20, 30, 45, and 1200 s is represented in Fig. 5.9. As it was already mentioned, the fresh samples have absorption peaks corresponding to regular NCs. After 4 days, their UV-Vis absorption spectra changed and one could notice a small maximum of MSNC at 319 nm for 10 and 20 s aliquots. After 8 and 14 days from the synthesis, this maximum became more pronounced, so that it could be well distinguished for 10, 20, and 30 s samples. These MSNCs absorbing at 319 nm seem to be unstable, since they later transformed to another species of the MSNCs with a very narrow absorption peak at 312 nm (after 35 days) with a hwhm of 6 nm. Not only the wavelength changed from 319 to 312 nm, but the MSNCs' peak intensified as well, once again indicating a higher stability. Consistently, absorption intensity of the regular NCs decreased for the samples stored for 35 days, which is caused by competition between MSNCs and regular NCs, resulting in dynamical evolution of their concentration. However, after 77 days, both regular CdS NCs and MSNCs are likely to decompose and afterwards disappear. Interestingly, these transformations take place for the CdS NCs at earlier stages of the reaction (Fig. 5.9b, c, d), and the UV-Vis absorption spectra of CdS NCs with a bigger residence time (45-1200 s) (Fig. 5.9e, f) undergo almost no changes. This fact implies that the MSNCs formed under high monomer concentration conditions may have grown very quickly into regular NCs due to high injection/growth temperature and their existence could not be recorded in the absorption spectra. But after some time, the solution tended to attain a more energetically beneficial state, bringing about the formation of MSNCs first absorbing at 319 nm and then even more stable MSNCs at 312 nm with increased intensity. A similar transformation at room temperature of the 323 nm CdS MSNCs to the 312 nm MSNCs after 10 days of storage was reported by Yu et al. [122].

Presumably, several reasons exist as to why bigger NCs (beginning from a residence time of 45 s) do not transform into MSNCs at room temperature. First, as already mentioned, the formation of MSNCs is favored under high monomer concentration, i.e. for samples taken out in the first seconds of the reaction. Second, big NCs possess enhanced stability (unlike small particles), since they are not so easy to dissolve according to the Gibbs-Thomson effect (see page 23).

Investigation of properties of MSNCs is challenging due to their small sizes, especially the determination of their diameters often leads to controversial results. Thus, Li et al. [123] estimated the diameter of 378 nm MSNCs family to be 2.7 nm from absorbance, 3-4 nm from TEM, and 1.9 nm from diffusion ordered NMR spectroscopy (DOSY). Relying on another result from literature [133], where 358 nm absorbing $Cd_{32}S_{50}$ nanoclusters had a size of 1.5 nm, they draw a conclusion that the diameter determined from the diffusion coefficient was the closest to the real value. In our case, the absorption-calculated size of 312 nm MSNCs is 1.5 nm, however, the real diameter should be smaller. Pan et al. found the size of 311 nm CdS MSNCs to be 1.32 nm by means of dynamic light scattering (DLS) measurements [121]. They have also observed that size of MSNCs is independent of the monomer or capping agent concentration, solvent, and reaction temperature. This once again underlines that the 311-312 species of CdS MSNCs seem to be the most stable.

5.3.3 Possible nucleation-growth mechanism

Formation of MSNCs in the course of the reaction should shed some light on the nucleation step. MSNCs undergo the stages of appearance and disappearance instead of focusing and defocusing stages of regular-sized NCs [134]. When the monomer concentration is high enough, they will appear and disappear again, when the monomer concentration decreases. Additionally, it is known that the decrease of injection/growth temperatures reduces the monomer activity and hence prolongs the existence of magic-sized nanocrystals [122][134]. Thus, after injection of a S precursor, our reaction begins with a nucleation stage where magic-sized nuclei are formed. These MSNCs have a very narrow size distribution, which remains almost constant during the whole time. Afterwards, they gradually transform into regular-sized NCs. According to the literature, the evolution of MSNCs into regular-sized NCs can be realized in different ways:

1. deposition of a large amount of monomers on the MSNCs almost instantaneously followed by one-dimentional (1D) or three-dimentional (3D) growth [78]
2. quantized growth of NCs through aggregation of MSNCs and subsequent monomer induced growth [135] or quantized fusion (combination of quantized aggregation and cluster fusion) [85]
3. dominant growth of NCs at the expense of MSNCs due to their Ostwald ripening [121]
4. forward/backward tunneling[1] mechanism, where some part of MSNCs grows to NCs and some decomposes back to monomers [122]

The first mechanism, proposed by Peng et al. [78], cannot be the main mechanism in our case, since the growth of 1D or 3D nanoparticles from MSNCs is not observed in our system. The second mechanism of Dagtepe et al. [135] or the similar mechanism of Sun et al. [85], i.e. aggregation growth (with subsequent fusion with monomers), could be possible in our system, however, challenging determination of the exact size and difficulty in obtaining TEM images of MSNCs make the analysis complicated. The third mechanism, assumed by Pan et al. [121], which includes dissolution of

---

[1] A "forward/backward tunneling" mechanism was originally proposed by Peng and co-workers suggesting that the MSNC species can "tunnel" through the thermodynamic barriers [78].

MSNCs in terms of the Ostwald ripening process could also take place in our reaction, however, we observed not only the formation of regular-sized NCs from magic-sized ones, but the opposite trend as well (implying that NCs and MSNCs stay in equilibrium). The fourth mechanism of Yu et al. [122] (Fig. 5.10), resembling to some

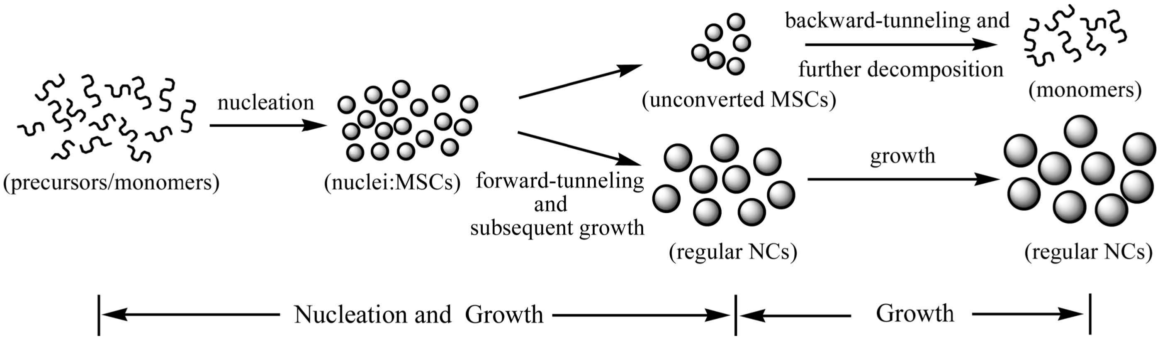

Figure 5.10: Proposed by Yu et al. [122] mechanism of MSNC-nucleated growth of CdS NCs. In the scheme, “MSC” is the abbreviation for magic sized crystals.

extend the aggregation scheme of Dagtepe et al. and the Ostwald ripening growth scheme of Pan et al., suggests that the MSNCs undergo “forward-tunneling” forming species close in their wavelength to regular NCs and which grow subsequently to NCs, or “backward-tunneling”with further decomposition to monomers. In our case, no intermediate sized clusters/crystals between MSNC and RNCs have been observed and this is why no “forward-tunneling” can be detected. Instead, one can suggest that “backward-tunneling” takes place when the 322 nm MSNCs transform into more stable 312 nm MSNCs. Both 322 and 312 MSNC species can transform into RNCs, which is evident by Fig. 5.5 on page 80. Although it is difficult to exclude Ostwald ripening completely, we believe that the aggregation/coalescence growth mechanism [135], presumably followed by fusion with monomers [85], is at least the dominant mechanism since we observe the reverse process, i.e. formation of MSNCs from RNCs at room temperature. The aggregation/fusion process should be very rapid, or even instantaneous, because no intermediate species can be observed. Taking all aforementioned into consideration, we tentatively propose a nucleation-growth mechanism for the formation of the CdS NCs from MSNCs (Fig. 5.11).

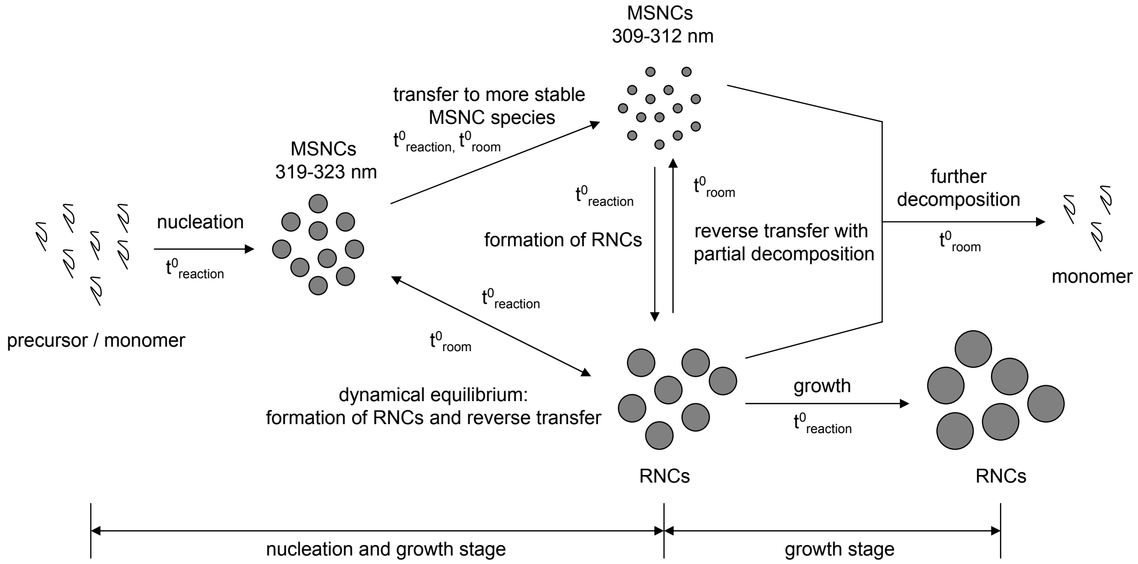

Figure 5.11: A possible nucleation-growth mechanism in our CdS reaction system. "MSNCs" and "RNCs" are the abbreviations for magic-sized nanocrystals and regular-sized nanocrystals, respectively; t^0_{reaction} and t^0_{room} indicate the reaction and room temperature, respectively.

As depicted in Fig. 5.11, after injection, the MSNCs form initially and act as nuclei to produce regular-sized NCs, absorbing above 350 nm. The resulting secondary particles grow further into stable regular NCs which cannot transfer back to MSNCs (Fig. 5.9f). The 319-323 nm MSNCs reduce to another family of more stable MSNC species absorbing at 309-312 nm, which in turn can grow to RNCs (Fig. 5.5 on page 80). The concentration of regular NCs remains almost invariable during the whole growth stage (Fig. 5.6c). Remarkably, not only the MSNCs can transfer into RNCs, but the reverse process takes place at room temperature, suggesting the dynamical equilibrium between them. As it can be seen from Fig. 5.9b, c, d (after 8 and 14 days of storage), under the transfer of RNCs into 319-323 nm MSNCs, the concentration of RNCs reduces, but the wavelength does not shift. However, after 35 days, when the 309-312 nm MSNCs form, not only the concentration decreases, but the wavelength shifts into the blue region indicating the partial decomposition of RNCs. Subsequently, when the MSNCs disappear at all (after 77 days), the absorption intensity of RNCs increases (in comparison to the sample after 35 days in Fig. 5.9b, c, d) indicating the conjugation of MSNC into/with RNCs with further decomposition of RNCs (as evident by a more pronounced wavelength shift of the absorption maximum). Although an aggregation/coalescence/fusion scheme could be possible in our reaction, the detailed mechanism of transformations between MSNCs and RNCs is challenging and needs further intensive experimental investigation. Nevertheless, we believe that our work provide some understanding of the transformations between MSNCs and NCs during the synthesis and storage.

5.4 Conclusions

To summarize, high quality CdS QDs with a very narrow size distribution (proved by UV-Vis absorption and TEM measurements) were synthesized using a novel method with Cd^0 precipitate as a Cd precursor and three different S precursors: S/ODE, TOPS, and TBPS. The analysis of the ligand shell revealed that independent of the S precursor, CdS NCs are capped with oleic acid molecules. The role of the CdS MSNCs as intermediate species during the synthesis of CdS QDs was investigated. Based on the studies, a plausible nucleation-growth mechanism was proposed for the formation of CdS NCs from the MSNCs.

Chapter 6

Surface modification of CdSe nanocrystals

This chapter describes the investigation of the surface shell composition of both as-synthesized CdSe QDs and pyridine-treated QDs. It was demonstrated that although two types of possible surfactants are present in the synthesis, viz. oleic acid (OA) and tri-n-octylphosphine (TOP), the obtained NCs are OA-capped without presence of TOP molecules in the ligand shell. NMR techniques were applied to determine the composition of the ligand shell as well as to distinguish the bound and free ligands before and after the ligand exchange. It was shown that after one-fold pyridine treatment some amount of OA was still present in the sample, which motivated us to fulfill the repeated steps of the ligand exchange. By using thermal gravimetric analysis (TGA) we could obtain quantitative information about the effectiveness of subsequent pyridine treatments.

6.1 Motivation and review of the literature

Presently, colloidal CdSe nanocrystals (NCs) are the most investigated object among inorganic semiconductor nanoparticles. Their synthesis has achieved a big progress resulting in a high size and shape monodispersity, as well as good optical properties. NCs consist of an inorganic core that is surrounded by a layer of organic ligands. This surface organic ligand shell is critical for the properties of NCs [136][137]. Thus, to adjust the reactivity and obtain different sizes and shapes of CdSe NCs, most of the previously published methods were focused on the use of different organic ligands, such as fatty or long carbon chained carboxylic acids (e.g. oleic acid [138][139][38], myristic acid [92], stearic acid [140]), amines (e.g. hexadecylamine [141], octadecylamine, dioctylamine) [142], alkyl thiols [143][144], alkyl phosphines (e.g. TOP, TBP), alkyl phosphine oxides (e.g. TOPO) [145], phosphonic acids (e.g. octadecylphosphonic acid, hexylphosphonic acid, tetradecylphosphonic acid [79][26]), etc. These capping molecules are responsible for stable colloidal solutions of NCs, preventing irreversible aggregation, coagulation, and fusion of the NCs due to van der Waals interactions. However, in many cases, the surfactants of as-synthesized CdSe nanoparticles are not suitable for their further processing and a modification of the original surface cap with other ligands is required for a desired application. By ligand exchange it is possible to achieve different goals:

- One can derivatize the surface so that the hydrophobic ligands will be exchanged by hydrophilic ones, which is usually used for biological applications in order to obtain water-soluble particles originally synthesized in the organic medium [146].
- Moreover, it is possible to enhance the quantum yield (QY) of the nanocrystal sample, which finds its applications in biomedical labeling. For example, ligand exchange of TOPO with n-hexadecylamine, n-dodecylamine, and allylamine can

result in an order of magnitude increase in QY of CdSe QDs [65].

- Furthermore, introducing new functional groups onto the surface can be useful to obtain nanoparticles with different properties. Such a surface functionalization process can be carried out with any compound capable of coordinating or bounding to the surface of the nanocrystal including, for example, different phosphines, phosphates, thiols, amines [146], carboxylic acids, polymers, dendrons [147][148], etc.
- Finally, one can reduce the thickness of the nanoparticles ligand shell to permit electron and hole transfer between NCs and organic semiconductors for their applications in optoelectronic and photovoltaic devices. An exchange of the original ligand shell by smaller molecules is important for photovoltaic applications since bound to the surface ligands after the synthesis usually consist of long carbon chains and form a barrier to charge carriers [149].

In our study, we are mainly concerned with the ligand exchange aimed to improve the performance of photovoltaic devices and in particular, hybrid polymer/NCs solar cells. Previously, exchange of the initial ligand shell usually consisting of "long" organic molecules (e.g. OA has length of ca. 2 nm [150]) with "short" pyridine molecules (a nitrogen-containing aromatic-ring structure, ca. 0.6 nm [151]) was successfully used to enhance charge transfer for the production of solar cells. It is known that pyridine binds mostly to the surface Cd atoms [152][153] replacing the original ligands when it is used in excess and the sample is heated. Due to the compactness of pyridine molecules, the nanocrystal-polymer distance decreases upon formation of the composite during heat treatment and the electron transfer from/to QDs is facilitated [149]. Another advantage of pyridine is that it can be removed through thermal evaporation easier than TOP/TOPO, fatty acids, or other long-chained ligands.

In one of the first and most cited references concerning synthesis of semiconductor nanoparticles by Murray et al., the authors did the ligand exchange with pyridine.

They noticed that exposure of purified NCs originally coated by TOP/TOPO to a large excess of pyridine at 60 ℃ begins the exchange of the surface cap. The exchange of surface ligands can be followed by change in the solubility of NCs since pyridine capped NCs are dispersible in polar solvents and aromatics, but not in aliphatics. However, at this stage, the procedure of the pyridine treatment was not perfect and the obtained NPs exhibited a slightly bigger size and a small broadening of the size distribution.

Since then, further investigations have led to significant improvements in the techniques of the pyridine treatment. Several runs of heating for 3-5 hours at 60 ℃ [154] or sonification [155] procedure of the purified nanoparticles in pyridine were proposed, which resulted in good properties of pyridine-treated QDs. Thus, the absorption spectra of the NCs after ligand exchange remained the same as that of as-synthesized nanoparticles indicating that no oxidation and aggregation of the semiconductor NCs occurred. Oxidation reduces the size of the nanocrystals and can be detected as a blue shift in the absorption spectrum. Aggregation of the nanoparticles, on the contrary, leads to the increase in size and therefore causes the red shift of the absorption spectrum. That is why after successful cap exchange, the main absorption features such as peak position and contour should be maintained in their original state. It was reported that after pyridine treatment, a quantum yield (QY) of semiconductor NCs is quenched substantially [156], however, it plays no role for solar cells fabrication and is even desirable for Raman spectroscopy measurements which were carried out using the nanoparticles from this thesis in reference [157].

Despite the evident importance of surface exchange reactions of semiconductor NCs with organic ligands for both the fundamental understanding of QDs properties and their numerous applications, surfaces of NCs are poorly investigated. To achieve a successful ligand exchange, it is necessary to study both the initial and modified ligand shell in detail. Such knowledge would allow a more rational approach to surface modification methodologies with retention of the semiconductor core's desirable optical properties. Usually, the efficiency of the exchange is limited by the difference in binding strengths of new and old ligands to an inorganic core of NCs. Fatty acids (such as oleic acid) and alkyl phosphines/phosphine oxides (such as TOP/TOPO) are considered to be strong ligands, whereas pyridine is regarded as an extremely weak bonding ligand. That is why usually replacing the original ligand shell completely with pyridine molecules is not possible both by a single pyridine treatment and even by repeated steps of pyridine treatment. For instance, literature data suggest that in the case of TOPO ligands, approx. 10-15 % of TOPO still remain on the surface [158][154]. Zhang et al. [147] fulfilled the ligand exchange of the originally TOP/TOPO coated CdSe NCs by heating the CdSe sample in pyridine at 65 ℃ for 1 hour and subsequently precipitating the particles with hexane. Surprisingly, even after seven repeated cycles of the pyridine treatment, still some amount of residual phosphorus was present in the ligand shell (evidenced by ^{31}P NMR analysis). Thus, the pyridine ligand exchange was mostly investigated for the case of initial TOPO ligands. However, to our knowledge, research on the pyridine treatment of the originally oleic acid coated CdSe QDs was not conducted, which will be introduced in this thesis. Additionally, although pyridine treatment was often applied, the quantitative studies of the extent of surface modification of NCs are limited. Suitable quantification includes the determination of the amount of initial ligands released from the surface or the amount of the new species of the alternative ligands bound to the NCs. Moreover, it is still unexplored how the pyridine ligand exchange influences the stability of colloids, the tendency for aggregation of the nanoparticles, and surface defects. For these reasons, the exact information of the composition of the ligand cap both after a single and multiple pyridine treatment can be highly important for end applications of these NCs. Our studies should shed new light on this important subject – ligand and surface chemistry of high quality nanocrystals.

As it was already mentioned, to attain a successful ligand exchange, the precise understanding of the original ligand shell composition should not be underestimated. In some reactions, more than one of possible stabilizing molecules are present during the synthesis and it is essential to determine which molecules are bound to the surface and which not. For example, in the synthesis of CdSe NCs in octadecene involving both oleic acid (OA) and TBPSe by Bullen et al. [58] (or TOPSe by van Embden et al. [55]), which is closely related to the topic of this work, there are two possible candidates for the ligand shell: OA and TBP (TOP). The authors studied the reaction kinetics and reported that oleic acid is an efficacious capping agent for CdSe QDs, since it caps the nuclei rapidly as they form. The so-synthesized CdSe QDs were used for the production of quantum-dot sensitized solar cells, and it was reported that they are OA-capped [38]. However, to our knowledge, the exactly composition of the ligand shell was not studied and the presence of TBP (TOP) molecules in the ligand shell was not ruled out.

In this thesis, CdSe QDs were synthesized using both OA and TOPSe. First, the ligands bound to the surface were investigated and it was proved that as-synthesized QDs are only OA-capped, without the presence of TOP molecules in the ligand shell. That is why original CdSe QDs will be further denoted as CdSeOA QDs. Second, the effect of one-fold, and later multiple pyridine treatment on the surface of CdSe NCs initially capped with OA was studied. These samples will be further referred to as CdSePy1 QDs for the first step of the pyridine treatment, CdSePy2 and CdSePy3 QDs for the second and third steps of the pyridine treatment, respectively. The composition of the initial and the final (after the ligand exchange) ligand shell was investigated by means of nuclear magnetic resonance (NMR) spectroscopy and thermal gravimetric analysis (TGA). It was shown that after one-fold pyridine treatment some amount of OA was still present in the sample, which motivated us to fulfill repeated steps of the ligand exchange. The absorption spectra after repeated pyridine treatment revealed that no aggregation or oxidation of the nanoparticles in solution occurred. TEM images were used to characterize the successive steps of the ligand exchange as well. The suitability of differently treated CdSe QDs for their application in hybrid solar cells was studied[1].

6.2 Results and discussion

Absorption UV-Vis spectroscopy, powder X-ray diffraction (XRD), transmission electron microscopy (TEM), and high resolution TEM (HRTEM) are the standard procedures to characterize the nanoparticles. To settle special questions (such as composition of the ligand shell), several methods are used, viz. nuclear magnetic resonance (NMR), thermal gravimetric analysis (TGA), etc. In our work, in the first step, the composition of the original ligand shell of as-synthesized CdSe QDs was studied. Then investigation of the ligand cap after the pyridine treatment was carried out.

The substitution of initial ligands with pyridine molecules was at first sight observed by change in the solubility of the NCs. As-synthesized nanoparticles dissolve mostly in all non-polar solvents, such as hexane, toluene, and chloroform, whereas after the ligand exchange, the surface of the quantum dots becomes polar and they dissolve well in pyridine (but no longer in hexane). Since chloroform is a low-polar solvent, the pyridine-treated QDs dissolve in it as well, however, the solubility in this case is marginal.

---

[1] The solar cell preparation and investigation will be discussed in Chapter 7.

6.2.1 Study of the composition of the original CdSe QDs ligand shell

The composition of the initial ligand shell of as-synthesized CdSe QDs was investigated by means of ^{1}H and ^{31}P NMR spectroscopy. NMR spectroscopy allows both the analysis of composition of the ligand shell and distinguishing between bound and free ligands. In order to receive detailed information about the ligand shell, it is advisable to analyze both the intact purified solid of nanoparticles and the recovered ligands, since different information can be obtained in both cases. The signals of ligands bound to the surface are usually broader than those of free ligands, they can be shifted, or some of them can even disappear. This can be seen in the NMR spectra of the intact particles. Signals coming from parts of the ligands being in the direct neighborhood of the surface are influenced in the strongest way, that is why the composition of the ligand shell can be reliably studied only if the ligands are not bound to the surface. In this sense, NMR spectra of the recovered ligands are necessary for the precise analysis of the ligand shell. They also help to find out in which state the bound ligands are (unchanged, polymerized, decomposed, etc.) by comparing integrals of the recovered spectra with those of a pure substance. To obtain the recovered ligands, purified NCs are destroyed by a DCl-D_2O solution with a subsequent extraction into a $CDCl_3$ solution by vigorous shaking.

CdSe NCs, synthesized in our work, grew in the presence of two types of possible surfactant molecules – OA and TOP. ^{31}P NMR spectroscopy of both intact and destroyed by a DCl-D_2O solution CdSe QDs was applied to determine the presence/absence of phosphorus compounds in the ligand shell. Thus, the ^{31}P NMR analysis did not prove the presence of any phosphorus compounds both in the intact and recovered ligand cap of the NCs. Since no phosphorus compounds were detected in the recovered ligand shell, the possibility that TOP is present on the surface of the QDs, but not measurable due to the immobilization on the surface, can be excluded. Based on these results, we deduce that the ligand shell of the CdSe QDs before pyridine treatment is composed only of oleic acid molecules.

This consideration was further confirmed by ^{1}H NMR measurements. The ^{1}H NMR spectrum of the CdSe nanocrystal sample coated with the original ligands from synthesis is shown in Fig. 6.1b and that of the recovered ligands in Fig.6.1c. The ^{1}H NMR spectrum of pure OA is represented in Fig. 6.1a. Two small peaks in the nanoparticles sample at 4.96 and 5.80 ppm belong to 1-octadecene (ODE), which show the difficulty to remove it completely. In the NMR spectrum of the intact CdSe QDs (Fig. 6.1b), the signals from the parts of oleic acid molecules in the direct neigh-

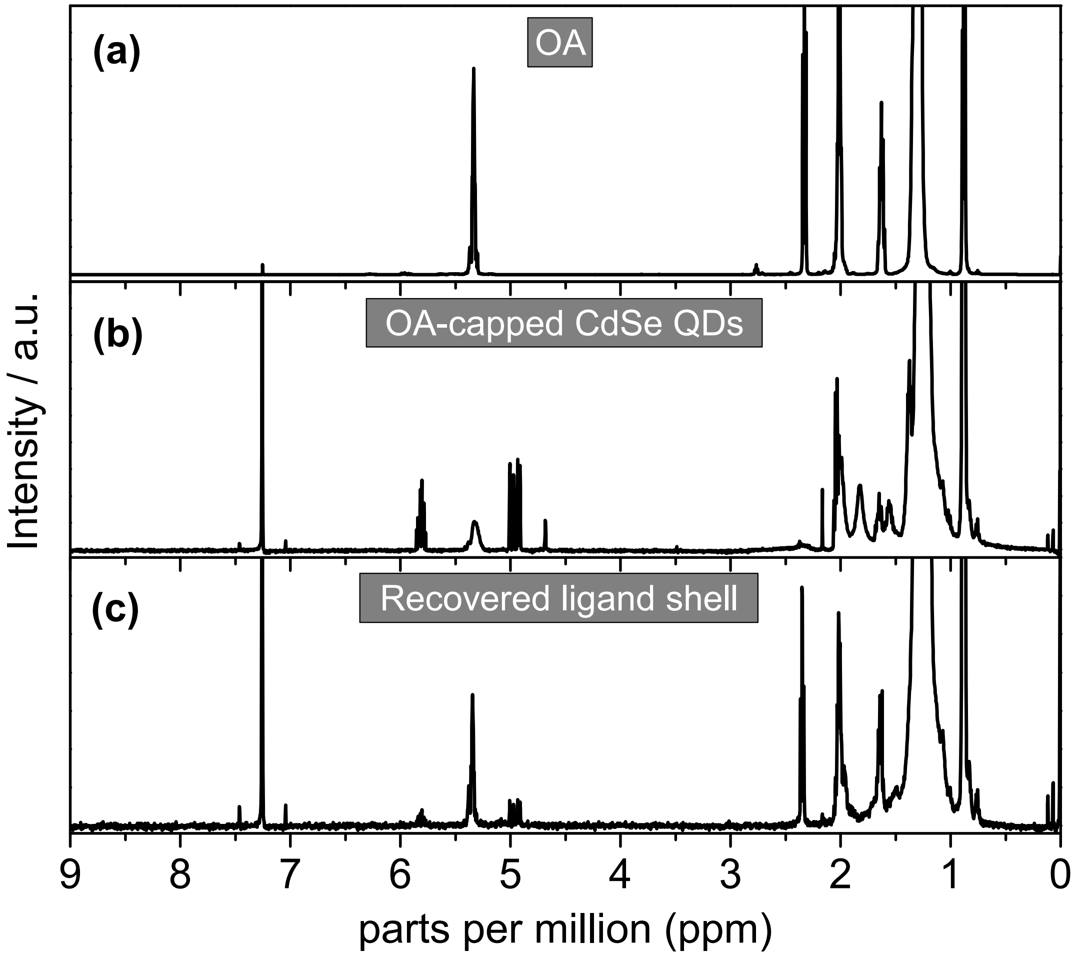

Figure 6.1: ^{1}H NMR spectra of (a) pure OA; (b) intact CdSeOA QDs; (c) recovered ligand shell of CdSeOA QDs.

borhood of the CdSe surface are broadened and shifted, and no signals from free OA can be observed. Because of the absence of free OA ligands in the intact particles, the measurements of the recovered ligand cap should precisely reveal the composition of the organic ligands bound to the surface.

Thus, in the ^{1}H NMR spectrum of the recovered ligand shell (Fig. 6.1c) one can clearly observe the presence of all typical OA peaks (Fig. 6.1a). The integrals of these signals, however, do not match those of the pure OA. The high intensity of the signals at 0.88 and 1.26 ppm can be assigned to hydrogen atoms bound to the aliphatic carbon chain, which indicates the presence of some additional organic material in the sample (the presence of additional organic material will be further confirmed by an XRD pattern). This could be polymerized ODE molecules, since as it had already been proven by mass spectrometry measurements (see Fig. 4.2 on page 44), ODE shows a strong tendency to form oligomers (composed of two, three, and four molecules) upon heating. These oligomers are difficult to remove from the samples through a standard cleaning procedure.

6.2.2 Investigation of the CdSe ligand shell after pyridine treatment

As it was previously written on page 96, the absorption spectra are one of the main characteristics of a successful ligand exchange. The main absorption features such as peak position and contour should be maintained in their original state confirming that no changes (such as oxidation, etching, or aggregation) of the CdSe QDs occurred. To avoid undesirable oxidation of the sample, all solvents should be degassed before usage, otherwise anhydrous solvents should be used. To prevent aggregation, the CdSe pellet at the vial's bottom after the precipitation/centrifugation should be redissolved in a new solvent as soon as possible. Fig. 6.2 represents the absorption spectra of CdSe QDs (with the mean diameter of 3.04 nm) before and after three cycles of the pyridine treatment. The band gap of bulk CdSe is reported to be 712-716 nm (1.74-1.73 eV)

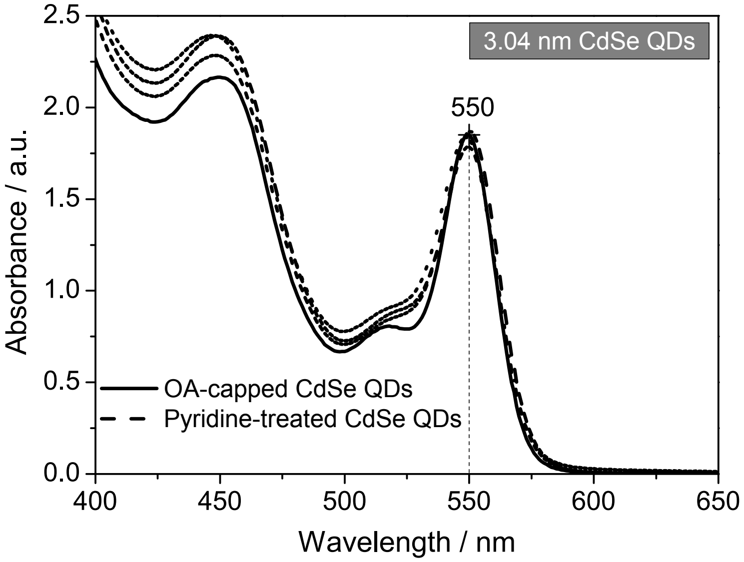

Figure 6.2: Absorption spectra of CdSeOA, CdSePy1, CdSePy2, and CdSePy3 QDs.

[159][160]. Thus, the present measurements show that there is a blue shift of more than 150 nm due to the pronounced size quantization effect. The absorption spectra have three well-defined absorption maxima indicating a high quality of the synthesized NCs. As the pyridine-treated CdSe QDs maintain the original optical spectra (in particular, the position and the width of the first maximum did not change), it means that the ligand exchange did not influence the size or size distribution of the NCs. Closer inspection only reveals the small visible change in the absorption spectra, viz. the position of the second absorption maximum is slightly shifted after the pyridine treatment. However, this could be an indication for different surface properties after a successful pyridine treatment.

Although the optical spectra of the CdSe QDs before and after the ligand exchange show almost no differences, TEM images of the corresponding samples demonstrate a tendency of nanoparticles to aggregate (Fig. 6.3). As-synthesized CdSe QDs can be found on a TEM grid well separated by their initial ligand shells, i.e. long-chained OA molecules (Fig. 6.3a). After the substitution of big OA molecules with small pyridine

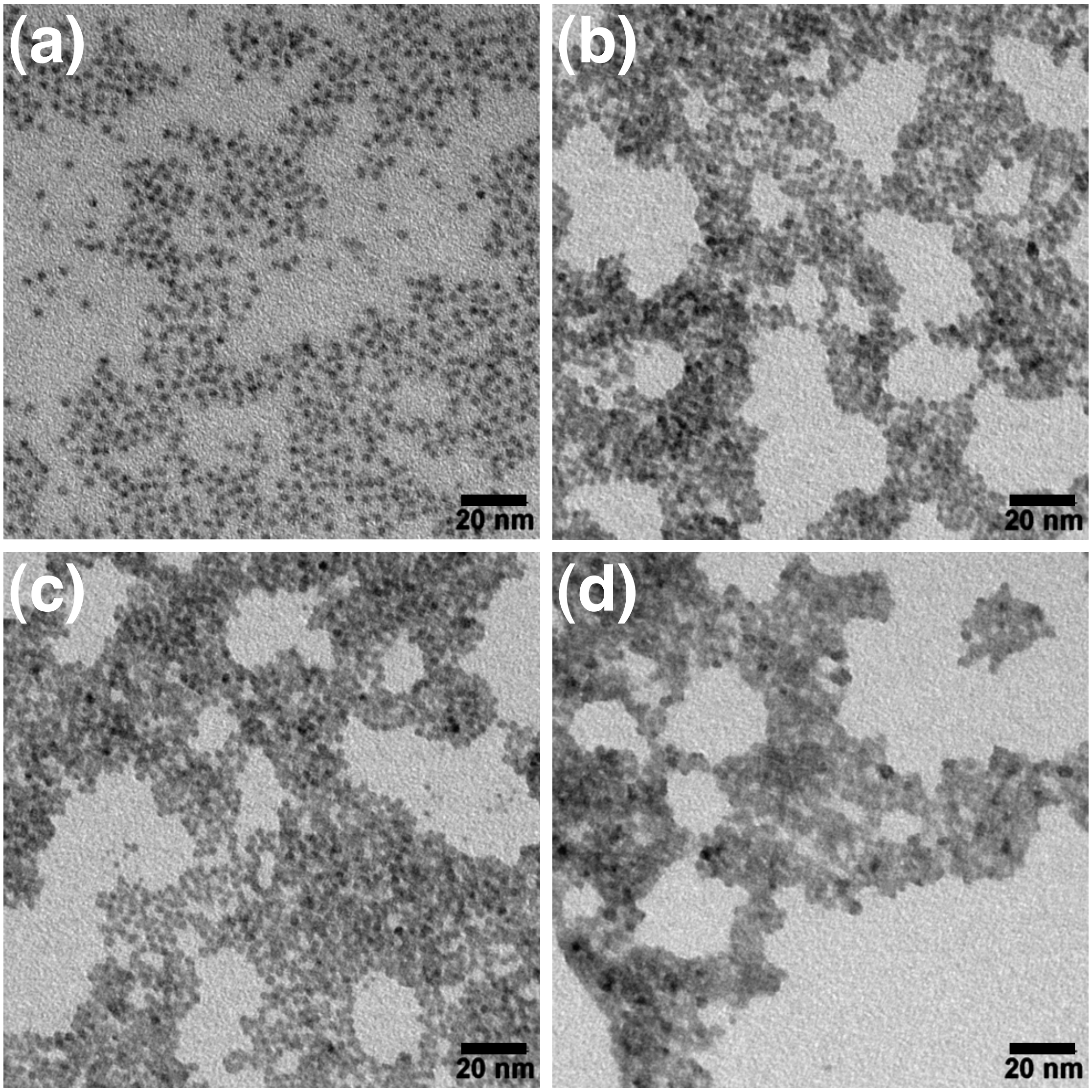

Figure 6.3: TEM images of (a) CdSeOA; (b) CdSePy1; (c) CdSePy2; (d) CdSePy3 QDs.

molecules, the size of the particles themselves does not change, but the distance between them decreases due to the thinner ligand shell. With the increase in number of subsequent runs of the pyridine treatment, this tendency to form aggregates on a TEM grid becomes more pronounced (Fig. 6.3b, c, d). After the third pyridine treatment, it is even difficult to distinguish separate nanoparticles in the TEM image (Fig. 6.3d). However, it should be pointed out that this aggregation caused by the thinner and weaker ligand shell seems to occur only during the drying process on the TEM grid, because the absorption spectra did not provide any evidence for aggregation in the colloidal solutions of the pyridine-treated QDs. The HRTEM images of the purified CdSe NCs in hexane and pyridine (Fig. 6.4) confirm their high crystallinity which is evident by the presence of clear lattice planes. Well-defined orientation of the lattice fringes is a prerequisite to recognize the stacking sequence, which is difficult to obtain from the pictures. That is why in our case, the crystal phase of the CdSe QDs can be more reliably determined by the powder X-ray diffraction (XRD) technique.

XRD analysis of the original (CdSeOA QDs) and pyridine-treated (CdSePy1 QDs) CdSe NCs revealed that both samples exhibit a zinc blende structure (Fig. 6.5). It should be noted that the CdSeOA QDs cannot be obtained in the form of a powder through a standard cleaning procedure. Even after a very thorough purification, the samples look like a viscous paste suggesting that there is still some excess of organics left. The presence of organic impurities is confirmed by the presence of an additional reflection in the XRD pattern in the case of the original CdSe QDs (Fig. 6.5a). As already discussed, this could be oligomers of ODE and remaining OA molecules in the ligand shell. The pyridine-treated NCs, on the contrary, represent a powder after evaporation of the solvent, and the XRD pattern has no additional peaks besides the Bragg's reflections belonging to CdSe particles (Fig. 6.5b). This shows that the ligand exchange with small pyridine molecules is an effective way to get rid of big OA molecules and organic impurities of ODE. The effectiveness of this method and the composition of the ligand shell were further studied by NMR spectroscopy and TGA analysis.

The ^{1}H NMR spectra of the intact particles and the recovered ligand shell of the CdSe QDs after one cycle of the pyridine treatment (CdSePy1 QDs) are represented in Fig. 6.6b, c, respectively. For comparison, the ^{1}H NMR spectrum of pure pyridine is shown in Fig. 6.6a. In the NMR spectrum of the intact particles (Fig. 6.6b), three peaks

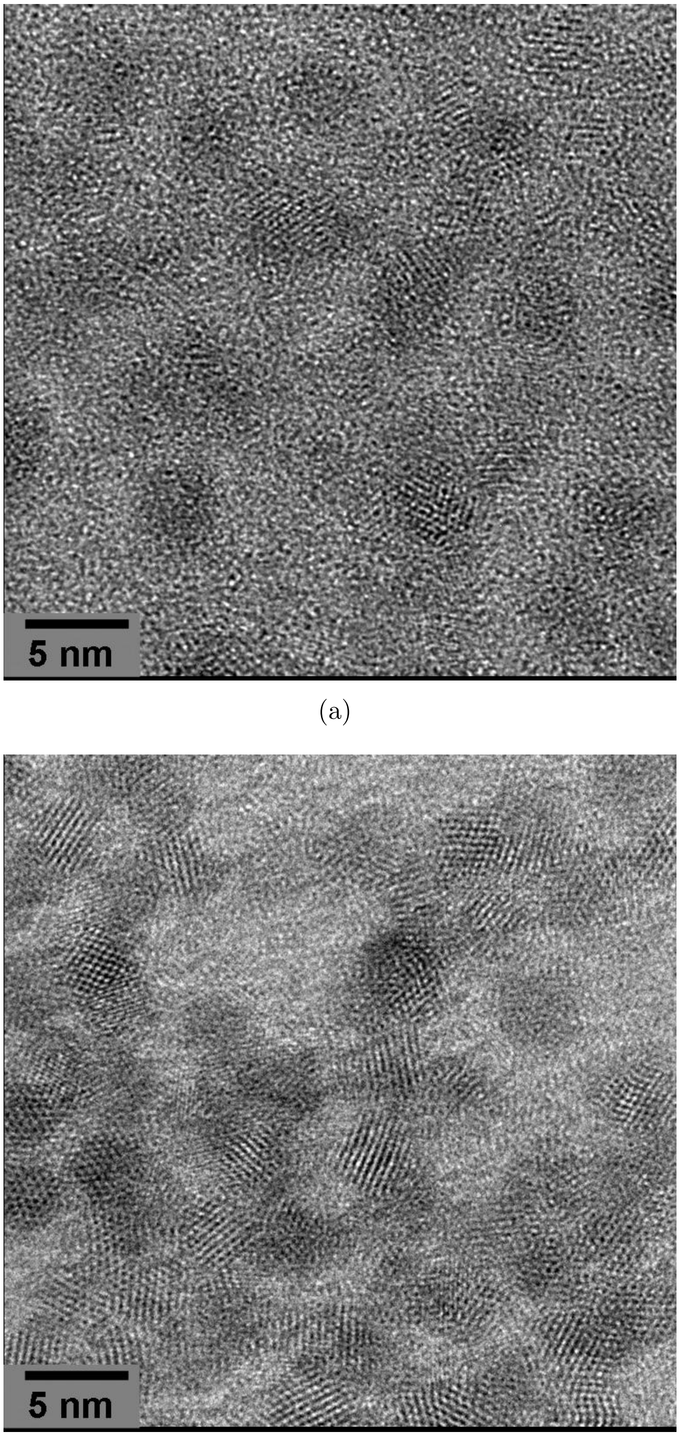

(a)

(b)

Figure 6.4: HRTEM images of CdSeOA and CdSePy1 QDs indicate high crystallinity of NCs before and after the ligand exchange: (a) CdSeOA QDs; (b) CdSePy1 QDs.

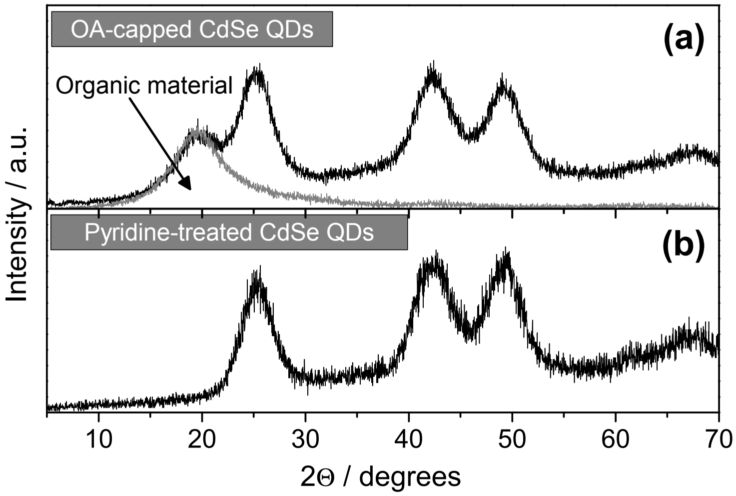

Figure 6.5: XRD patterns of (a) CdSeOA QDs; (b) CdSePy1 QDs show the presence of zinc blende structure for both of the samples.

corresponding to pyridine at 7.29, 7.68, and 8.62 ppm can be observed, although the first peak is overlapped by the signal of $CDCl_3$. These peaks are shifted to bigger ppm values compared to pure pyridine (Fig. 6.6a). This fact makes it possible to conclude that pyridine is bound to the NCs surface. In addition, no peaks that could be specifically assigned to OA molecules can be found in the spectrum of pyridine-treated CdSe QDs. The ^1H NMR spectrum of the recovered ligand shell reveals, on the contrary, the presence of all typical OA signals (Fig. 6.6c). This can be explained by the fact that in the intact particles OA molecules are bound to the CdSe surface, and their peaks are broadened, which is why they cannot be observed. Interestingly, pyridine signals are missing in the spectrum of the recovered ligand shell. However, this can be due to better miscibility of pyridine with the DCl-D_2O phase than with $CDCl_3$ used for the NMR measurements. Thus, taking the measurements of both the intact QDs and the recovered ligand shell into account, it is safe to conclude that the ligand shell after the pyridine treatment is composed of both OA and pyridine molecules. The NMR analysis clearly reveals that both types of molecules are bound to the surface of the NCs.

To prove the NMR results, a TGA analysis both of the original (CdSeOA QDs)

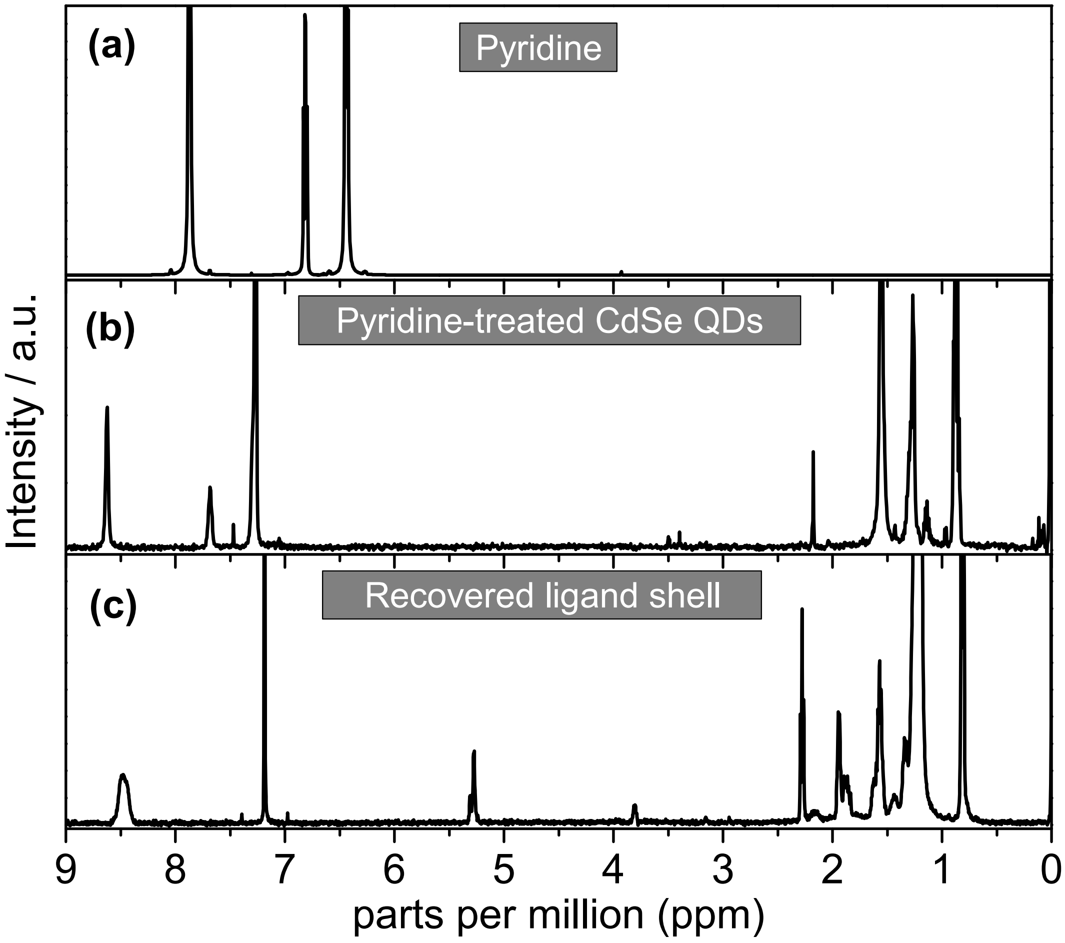

Figure 6.6: ^{1}H NMR spectra of (a) pure pyridine; (b) intact CdSePy1 QDs; (c) recovered ligand shell of CdSePy1 QDs.

and pyridine-treated CdSe QDs after every run of the ligand exchange (CdSePy1, CdSePy2, CdSePy3 QDs) was carried out. The TGA curve of the CdSeOA sample is depicted in Fig. 6.7a. As it can be seen, there is only one-stage decomposition pattern of the weight loss for OA-coated NCs. The weight loss starts at 160 ℃ and continues until 470 ℃ with the derivative of this curve having a maximum at ca. 435 ℃ (Fig. 6.7b). Such high desorption temperature indicates that the particles are covered by strongly binding ligands. Following the NMR results, the ligand shell of the CdSe QDs is composed of OA molecules which are known to bind strongly to the CdSe surface and to decompose from the surface at high temperatures in TGA

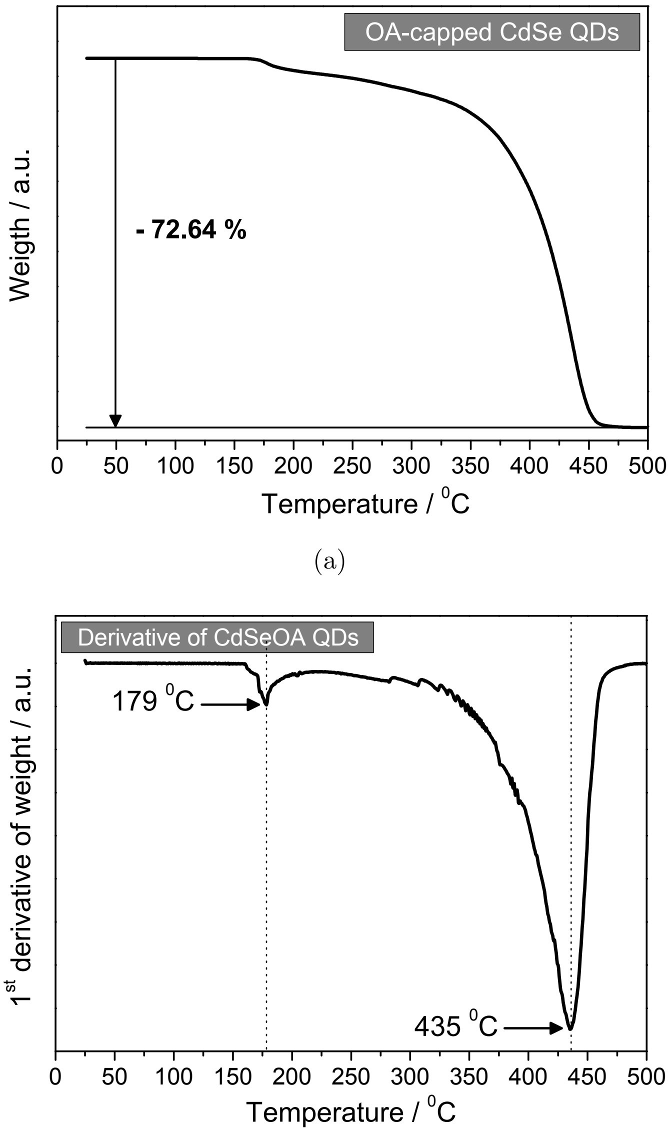

(a)

(b)

Figure 6.7: Results of the TGA analysis of CdSeOA QDs: (a) TGA curve showing weight loss; (b) First derivative of the TGA curve.

experiments [161]. A total weight loss of 72.64 % was observed when the analysis was done between room temperature and 500 ℃ at a rate of 2.5 ℃/min under a nitrogen atmosphere. This result is supportive of the XRD pattern and NMR spectra indicating the presence of big quantities of the organic material in the nanocrystal sample. The availability of ODE oligomers in the viscous paste of the sample allows us to assume that they, together with OA ligands, contribute to the total weight loss.

It should be noted that a small mass loss (which can be seen from the 1st derivative) is also observed for this sample at 179 °C, possibly due to the presence of other weakly bound species.

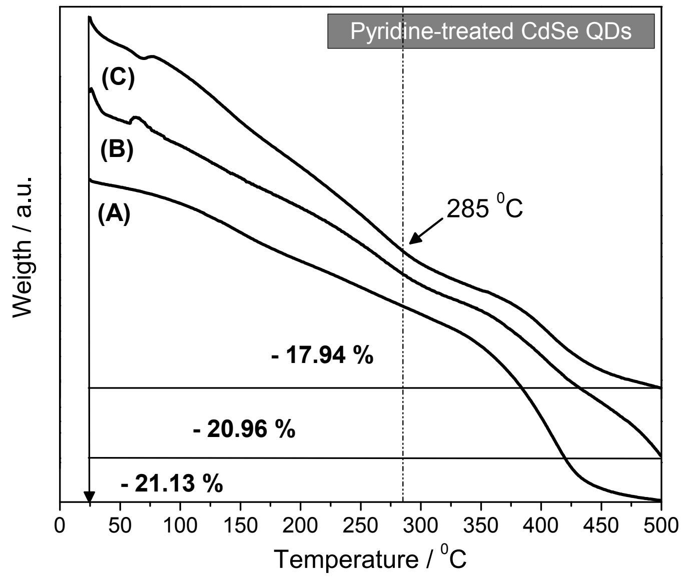

(a)

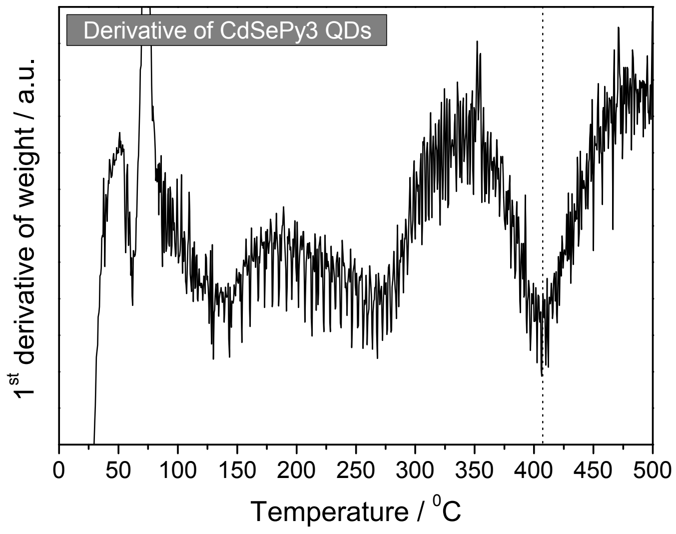

(b)

Figure 6.8: Results of the TGA analysis of pyridine-treated CdSe QDs: (a) TGA curve showing weight loss for (A) CdSePy1 QDs; (B) CdSePy2 QDs; (C) CdSePy3 QDs; (b) First derivative of the TGA curve of CdSePy3 QDs.

The TGA curves of the pyridine-treated CdSe QDs (Fig. 6.8a) show already two-stage decomposition patterns with the breaking point at ca. 285 ℃. The total weight losses for NCs after the first, second, and third cycle of the pyridine treatment are 21.13, 20.96, and 17.94 %, respectively (Fig. 6.8a). This reduction of the weight loss from approx. 73 to 20 % after the pyridine treatment clearly confirms that the ligand exchange of OA-capped CdSe QDs with pyridine substantially removes the organic impurities from the nanocrystal sample. However, it can be seen that not all of the original OA ligands can be replaced by pyridine after one-fold and even after three successive steps of the pyridine treatment. This is evidenced in the TGA curve of the CdSePy3 sample by a second decomposition step with a maximum at 410 ℃ (Fig. 6.8b), also observed almost at the same position in the case of the OA-capped QDs. The similar results were reported for the pyridine treatment of initially TOPO-coated NCs, where even after seven cycles of the ligand exchange with pyridine, some of the original ligands were present in the sample (approx. 10-15 %) [147].

Assuming that weight loss below and above 285 ℃ is due to weakly bound pyridine molecules and strongly bound OA ligands, respectively, the fraction of surface sites capped by pyridine (γ_{Py}) and OA (γ_{OA}) molecules on the surface of CdSe QDs was estimated after each pyridine treatment using a method developed by Foos et al. [162].

The authors define the mass fraction of organic material lost in the TGA experiment as (X_{org}):

$$X_{org} = \frac{M_{org(total)}}{M_{org(total)} + M_{core}} \tag{6.1}$$

where $M_{org(total)}$ is the total mass of organic ligands and M_{core} is the mass of the CdSe core. Under assumption that the surface coordinating species only bind at Cd sites, $M_{org(total)}$ can be further defined as:

$$M_{org(total)} = S \cdot M_{org} \cdot \gamma \tag{6.2}$$

where S is the number of surface Cd atoms, M_{org} is the mass of the organic ligands (g/molecule), and γ is the packing factor or fraction of surface Cd atoms which are bound to coordinating species. Substitution of this equation leads to:

$$X_{org} = \frac{S \cdot M_{org} \cdot \gamma}{S \cdot M_{org} \cdot \gamma + M_{core}} \tag{6.3}$$

Solving of γ results in:

$$\gamma = \frac{X_{org} \cdot M_{core}}{S \cdot M_{org} - X_{org} \cdot S \cdot M_{org}} \tag{6.4}$$

The mass of the core can be determined as follows:

$$M_{core} = \frac{V_{core}}{V} \cdot N \cdot MW_{CdSe} \cdot \frac{1}{N_A} = \frac{4/3\pi r^3 \cdot N \cdot MW_{CdSe}}{V \cdot N_A} \tag{6.5}$$

Here, V_{core} is the calculated volume of the CdSe core, V is the volume of a CdSe unit cell (with radius of 0.608 nm), N is the number of CdSe units per unit cell (N = 4), MW_{CdSe} is the molecular weight of CdSe, and N_A is Avogadro's number.

In order to calculate S, the number of Cd surface sites, Foos et al. used the model presented by Kuno et al. [158]. Using this method, they obtained the following equation:

$$S = (CdSe)_r - (CdSe)_{r-d} \tag{6.6}$$

where $(CdSe)_r$ is the number of CdSe units in a sphere of radius r and $(CdSe)_{r-d}$ is the number of CdSe units in a sphere of radius r-d, with d defined as the Cd-Se bond length of 0.262 nm.

Therefore,

$$S = \left(\frac{4/3\pi r^3}{V}\right) \cdot N - \left(\frac{4/3\pi (r-d)^3}{V}\right) \cdot N = \frac{\{4/3\pi r^3 - (4/3\pi (r-d)^3)\}\, N}{V} \qquad (6.7)$$

Again, assuming that the ligand molecules are bound only to Cd (and not to Se) atoms, we estimated the number of surface Cd atoms (S) for CdSe QDs with a diameter of 3.33 nm. The size of nanoparticles was calculated as usual from the absorption spectrum using Eq. 2.1 on page 10 (the absorption spectrum is not shown here). Taking the magnitude X_{org} (total weight loss) from the TGA measurements and solving the aforesaid expression for γ (Eq. 6.4), we calculated the packing factor γ both for pyridine and oleic acid ligands: γ_{Py} and γ_{OA}. As already mentioned, it was considered that pyridine ligands decompose below 285 °C and oleic acid above this temperature. The following results were obtained: $\gamma_{Py} = 0.54, 0.73, 0.80$ and $\gamma_{OA} = 0.26, 0.20, 0.12$ for the samples CdSePy1, CdSePy2, and CdSePy3, respectively. The exact calculations are summarized in Table 6.1.

Table 6.1: Summary of the results calculated from the TGA and UV-Vis absorption spectra (using Eq. 2.1 and Eq. 6.1-6.7).

Ligand	Pyridine			Oleic acid		
Sample	CdSePy1	CdSePy2	CdSePy3	CdSePy1	CdSePy2	CdSePy3
Wavelength/nm	563					
Diameter/nm	3.33					
S	138					
M_{core}/g	1.12E-19					
M_{org}/g	1.31E-22			4.69E-22		
X_{org}	0.080	0.105	0.114	0.131	0.104	0.065
γ	0.538	0.729	0.799	0.262	0.202	0.120

Interestingly, the originally OA-coated NCs influenced by a high temperature during the TGA measurements (ca. 500 °C) show a different type of a crystal structure than the samples after the synthesis, i.e. zinc blende is transformed to a wurtzite structure (Fig. 6.9a), whereas no changes are observed for the pyridine-treated NCs (Fig.

6.9b). It is known that according to thermodynamic laws, zinc blende and wurtzite forms are the most stable at lower and high temperatures, respectively. That is why the wurtzite structure of CdSe nanocrystals is more likely to be obtained at higher temperatures. Although during the synthesis the injection is fulfilled at 300 ℃, the obtained NCs exhibit a zinc blende structure, which changes to wurtzite at higher temperatures during the TGA measurements. This is typical, however, only for OA-coated NCs. A similar cubic to hexagonal phase transition was documented for CdSe NCs with thermal annealing at 300-400 ℃ [99]. The corresponding to each maximum crystallographic reflections are depicted in Fig. 6.9.

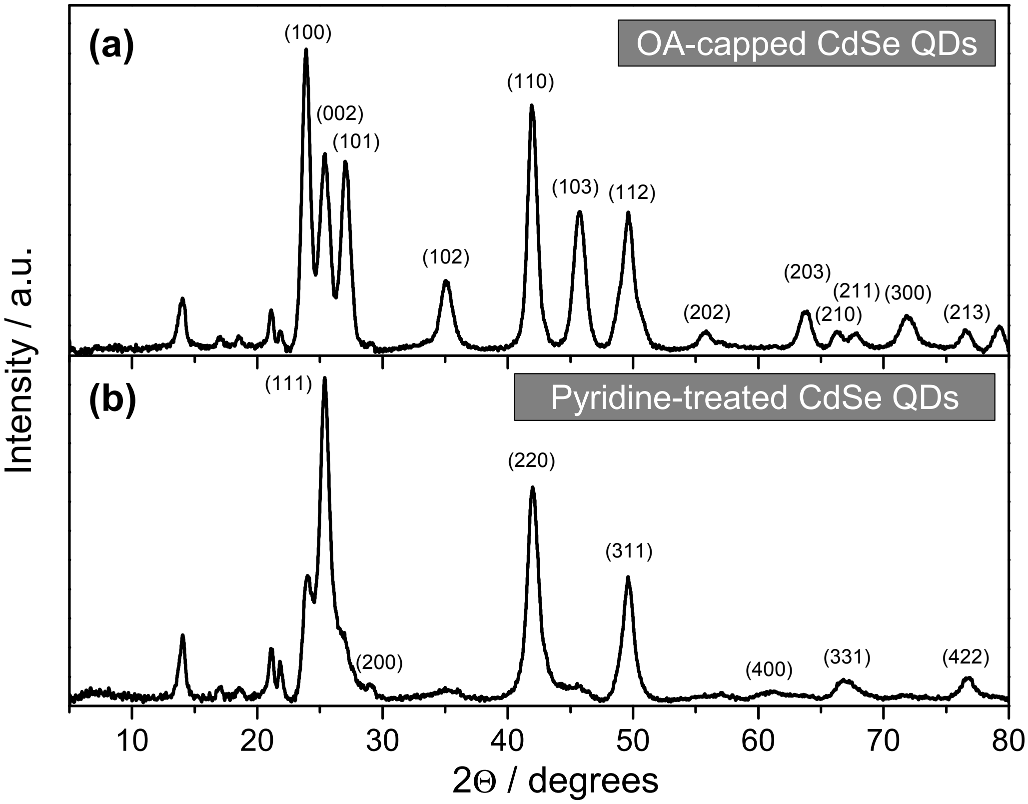

Figure 6.9: XRD patterns of (a) CdSeOA QDs; (b) CdSePy1 QDs after the TGA measurements show the change in the crystal structure of OA-capped CdSe QDs from zinc blende to wurtzite.

So, from the TGA measurements it is evident that after every pyridine treatment more and more OA-molecules are substituted with pyridine molecules. The overall surface coverage increases from 80 % to 93 % after the second pyridine treatment and almost does not change after the third pyridine treatment. This shows that the change of the γ values is really due to an exchange of strong OA ligands by weak pyridine ligands and not a result of a binding of additional pyridine molecules to the surface. After third pyridine treatment, 12 % of the original OA ligands are left in the sample, which is similar to the measurements made for the case of initial TOPO-ligands, when after three cycles of the pyridine treatment, 11 % of TOPO-ligands remained in the ligand shell [154]. This implies that the effectiveness of the ligand exchange with pyridine is almost the same both for OA and TOPO surfactants. Thus, the TGA results confirm the observation made by TEM (increasing aggregation tendency) that the stabilization of the NCs gets weaker with every step of the pyridine treatment. Moreover, the TGA results corroborate the conclusions made from the NMR spectra that after one-fold pyridine treatment (CdSePy1 QDs), the ligand shell is composed of both oleic acid and pyridine molecules.

6.3 Conclusions

To conclude, the investigation of the initial ligand shell of CdSe QDs was fulfilled and it was demonstrated that as-synthesized NCs are only oleic acid capped, despite the fact that a TOPSe solution was used as a Se precursor. Then these NCs were subjected to three repeated steps of pyridine treatment to achieve the more efficient surface modification. The successful ligand exchange was proved by means of UV-Vis absorption and NMR spectroscopy. The TGA analysis allowed us to investigate the surface coverage of CdSe QDs with oleic acid and pyridine surfactants. The TEM and XRD measurements were carried out for structural characterization of the samples.

Chapter 7

Preparation of P3HT/CdSe QD hybrid solar cells

In this chapter, the application of the CdSe QDs for the preparation of polymer/CdSe hybrid solar cells is investigated. The hybrid CdSe/P3HT solar cells were fabricated using the pyridine capped CdSe QDs, and I-V characteristics of these solar cells were collected to characterize the sequential steps of the pyridine treatment. Although repeated pyridine treatment was found to have a beneficial effect in the sense that it led to more complete ligand exchange, which in turn enabled more efficient charge transfer, the main characteristic parameters of the solar cells were found to deteriorate. Correlations of this behavior with the morphology of the hybrid blends were analyzed. Furthermore, two cross-linking compounds (viz. 1,7-diaminoheptane and 3,3',5,5'-tetramethylbenzidine) were attempted to improve the charge transport between the pyridine-treated CdSe QDs. The solar cells fabricated with every cross-linker and different cross-linking procedures were analyzed.

7.1 Motivation and review of the literature

The growing world energy demand and limited fossil fuel resources promote the search for renewable energy sources. In particular, in recent years, the conversion of globally available and inexhaustible solar light into electricity has attracted much attention. The processes of light harvesting and generation of electricity are described in detail in the literature [163][164]. Different photovoltaic (PV) solar cells have been developed, which are often categorized into first, second, and third generation by their materials:

- First generation solar cells are based on crystalline silicon (single junction devices) and currently dominate the solar panel market due to their high efficiency. However, their production is connected with high costs, a problem that second generation cells hope to remedy.
- Second generation cells, also called thin-film solar cells (including amorphous and micromorphous silicon, cadmium telluride (CdTe), and copper indium gallium sulfide or selenide (CIGS/CIGSe)), are significantly cheaper than the first generation cells, but have lower efficiencies. Another great advantage of second generation solar cells is their flexibility, for instance, solar shingles and solar panels can be rolled out onto a roof or other surfaces.
- Third generation technologies aim to enhance a poor electrical performance of the second generation cells together with maintenance of low manufacturing costs. Such technologies include multijunction photovoltaic cells, tandem cells, silicon nano-structures, thermoelectric cells, etc. However, until now they have just been a research target and do not yet really exist in the production.

At present, there is concurrent research on all three photovoltaic cells generations. In this thesis, we focus on the study of second generation solar cells and, in particular, on the blends of conjugated polymer and inorganic nanocrystals that have several advantages such as high electron mobility, low cost, easy processing, the potential for large-areas devices, the possibility to be realized on flexible substrate, and/or improved spectral coverage [165][166].

Nowadays, the organic solar cells comprised of conjugated polymers as electron donors and fullerene derivatives as electron acceptors achieve power conversion efficiencies (PCE) up to 6.5 % [167], which is higher than that of conjugated polymer/NC solar cells (PCE up to 2,8 %) [168]. Nevertheless, introducing inorganic nanoparticles, such as CdSe, in photovoltaic devices has a lot of potential and is worth being studied. The main advantage of using organic/inorganic hybrid solar cells versus organic devices lies in the high intrinsic carrier mobilities that exist in inorganic semiconductors. Moreover, in inorganic nanoparticles, the electronic properties can be controlled, tuned and in some cases completely changed by nanoscale confinement. In other words, varying the radius of the NCs, the quantum size effect can be used to control their band gap and the fabricated devices can be made thinner due to enhancement of the absorption coefficient of the NCs as compared to the bulk material. Additionally, the absorption of CdSe nanoparticles in the visible region is much better in comparison to [6,6]-phenyl C61-butyric acid methyl ester (PCBM), the most commonly used organic electron acceptor material.

Often, CdSe nanocrystals with tunable band gaps and high intrinsic charge carrier mobilities are combined with conjugated polymers, such as e.g. poly(2-methoxy-5-(2-ethylhexoxy)-p-phenylenevinylene) (MEH-PPV) or poly(3-hexylthiophene) (P3HT), to form bulk-heterojunction (BHJ) hybrid solar cells [5][149][168][169][170]. In these systems, charge transfer is favored between high electron affinity inorganic semiconductors (acting as electron acceptors) and relatively low ionization potential organic polymers (acting as electron donors).

Several morphologies of CdSe NCs have been applied for the fabrication of bulk-heterojunction hybrid solar cells, among them are quantum dots (QDs) [171][172], nanorods [173][166][169], tetrapods [174][168], and hyperbranched [170] CdSe NCs.

State-of-the-art organic solar cells made of CdSe QDs and P3HT show lower PCE in comparison to other nanoparticle shapes since elongated structures are supposed to be favorable for efficient electron transport. However, this difference is being reduced and the best PCE of 2.0 % for CdSe QDs/P3HT solar cells has been recently demonstrated by Zhou et al. [175]. In comparison, the best values of PCE of CdSe nanorods and CdSe tetrapods are known to be 2.6 % [169] and 2.8 % [168], respectively. Furthermore, the availability of numerous kinds of CdSe QDs syntheses (mostly wet chemical methods) allows to vary the nanoparticles surfactants that influence the charge transfer and solubility of NCs.

Usually, long-chained ligands used during the synthesis of CdSe QDs to prevent their aggregation impede the charge transfer between NCs and polymer, and for this reason the surface modification is often applied [5][176][38][172][177]. Various surface modification procedures have been reported to enhance the electrical response of photovoltaic devices [178][179], however, the most common one is the pyridine treatment. Relatively small pyridine molecules with an aromatic-ring structure enhance charge transfer and can be removed through thermal annealing easier than long-chained alkyl ligands (e.g. TOPO or OA).

Remarkably, the pyridine treatment was already applied in the first studies concerning inorganic/organic solar cells. Attempts to fabricate the solar cells from pyridine-treated CdSe spherical nanoparticles and conjugated polymer MEH-PPV were made by the group of Alivisatos in 1996 [149]. However, the obtained PCE was very low (ca. 0.1 %). In 2006, Han et al. managed to produce nc-CdSe/MEH-PPV solar cells with a higher PCE, i.e. 0.65 % before and 0.85 % after annealing, and CdSe/P3HT solar cells with PCE of 1.08 % (with 80 wt. % of nc-CdSe) under simulated AM1.5 global condition [177]. Thus, they showed the role of annealing and necessary weight percentage of CdSe NCs for improvement of the photovoltaic device performance.

In 2008, Olson et al. investigated the impact of surface modified CdSe QDs on the CdSe/P3HT solar cells: original TOPO ligands were exchanged with different molecules, viz. pyridine, butylamine, tributylamine, oleic acid, and stearic acid [172]. They reported the best efficiency with butylamine ligands (up to 1.77 %).

In 2010, Zhou et al. reported the power conversion efficiency of about 2 % for non-ligand exchanged CdSe QDs/P3HT hybrid solar cells [175]. For the solar cell fabrication, they applied an acid-assisted washing procedure to hexadecylamine (HDA) capped spherical CdSe QDs which resulted in substantial reduction of the ligand shell thickness. Thus, either ligand exchange or other procedures reducing the thickness of the initial ligand shell were proved to be necessary for the improvement of charge transfer in polymer/nanoparticle solar cells.

In this thesis, we report on the impact of the ligand exchanged CdSe QDs combined with P3HT for the solar cells fabrication. The as-synthesized CdSe NCs were capped with long-chained OA ligands (ca. 2 nm [150]) which are known to impede efficient charge transport in films. That is why in order to improve electrical properties of the CdSe/P3HT films, surface modification of CdSe QDs with shorter pyridine molecules (ca. 0.6 nm [151]) was applied. From the schematic energy level diagram for CdSe nanocrystals and P3HT (Fig. 7.1a) it can be seen that CdSe is used as the electron transport material and P3HT is an effective hole transport material in its regioregular form. In these systems, current is observed in the external circuit because the electric field drives the holes generated or formed in the P3HT layer toward the PEDOT:PSS/ITO electrode and electrons in CdSe NPs toward the Al electrode. The mechanical properties of highconductive P3HT allow for solution-casting of uniform thin films at room temperature. Additionally, due to complementary absorption spectra of CdSe and P3HT in the visible range, these QD/polymer blend devices have a very broad photocurrent spectrum extending from 300 to 650 nm (Fig. 7.1b).

Furthermore, to enhance the charge transfer between neighbored CdSe nanoparticles, a cross-linking technique was applied to the pyridine-treated CdSe QDs. For this

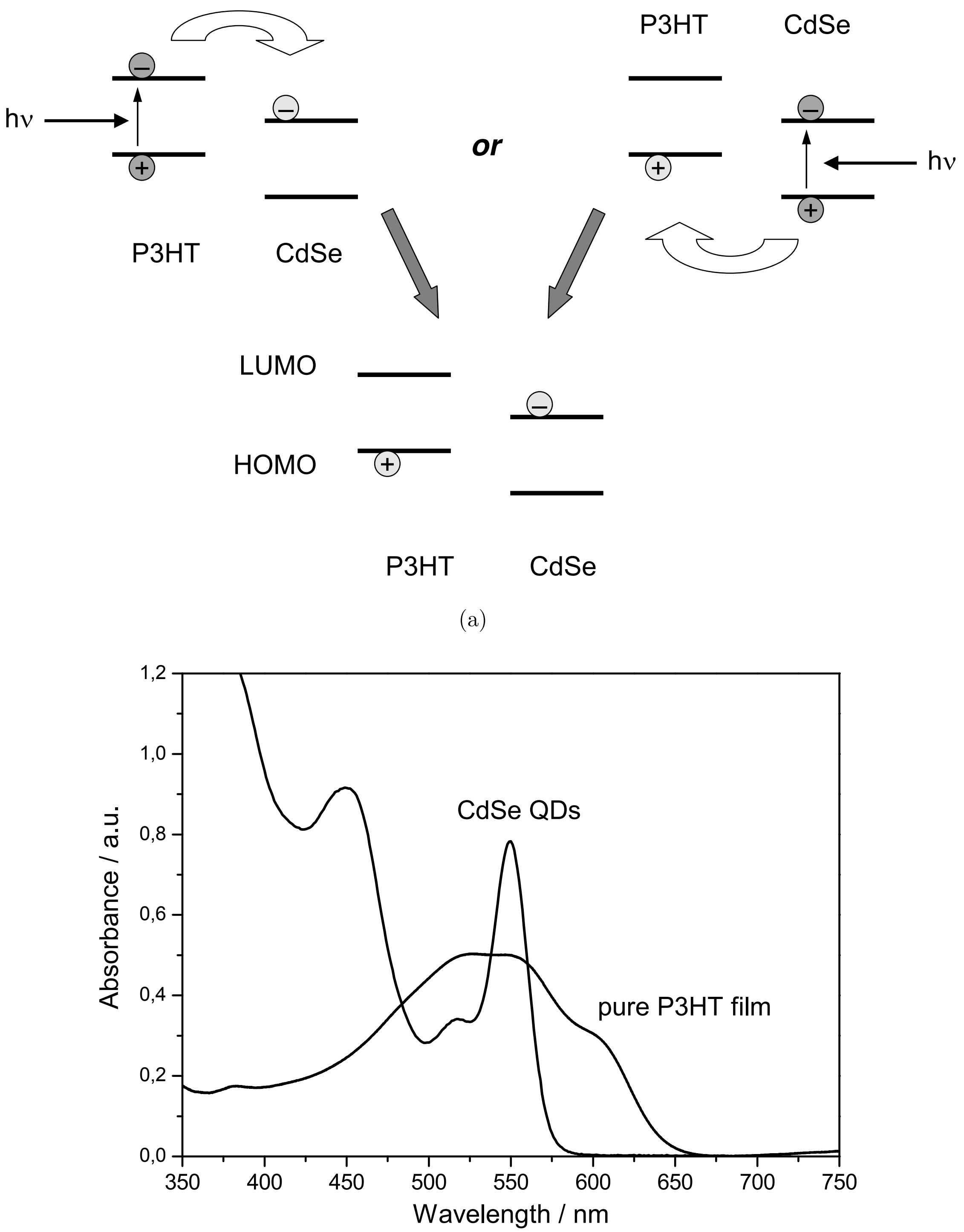

(a)

(b)

Figure 7.1: The hybrid system of P3HT and CdSe QDs: (a) Schematic representation of the charge transfer between CdSe NCs and P3HT; (b) Absorption spectra of CdSe QDs in a solution and pure film of P3HT.

purpose, two organic molecules possessing two spatially separated amino groups were chosen.

7.2 Results and discussion

7.2.1 Influence of multiple pyridine treatments on the performance of solar cells

The composition of the ligand shell of CdSe NCs is known to have a big effect on the performance of solar cells [172]. As it was discussed in Chapter 6, the one-fold pyridine treatment of originally OA-capped CdSe QDs does not lead to complete substitution of the old ligands with new ones. However, repeated ligand exchange increases the percentage of surface atoms bound to pyridine molecules. To investigate the impact of the ligand shell composition of CdSe QDs on the efficiency of photovoltaic devices, CdSe NCs after every cycle of three pyridine treatments (CdSePy1, CdSePy2, and CdSePy3 QDs) were incorporated into hybrid bulk heterojunction (BHJ) P3HT/CdSe solar cells.

The current density-voltage characteristics of these solar cells in the dark and under illumination and the fourth quadrant of the J-V curves are depicted in Fig. 7.2a and b, respectively. It can be seen that all solar cells behave like a rectifying diode and exhibit a photoresponse. The main characteristics of the solar cells, i.e. the open circuit voltage (V_{oc}), the short circuit current density (J_{sc}), the fill factor (FF), and the power conversion efficiency (η or PCE), were determined for every sample (Table 7.1). The theoretical explanations and equations used for this purpose are summarized in Appendix B. From Fig. 7.2 and Table 7.1 it is evident that the solar cells based on the CdSePy1 QDs showed the best efficiency. The absolute magnitude of the efficiency (0.28 %) is not the highest among those reported for the blends of spherical CdSe NCs and P3HT (reaching 1 % [177][163]) since more effort should be made to

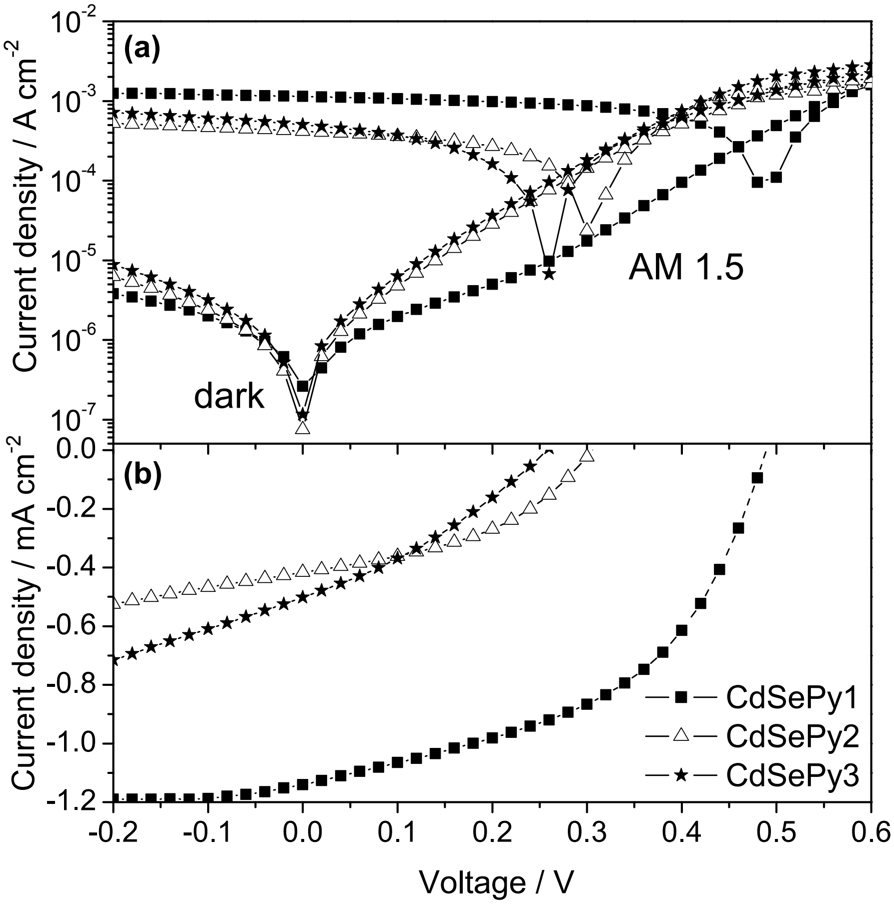

Figure 7.2: J-V characteristics of the hybrid solar cells in the dark and under illumination with simulated AM 1.5G radiation for cells with CdSePy1, CdSePy2, and CdSePy3 QDs: (a) J-V curves in the dark and under illumination in semi-logarithmic representation; (b) fourth quadrant in linear representation for the J-V curves under illumination. The fabrication of the solar cells and measurements were done by Dr. N. Radychev.

optimize the preparation parameters such as mixing ratio, annealing time and temperature, film thickness, etc. of our laboratory solar cells. However, the obtained efficiencies in this series of experiments are still a reasonable starting point and allow us to compare the samples after different steps of the ligand exchange. Astonishingly, the repeated pyridine treatment of CdSe QDs strongly decreased the main characteristic parameters of the solar cells. Thus, for example, for samples based on CdSePy1 and CdSePy2 NCs, the short circuit current density (J_{sc}) and the open circuit voltage (V_{oc}) dropped from 1.14 to 0.42 mA/cm^2 and from 0.49 to 0.31 V, respectively. This

Table 7.1: Characteristic parameters of the solar cells with CdSePy1, CdSePy2, and CdSePy3 QDs.

Treatment	FF	$J_{sc}, mA \cdot cm^{-2}$	V_{oc}, V	$\eta, \%$
1	0.49	1.14	0.49	0.27
2	0.44	0.42	0.31	0.06
3	0.34	0.50	0.26	0.04

resulted in the overall five-fold reduction of the power conversion efficiency (from 0.27 to 0.06 %, Table 7.1). As it was already mentioned in Chapter 6, the ligand exchange of long-chained fatty acids with short pyridine molecules enhances or even permits the electron and hole transfer between NCs and organic semiconductors. That is why the more pyridine molecules are present in the ligand shell (instead of e.g. OA molecules), the better the charge transfer between the polymer and NCs as well as neighbored QDs should be. Moreover, the annealing of the films at a temperature of 140 ℃ leads to partial evaporation of the weak pyridine ligands[1], which in turn improves the efficiency of the solar cells. Nevertheless, even if the fraction of the NC surface covered with pyridine increased after each cycle of the pyridine treatment (see Chapter 6), this resulted in worse quality of the solar cells.

Such behavior can be explained in terms of the morphology of the hybrid blends. Although the UV-Vis spectra showed that the size distribution of the colloidal CdSe QDs themselves remained unaffected by the multiple pyridine treatments (see Fig. 6.2 on page 103), the thickness of the ligand cap decreased substantially after the ligand exchange. Pyridine is not only shorter but also a weaker capping agent in comparison to OA, and a slight coagulation of CdSe QDs can occur much easier after the ligand exchange. This assumption is clearly evident by TEM images (see Fig. 6.3 on page 104), which demonstrate increasing tendency of the CdSe QDs to agglomerate in dry films after each step of the pyridine treatment. Such agglomeration phenom-

---

[1] The boiling point of free pyridine is 115.2 ℃.

ena have a strong effect on the morphology of the active layer. Presumably, the spin coating leads to large clusters of aggregated CdSe NPs that are not well-dispersed in the P3HT host matrix. The aggregation of the CdSe NCs in the P3HT matrix leads to the formation of an inhomogeneous active layer with the phase separation increasing after each cycle of the pyridine treatment. The strong phase inhomogeneity is then likely to impede the efficient charge separation due to the small exciton diffusion length in the polymer phase. Furthermore, electron spin resonance (ESR) measurements carried out by F. Witt (not shown here) revealed that after multiple pyridine treatments, the amount of defect states in the NC surface increased [180]. The observation of a higher trap density by ESR provides an additional reason for the reduced device performance.

7.2.2 Influence of cross-linkers on the performance of solar cells

It has been reported that the cross-linking leads to the enhanced chemical and presumably mechanical robustness of the films, making them very resistant to dissolution in many solvents [181]. Moreover, treatment of photovoltaic films with different cross-linking molecules results in enhanced conductivity and extremely improves the electrochromic kinetics of the films [182][183]. In particular, Yu et al. reported that conductivity of thin films of n-type CdSe NCs, measured between two gold electrodes, increased by many orders of magnitude as the TOP/TOPO-capped CdSe nanoparticles were treated with 1,7-diaminoheptane [182]. In our work, we tried two bidentate linkers such as 1,7-diaminoheptane (motivated by reference [182]) and 3,3',5,5'-tetramethylbenzidine, whose chemical structures are represented in Fig. 7.3. The amino-end groups have a strong affinity to Cd atoms and should cross-link the adjacent CdSe QDs at bare sites via a Cd-N bond (including the sites where pyridine ligands were initially bound, but evaporated after the annealing). Before the cross-

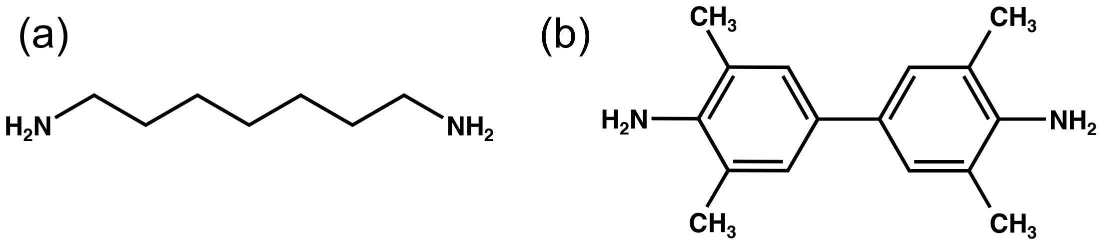

Figure 7.3: Chemical structures of the used cross-linkers: (a) 1,7-diaminoheptane; (b) 3,3',5,5'-tetramethylbenzidine.

linking procedure, the CdSe nanoparticles are likely to be bound by means of van der Waals forces between the ligands and cores of neighbored CdSe QDs. After the cross-linking, the particles become strongly bound to each other via the diamines (or dithiols) that act as bridging molecules: one functional group bonds to one CdSe QD and another to a neighbored dot [181][150]. Thus, the increase in proximity between the particles could be achieved, which results in improved electron and hole transport without worsening of the desired quantum size tuning effect of colloidal CdSe QDs. Especially a good charge transport can be achieved if the linking molecules contain delocalized π orbitals (i.e. conjugated double bonds or aromatic rings), that is why 3,3',5,5'-tetramethylbenzidine containing two aromatic rings and hence a conjugated system of π electrons was chosen for our experiments. Furthermore, the cross-linking has one more beneficial effect – it should provide the stable passivation of the nanoparticles surfaces and thus produce quasi inert solid films.

As already mentioned in Chapter 2, addition of the cross-linker to the solution of CdSe QDs in pyridine results in immediate coagulation of the nanoparticles and makes them unsuitable for further processing. This is even despite the fact that the NCs are capped with pyridine ligands in the solution. Presumably, due to very strong affinity to Cd atoms, the linking molecules displace the weak pyridine ligands and thus form the networks of nanoparticles. The next cross-linking technique was the preparation of the CdSe/P3HT/cross-linker mixture, which was then used for the spin-coating of an active layer. It should be pointed out that both the solutions of the CdSe/P3HT/cross-linker and the films did not exhibit any visible drawbacks, such as inhomogeneity or film cracks. The last cross-linking procedure that we tried was immersing of the *a priori* prepared hybrid blends into diluted solutions of the linking substances. At this step, the solvent of the solutions with cross-linkers was chosen so that it would not dissolve both the CdSe nanoparticles and the polymer.

1,7-diaminoheptane (DAH)

The fourth quadrant of the J-V curves of the solar cells prepared using two different cross-linking techniques and a comparison solar cell with pyridine-treated CdSe QDs is depicted in Fig. 7.4[2]. Three major conclusions can be drawn from the represented curves.

First, it is evident that the comparison solar cell composed of the CdSe/P3HT active layer possesses the highest efficiency, and the cross-linking leads to dramatic six-fold decrease of the J_{sc} value. This result is astonishing, since it was reported that DAH increased the conductivity of the CdSe QDs films [182], and one would expect higher efficiency after the cross-linking procedure. However, it is possible that too strong linking effect of this compound leads to substantial changes in the film morphology, which results in the overall deterioration of the solar cells.

Second, it can be seen that the annealing step of the standard CdSe/P3HT-based solar cells is very important and results in better quality of the devices. Thus, samples 5 and 6 in Fig. 7.4 are the solar cells with and without thermal annealing, respectively. It is obvious that without heat treatment, the J_{sc} magnitude decreases by more than three times. This fact corroborates the results from the literature [5][176]. It has been

---

[2] To study the influence of the heat treatment on the performance of solar cells some films were annealed, which is indicated in the caption of Fig. 7.4 in detail. If present, annealing was done during 20 min at the temperature of 140 °C.

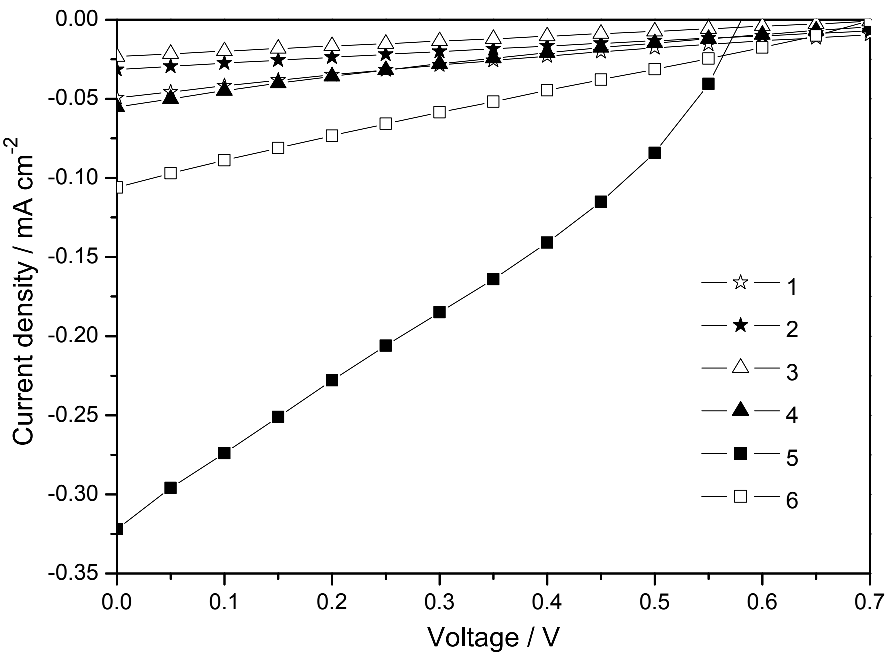

Figure 7.4: The fourth quadrant of the J-V curves of the hybrid solar cells fabricated with 1,7-diaminoheptane under illumination AM1.5G: (1) CdSe+P3HT+DAH film, annealed; (2) CdSe+P3HT+DAH film, without annealing; (3) CdSe+P3HT film, immersed for 10 min, dried at 70 ℃; (4) CdSe+P3HT film, annealed, immersed for 10 min, dried at 70 ℃; (5) CdSe+P3HT film, annealed; (6) CdSe+P3HT film, without annealing.

reported that annealing of the P3HT/CdSe composite films near the glass transition temperature of the polymer can, on the one hand, enhance the hole mobility in the polymer phase and, on the other hand, partly eliminate pyridine ligands for better electron transport between nanocrystals [176]. Furthermore, the removal of interfacial pyridine can also improve charge transfer between the CdSe QDs and the host polymer P3HT [5].

Third, if we compare samples 3 and 4 (Fig. 7.4), viz. CdSe/P3HT blends immersed into a cross-linker solution where sample 4 was annealed before the dipping and sample 3 was not, the beneficial effect of annealing on the performance of the solar cells with cross-linkers can be observed. The higher value of the current density for sample 4 indicates that DAH binds to the Cd sites and thermal treatment is necessary to remove the excess of pyridine ligands to make more Cd sites free, which is consistent with literature [5].

3,3',5,5'-tetramethylbenzidine (TMB)

Hoping to improve the efficiency of the solar cells, we chose another bifunctional molecule as a linker, i.e. 3,3',5,5'-tetramethylbenzidine (Fig. 7.3b), which contains besides two amino-groups two aromatic rings as well. We suggested that the conjugated system of π electrons in this substance should facilitate the charge transfer and thus lead to better results than 1,7-diaminoheptane, which has no π orbitals.

Fig. 7.5a shows the J-V characteristics of the standard CdSe/P3HT hybrid solar cell and the solar cell with TMB cross-linker in the dark and under simulated AM1.5G illumination in semi-logarithmic representation. It can be seen that both devices, with and without the cross-linker, behave like a rectifying diode and exhibit the photovoltaic response. The fourth quadrant of these two solar cells (samples 1 and 2, respectively) together with other devices after applying the cross-linker technique under illumination are depicted in Fig. 7.5b[3]. It can be seen that cells 1 and 2 (whose J-V characteristics in the dark and under illumination are represented in Fig. 7.5a) exhibit the highest magnitudes of J_{sc} and the fill factor (FF). The main characteristics of these two solar cells with best efficiencies are summarized in Table 7.2.

Table 7.2: Characteristic parameters of the solar cells produced from CdSe/P3HT active layer with and without cross-linking.

№	Sample	FF	$J_{sc}, mA \cdot cm^{-2}$	V_{oc}, V	$\eta, \%$
1	CdSe/P3HT film	0.47	0.83	0.49	0.19
2	CdSe/P3HT film with TMB	0.32	1.12	0.55	0.20

Sample 2 was produced by immersing the annealed film of the CdSe/P3HT blend

---

[3] All samples represented in Fig. 7.5 were annealed during 20 min at the temperature of 140 ℃ before evaporation of Al cathode. For sample 2 the heat treatment step was also applied before immersing it into the cross-linker solution. This is additionally indicated in the caption of Fig. 7.5.

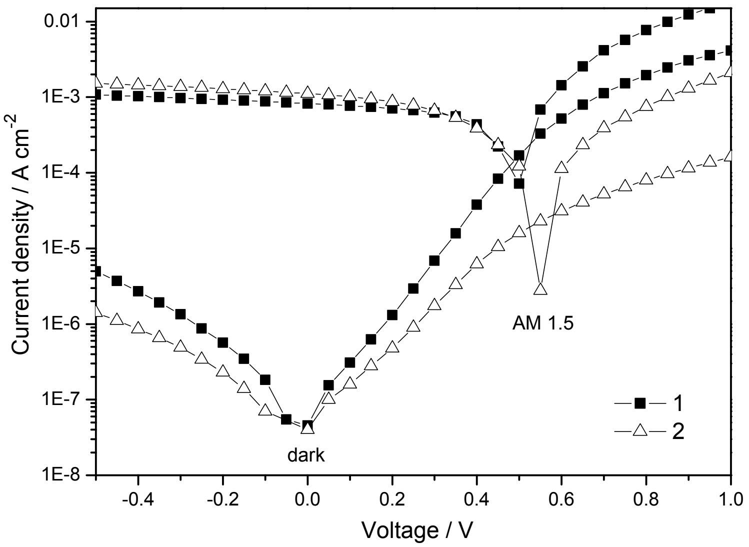

(a)

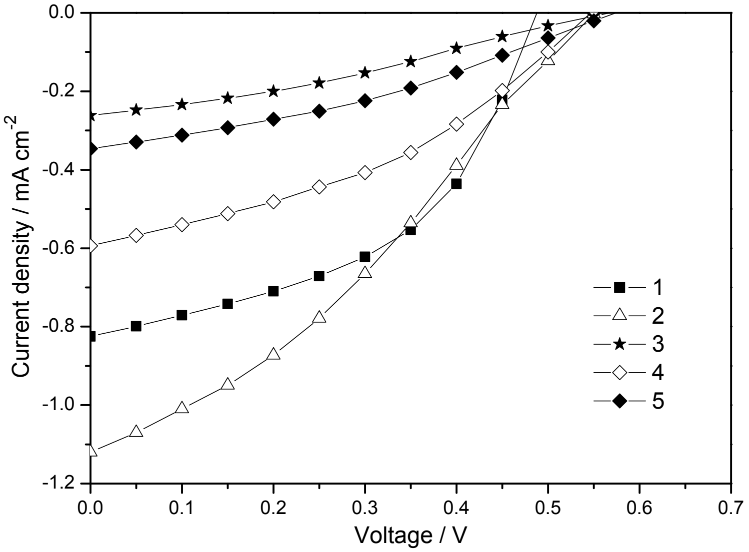

(b)

Figure 7.5: J-V curves of the solar cells fabricated with 3,3',5,5'-tetramethylbenzidine: (a) J-V characteristics of the hybrid solar cells in the dark and under illumination AM1.5G in semi-logarithmic representation: (1) CdSe+P3HT film, annealed; (2) CdSe+P3HT film, annealed, immersed for 30 min, annealed; (b) The fourth quadrant of the J-V curves of the hybrid solar cells fabricated with under illumination AM1.5G: (1) CdSe+P3HT film, annealed; (2) CdSe+P3HT film, annealed, immersed for 30 min, annealed; (3) CdSe+P3HT+TMB film, annealed; (4) CdSe+P3HT film, immersed for 10 min, annealed; (5) CdSe+P3HT film, immersed for 60 min, annealed.

into 5 mM solution of TMB in acetone for a duration of 30 min (then the post-linking annealing was applied as well). The similar fabricated devices but without the heat treatment before immersing into the cross-linker solution (samples 4 and 5 in Fig. 7.5b) show much lower J_{sc} and FF values. This suggests that in order to improve the photovoltaic responses of the hybrid solar cells by means of the cross-linking of TMB with CdSe QDs, it is necessary to anneal the CdSe/P3HT film before immersing it into the linker solution. Thermal annealing promotes the equilibrium morphology of a spin-cast film, enhances phase separation, and helps to evaporate redundant pyridine molecules [5]. This facilitates the attachment of the TMB molecules to form bridges between the nanoparticles. Presumably, the aromatic rings in the TMB are capable of directly intercepting one of the charge carries and transferring it further to the next-lying CdSe dot. That is why the short circuit current density of the hybrid solar cell shows a 25 % increase after the cross-linking (sample 2 in Fig. 7.5b). The V_{oc} of the solar cell that underwent the cross-linking procedure also has a higher value (0.55 vs. 0.49 V, Table 7.2). Unfortunately, the FF decreased from 0.47 to 0.32 (Table 7.2), however, this can probably be improved through further cell optimization. The value of PCE was calculated to be almost the same for the both samples (about 0.2 %, Table 7.2). The preparation of the devices with blends where a CdSe/P3HT/TMB mixture is spin-coated as an active layer (sample 3 in Fig. 7.5b) resulted in the lowest J_{sc} magnitude. This is probably due to the dramatic coagulation of the nanoparticles, which is caused by the cross-linking molecules and leads to the undesirable changes in the morphology of the films. So, it could also be concluded that the dipping method is better than the mixing of a cross-linker with a P3HT/CdSe solution for fabrication of the hybrid solar cells.

Thus, the beneficial effect of 3,3',5,5'-tetramethylbenzidine on both the short circuit current density and open circuit voltage values has been observed in hybrid solar cells. This is even despite the fact that no complete optimization of the laboratory solar cells such as film thickness, concentration of the linker solution, immersing time, etc. has been done yet. The preliminary results show that cross-linking is a promising approach to enhance the efficiency of the hybrid solar cells significantly after applying various optimization procedures.

7.3 Conclusions

To conclude, two series of hybrid P3HT/pyridine-treated CdSe QDs solar cells were investigated in our work. First, the solar cells were fabricated using CdSe NCs after the first, second and third steps of the pyridine treatment. For characterization, the I-V curves were measured and the main parameters of the solar cells (J_{sc}, V_{oc}, FF, PCE) were determined. Surprisingly, the efficiency of the photovoltaic devices deteriorated after incorporation of the multiple pyridine-treated CdSe QDs. Such behavior could be explained by the morphology of the hybrid blends. As it is evidenced by TEM images, CdSe NCs tend to aggregate after the multiple ligand exchange. This could lead to phase separation in the films which in turn impeded the efficient charge separation.

Second, CdSe QDs after one-fold pyridine treatment were cross-linked with two substances containing amino-end groups (DAH and TMB) to facilitate the charge transfer in the hybrid blends. Different cross-linking techniques as well as the influence of heat treatment on the film properties were studied. Cross-linking with 1,7-diaminoheptane was found to reduce the efficiency of the solar cells. On the contrary, using 3,3',5,5'-tetramethylbenzidine as a linking compound resulted in higher J_{sc} and V_{oc} values. Such positive result of TMB could be due to the presence of a conjugated system of π orbitals in its aromatic rings and shows that cross-linking is a promising strategy for future improvement of CdSe/P3HT hybrid solar cells.

Chapter 8

Summary

In this thesis, nearly monodisperse CdSe and CdS QDs were synthesized by a novel colloidal synthesis involving *in situ* formed Cd^0 particles that acted as a Cd precursor. Presence of Cd^0 particles in the course of the reaction regulates the monomer supply in the solution during the nanocrystal growth and results in high quality QDs. To investigate the growth kinetics of CdSe and CdS nanoparticles, reactions with different types of Se or S precursors, Cd to Se or S ratio, and concentrations of the stabilizer (oleic acid) were characterized by means of UV-Vis absorption spectroscopy. TEM confirmed that as-synthesized nanocrystals had a very narrow size distribution, although no post-preparative size-selection was applied. Unlike the S/ODE precursor which high reactivity over TOPS and TBPS solutions was well known, a Se/ODE precursor was considered to be less reactive than more commonly used in the CdSe QDs syntheses TOPSe and TBPSe. In our work, it was shown that special conditions are required to produce the Se/ODE precursor comparable in its reactivity with TOPSe and TBPSe solutions. Although the mass spectra of both Se/ODE and S/ODE precursors revealed the similar chemical composition, i.e. ODE_x-$Se_y(S_y)$ adducts and their decomposition products, the nature of chemical bonds in these solutions was found to be different. Thus, ^1H and ^{13}C NMR spectra suggested that in the case of S/ODE, the chemical interactions should be mainly van der Waals, whereas for Se/ODE, the covalent forces are likely to be dominant. Analysis of the ligand shell of CdSe and CdS QDs obtained with different precursors (both phosphine-free and phosphine ones) indicated that independent of the used Se or S precursor, the synthesized nanocrystals were only capped with OA molecules.

To facilitate the charge transfer between CdSe QDs for photovoltaic applications (in particular, for hybrid nanoparticle/polymer solar cells), the initial long-chained OA ligands were substituted with pyridine molecules. Additionally, pyridine treatment was found to be beneficial in the sense that it reduced the amount of organic impurities, which was evidenced by the XRD and TGA analyses. NMR and TGA measurements showed that after one-fold pyridine treatment, not all molecules of the original OA surfactants were replaced with pyridine. To achieve more efficient surface modification, the pyridine treatment was repeated two more times. However, even after three successive runs of the ligand exchange, 12 % of the surface cadmium sites remained passivated by OA molecules. The comparison of the UV-Vis absorption spectra of all samples revealed that the size and size distribution of the NCs did not change during the surface modification process; moreover, no signs of aggregation of the QDs in solution were observed. Differently, nanoparticles after the ligand exchange demonstrated a tendency to form aggregates on a TEM grid, which is in accordance with the findings that pyridine molecules are weaker stabilizing ligands than OA.

In the last part of the thesis, the impact of the pyridine-treated CdSe QDs on the performance of hybrid P3HT/CdSe solar cells was investigated. First, it was found that one-fold pyridine-treated nanoparticles resulted in better efficiency of laboratory solar cells in comparison to the multiple treated ones. Even though the repeated surface modification process resulted in a thinner ligand shell that should have enhanced the charge transfer, CdSe NCs tended to aggregate after multiple ligand exchange, as it was evidenced by TEM images. This could lead to undesirable phase separation in the films, which in turn impeded the efficient charge separation. Second, cross-linking procedure of one-fold pyridine-treated CdSe NCs was applied to improve the charge transport between nanoparticles. The beneficial effect of the cross-linking on J_{sc} and V_{oc} values was observed in the case of 3,3',5,5'-tetramethylbenzidine containing two aromatic rings and hence conjugated system of π orbitals that facilitated the charge transfer. Thus, it was shown that cross-linking is a promising strategy for future improvement of CdSe/P3HT hybrid solar cells.

Appendix A

Calculation of percentage of Cd and Se surface atoms

Eq. 6.7 on page 113 expresses the number of Cd surface sites (S). To calculate the number of both Cd and Se surface atoms, the magnitude S was multiplied by two. These values are shown in Table 4.1.

Then modifying Eq. 6.7, the whole number of Cd units both on the surface and in the core (S_{all}) is expressed as follows:

$$S_{all} = \left(\frac{4/3\pi r^3}{V}\right) \cdot N \tag{A.1}$$

Here, r is a mean radius of a CdSe nanoparticle (from absorbance), V is the volume of a CdSe unit cell (with radius of 0.608 nm), N is the number of CdSe units per unit cell (N = 4).

From the difference between the whole number of Cd or Se units S_{all} and their surface sites S, one can obtain a number of Cd or Se units in the core (S_{core}):

$$S_{core} = S_{all} - S \tag{A.2}$$

Taking into account the real ratio of Cd : Se obtained by EDX (Table 4.1), one can determine the number of all Se atoms:

$$N_{Se} = \frac{2 \cdot S_{all}}{1 + (Cd : Se)_{EDX}} \tag{A.3}$$

$2 \cdot S_{all}$ represents the whole number of both Cd and Se units.

The number of all Cd atoms is calculated then as a difference:

$$N_{Cd} = 2 \cdot S_{all} - N_{Se} \tag{A.4}$$

Finally, the number of Cd and Se surface atoms ($N_{Cd,surface}$ and $N_{Se,surface}$, respectively) can be obtained as follows:

$$N_{Cd,surface} = N_{Cd} - S_{core} \tag{A.5}$$

and

$$N_{Se,surface} = N_{Se} - S_{core} \tag{A.6}$$

The following equations allow to calculate the percentage of Cd and Se surface atoms, respectively:

$$\%_{Cd,surface} = \frac{N_{Cd,surface}}{2 \cdot S} \cdot 100\% \tag{A.7}$$

and

$$\%_{Se,surface} = \frac{N_{Se,surface}}{2 \cdot S} \cdot 100\% \tag{A.8}$$

These final magnitudes ($\%_{Cd,surface}$ and $\%_{Se,surface}$) are shown in Table 4.1.

Appendix B

Solar cell characterization

Power conversion efficiency (PCE) η is often used to describe the electrical characteristics of solar cells under illumination. It represents the ratio of the maximum obtainable electrical power (P_{max}) and the incident light power (I_{light}) [47]:

$$\eta = \frac{P_{max}}{I_{light}} \times 100\% \tag{B.1}$$

The maximum power point P_{max} is located in the fourth quadrant on the current density-voltage (J-V) curve and is determined by the maximum value of the product of current density J_{max} and voltage V_{max} (Fig. B.1). The (J-V) curve of an ideal solar cell would have a rectangular shape, and its efficiency would be determined as a light-dashed area in Fig. B.1, i.e. the product of the short-circuit current density (J_{sc}) and the open-circuit voltage (V_{oc}). However, real J-V characteristics are always curved and the efficiency of a real solar cell is shown as a dark-dashed area. The ratio between the actual maximum power output and the maximum theoretical power output is called fill factor (FF) [47]:

$$FF = \frac{P_{max}}{J_{sc} \cdot V_{oc}} \tag{B.2}$$

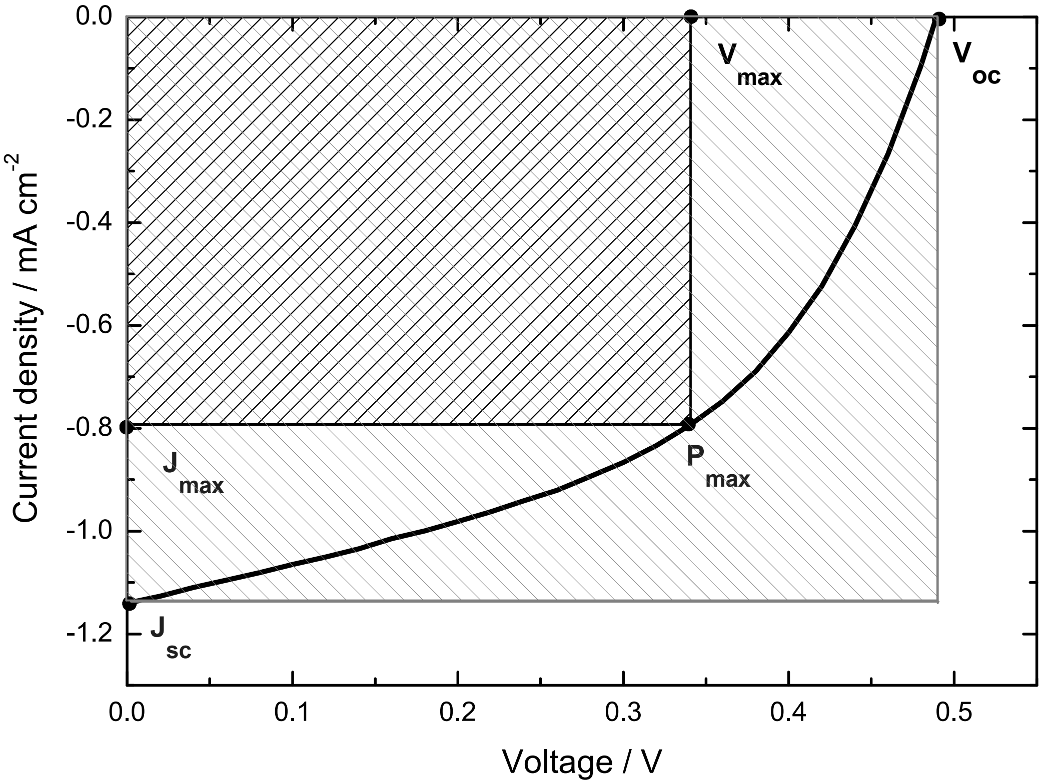

Figure B.1: Current density – voltage (J-V) curve of a solar cell under illumination.

The higher the FF the more electrical power can be extracted (usually it lies between 0.25 and 1.0). With Eq. B.2, Eq. B.1 can be written as:

$$\eta = \frac{J_{sc} \cdot V_{oc} \cdot FF}{I_{light}} \times 100\% \tag{B.3}$$

Hence, optimization of the solar cell performance requires maximizing each of there parameters J_{sc}, V_{oc}, FF. The power conversion efficiency η should be measured under standard test conditions, i.e. radiant density of 100 mW/cm^2 with a spectral distribution defined as AM1.5G at a cell temperature of 25 ℃.

Appendix C

R-phrases, S-phrases and their combinations

Table C.1: Safety precaution information on the used chemicals.

Substance	Hazard signs	R-phrases	S-phrases
Acetone	F, Xi	11-36-66-67	9-16-26-46
4-Aminothiophenol	C	20/21/22-34	26-27-36/37/39-45
Cadmium oxide	T+, N	45-26-48/23/25-62-63-68-50/53	45-53-60-61
Chlorbenzene	Xn, N	10-20-51/53	24/25-61
D-Chloroform	Xn	22-38-40-48/20/22	36/37
1,7-Diaminoheptane	Xi	36/38	–
Hexane	F, Xn, N	11-38-48/20-62-65-67-51/53	9-16-29-33-36/37-61-62
Methanol	T, F	11-23/24/25-39/23/24/25	7-16-24-36/37-45
1-Octadecene	Xn	53-65	61-62
Oleic acid	Xi	38	–
Pyridine	F, Xn	11-20/21/22	26-28
Selenium	T	23/25-33-53	20/21-28-45-61
Sulfur	Xi	38	46
Tri-n-butylphosphine	C, Xi	17-21/22-34	16-26-27-36/37/39
Tri-n-octylphosphine	C, Xi	34-36/37/38	26-36/37/39-45
3,3',5,5'-Tetramethylbenzidine	–	–	–

Risk (R-) and safety precaution (S-) phrases used in the classification, packaging, labeling, and provision of information on dangerous substances:

List of R-Phrases

R 1 Explosive when dry.
R 3 Extreme risk of explosion by shock, friction, fire or other sources of ignition.
R 4 Forms very sensitive explosive metallic compounds.
R 5 Heating may cause an explosion.
R 6 Explosive with or without contact with air.
R 7 May cause fire.
R 8 Contact with combustible material may cause fire.
R 9 Explosive when mixed with combustible material.
R 10 Flammable.
R 11 Highly flammable.
R 12 Extremely flammable.
R 13 Extremely flammable liquefied gas.
R 14 Reacts violently with water.
R 15 Contact with water liberates extremely flammable gases.
R 16 Explosive when mixed with oxidizing substances.
R 17 Spontaneously flammable in air.
R 18 In use, may form flammable/explosive vapour-air mixture.
R 19 May form explosive peroxides.
R 20 Harmful by inhalation.
R 21 Harmful in contact with skin.
R 22 Harmful if swallowed.
R 23 Toxic by inhalation.
R 24 Toxic in contact with skin.
R 25 Toxic if swallowed.
R 26 Very toxic by inhalation.
R 27 Very toxic in contact with skin.
R 28 Very toxic if swallowed.
R 29 Contact with water liberates toxic gas.
R 30 Can become highly flammable in use.
R 31 Contact with acids liberates toxic gas.
R 32 Contact with acids liberates very toxic gas.
R 33 Danger of cumulative effects.
R 34 Causes burns.
R 35 Causes severe burns.
R 36 Irritating to eyes.
R 37 Irritating to respiratory system.
R 38 Irritating to skin.
R 39 Danger of very serious irreversible effects.
R 40 Limited evidence of a carcinogenic effect.
R 41 Risk of serious damage to eyes.
R 42 May cause sensitization by inhalation.
R 43 May cause sensitization by skin contact.

R 44 Risk of explosion if heated under confinement.
R 45 May cause cancer.
R 46 May cause heritable genetic damage.
R 47 May cause birth defects.
R 48 Danger of serious damage to health by prolonged exposure.
R 49 May cause cancer by inhalation.
R 50 Very toxic to aquatic organisms.
R 51 Toxic to aquatic organisms.
R 52 Harmful to aquatic organisms.
R 53 May cause long-term adverse effects in the aquatic environment.
R 54 Toxic to flora.
R 55 Toxic to fauna.
R 56 Toxic to soil organisms.
R 57 Toxic to bees.
R 58 May cause long-term adverse effects in the environment.
R 59 Dangerous for the ozone layer.
R 60 May impair fertility.
R 61 May cause harm to the unborn child.
R 62 Possible risk of impaired fertility.
R 63 Possible risk of harm to the unborn child.
R 64 May cause harm to breastfed babies.
R 65 Harmful: may cause lung damage if swallowed.
R 66 Repeated exposure may cause skin dryness or cracking.
R 67 Vapours may cause drowsiness and dizziness.
R 68 Possible risk of irreversible effects.

Combinations of R-Phrases

R 14/15 Reacts violently with water, liberating extremely flammable gases.
R 15/29 Contact with water liberates toxic, extremely flammable gas.
R 20/21 Harmful by inhalation and in contact with skin.
R 20/21/22 Harmful by inhalation, in contact with skin and if swallowed.
R 20/22 Harmful by inhalation and if swallowed.
R 21/22 Harmful in contact with skin and if swallowed.
R 23/24 Toxic by inhalation and in contact with skin.
R 23/24/25 Toxic by inhalation, in contact with skin and if swallowed.
R 23/25 Toxic by inhalation and if swallowed.
R 24/25 Toxic in contact with skin and if swallowed.
R 26/27 Very toxic by inhalation and in contact with skin.
R 26/27/28 Very toxic by inhalation, in contact with skin and if swallowed.
R 26/28 Very toxic by inhalation and if swallowed.
R 27/28 Very toxic in contact with skin and if swallowed.
R 36/37 Irritating to eyes and respiratory system.
R 36/37/38 Irritating to eyes, respiratory system and skin.
R 36/38 Irritating to eyes and skin.
R 37/38 Irritating to respiratory system and skin.

R 39/23 Toxic: danger of very serious irreversible effects through inhalation.

R 39/23/24 Toxic: danger of very serious irreversible effects through inhalation and in contact with skin.

R 39/23/24/25 Toxic: danger of very serious irreversible effects through inhalation, in contact with skin and if swallowed.

R 39/23/25 Toxic: danger of very serious irreversible effects through inhalation and if swallowed.

R 39/24 Toxic: danger of very serious irreversible effects in contact with skin.

R 39/24/25 Toxic: danger of very serious irreversible effects in contact with skin and if swallowed.

R 39/25 Toxic: danger of very serious irreversible effects if swallowed.

R 39/26 Very toxic: danger of very serious irreversible effects through inhalation.

R 39/26/27 Very toxic: danger of very serious irreversible effects through inhalation and in contact with skin.

R 39/26/27/28 Very toxic: danger of very serious irreversible effects through inhalation, in contact with skin and if swallowed.

R 39/26/28 Very toxic: danger of very serious irreversible effects through inhalation and if swallowed.

R 39/27 Very toxic: danger of very serious irreversible effects in contact with skin.

R 39/27/28 Very toxic: danger of very serious irreversible effects in contact with skin and if swallowed.

R 39/28 Very toxic: danger of very serious irreversible effects if swallowed.

R 42/43 May cause sensitization by inhalation and skin contact.

R 48/20 Harmful: danger of serious damage to health by prolonged exposure through inhalation.

R 48/20/21 Harmful: danger of serious damage to health by prolonged exposure through inhalation and in contact with skin.

R 48/20/21/22 Harmful: danger of serious damage to health by prolonged exposure through inhalation, in contact with skin and if swallowed.

R 48/20/22 Harmful: danger of serious damage to health by prolonged exposure through inhalation and if swallowed.

R 48/21 Harmful: danger of serious damage to health by prolonged exposure in contact with skin.

R 48/21/22 Harmful: danger of serious damage to health by prolonged exposure in contact with skin and if swallowed.

R 48/22 Harmful: danger of serious damage to health by prolonged exposure if swallowed.

R 48/23 Toxic: danger of serious damage to health by prolonged exposure through inhalation.

R 48/23/24 Toxic: danger of serious damage to health by prolonged exposure through inhalation and in contact with skin.

R 48/23/24/25 Toxic: danger of serious damage to health by prolonged exposure through inhalation, in contact with skin and if swallowed.

R 48/25 Toxic: danger of serious damage to health by prolonged exposure if swallowed.

R 48/23/25 Toxic: danger of serious damage to health by prolonged exposure through inhalation and if swallowed.

R 48/24 Toxic: danger of serious damage to health by prolonged exposure in contact with skin.

R 48/24/25 Toxic: danger of serious damage to health by prolonged exposure in contact with skin and if swallowed.
R 48/25 Toxic: danger of serious damage to health by prolonged exposure if swallowed.
R 50/53 Very toxic to aquatic organisms, may cause long-term adverse effects in the aquatic environment.
R 51/53 Toxic to aquatic organisms, may cause long-term adverse effects in the aquatic environment.
R 52/53 Harmful to aquatic organisms, may cause long-term adverse effects in the aquatic environment.
R 68/20 Harmful: possible risk of irreversible effects through inhalation.
R 68/20/21 Harmful: possible risk of irreversible effects through inhalation and in contact with skin.
R 68/20/21/22 Harmful: possible risk of irreversible effects through inhalation, in contact with skin and if swallowed.
R 68/20/22 Harmful: possible risk of irreversible effects through inhalation and if swallowed.
R 68/21 Harmful: possible risk of irreversible effects in contact with skin.
R 68/21/22 Harmful: possible risk of irreversible effects in contact with skin and if swallowed.
R 68/22 Harmful: possible risk of irreversible effects if swallowed.

List of S-Phrases

S 1 Keep locked up.
S 2 Keep out of the reach of children.
S 3 Keep in a cool place.
S 4 Keep away from living quarters.
S 5 Keep contents under … (appropriate liquid to be specified by the manufacturer).
S 6 Keep under … (inert gas to be specified by the manufacturer).
S 7 Keep container tightly closed.
S 8 Keep container dry.
S 9 Keep container in a well-ventilated place.
S 12 Do not keep the container sealed.
S 13 Keep away from food, drink and animal feedingstuffs.
S 14 Keep away from … (incompatible materials to be indicated by the manufacturer).
S 15 Keep away from heat.
S 16 Keep away from sources of ignition - No smoking.
S 17 Keep away from combustible material.
S 18 Handle and open container with care.
S 20 When using do not eat or drink.
S 21 When using do not smoke.
S 22 Do not breathe dust.
S 23 Do not breathe .
S 24 Avoid contact with skin.
S 25 Avoid contact with eyes.
S 26 In case of contact with eyes, rinse immediately with plenty of water and seek medical advice.

S 27 Take off immediately all contaminated clothing.
S 28 After contact with skin, wash immediately with plenty of … (to be specified by the manufacturer).
S 29 Do not empty into drains.
S 30 Never add water to this product.
S 33 Take precautionary measures against static discharges.
S 34 Avoid shock and friction.
S 35 This material and its container must be disposed of in a safe way.
S 36 Wear suitable protective clothing.
S 37 Wear suitable gloves.
S 38 In case of insufficient ventilation, wear suitable respiratory equipment.
S 39 Wear eye / face protection.
S 40 To clean the floor and all objects contaminated by this material, use … (to be specified by the manufacturer).
S 41 In case of fire and / or explosion do not breathe fumes.
S 42 During fumigation / spraying wear suitable respiratory equipment.
S 43 In case of fire, use … (indicate in the space the precise type of firefighting equipment. If water increases risk, add ”Never use water”).
S 44 If you feel unwell, seek medical advice (show the label where possible).
S 45 In case of accident or if you feel unwell, seek medical advice immediately (show the label where possible).
S 46 If swallowed, seek medical advice immediately and show the container or label.
S 47 Keep at temperature not exceeding °C … (to be specified by the manufacturer).
S 48 Keep wet with .
S 49 Keep only in the original container.
S 50 Do not mix with … (to be specified by the manufacturer).
S 51 Use only in well-ventilated areas.
S 52 Not recommended for interior use on large surface areas.
S 53 Avoid exposure – obtain special instructions before use.
S 54 Obtain the consent of pollution control authorities before discharging to waste-water treatment plants.
S 55 Treat using the best available techniques before discharge into drains or the aquatic environment.
S 56 Dispose of this material and its container to hazardous or special waste collection point.
S 57 Use appropriate container to avoid environmental contamination.
S 58 To be disposed of as hazardous waste.
S 59 Refer to manufacturer / supplier for information on recovery / recycling.
S 60 This material and its container must be disposed of as hazardous waste.
S 61 Avoid release to the environment. Refer to special instructions / Safety data sheets.
S 62 If swallowed, do not induce vomiting: seek medical advice immediately and show the container or label.
S 63 In case of accident by inhalation: remove casualty to fresh air and keep at rest.
S 64 If swallowed, rinse mouth with water (only if the person is conscious).

Combinations of S-Phrases

S 1/2 Keep locked up and out of the reach of children.
S 3/7 Keep container tightly closed in a cool place.
S 3/9 Keep in a cool, well ventilated place.
S 3/7/9 Keep container tightly closed in a cool, well ventilated place.
S 3/9/14 Keep in a cool, well-ventilated place away from ... (incompatible materials to be indicated by the manufacturer).
S 3/9/49 Keep only in the original container in a cool, well-ventilated place.
S 3/9/14/49 Keep only in the original container in a cool, well-ventilated place away from ... (incompatible materials to be indicated by the manufacturer).
S 3/14 Keep in a cool place away from ... (incompatible materials to be indicated by the manufacturer).
S 7/8 Keep container tightly closed and dry.
S 7/9 Keep container tightly closed and in a well-ventilated place.
S 7/47 Keep container tightly closed and at a temperature not exceeding °C ... (to be specified by the manufacturer).
S 20/21 When using do not eat, drink or smoke.
S 24/25 Avoid contact with skin and eyes.
S 27/28 After contact with skin, take off immediately all contaminated clothing, and wash immediately with plenty of ... (to be specified by the manufacturer).
S 29/35 Do not empty into drains; dispose of this material and its container in a safe way.
S 29/56 Do not empty into drains, dispose of this material and its container at hazardous or special waste collection point.
S 36/37 Wear suitable protective clothing and gloves.
S 36/37/39 Wear suitable protective clothing, gloves and eye / face protection.
S 36/39 Wear suitable protective clothing and eye / face protection.
S 37/39 Wear suitable gloves and eye / face protection.
S 47/49 Keep only in the original container at a temperature not exceeding °C ... (to be specified by the manufacturer).

Bibliography

[1] A. P. Alivisatos. Perspectives on the physical chemistry of semiconductor nanocrystals. *J. Phys. Chem.*, 100:13226–13239, 1996.

[2] S. V. Gaponenko. *Optical Properties of Semiconductor Nanocrystals.* Cambridge University Press: Cambridge, U.K., 2005.

[3] H. Weller. Quantized semiconductor particles: a novel state of matter for materials science. *Adv. Mater.*, 5:88–95, 1993.

[4] M. Gao, C. Lesser, S. Kirstein, H. Mohwald, A. L. Rogach, and H. Weller. Electroluminescence of different colors form polycation/CdTe nanocrystal self-assembled films. *J. Appl. Phys.*, 87:2297–2302, 2000.

[5] W. U. Huynh, J. J. Dittmer, W. C. Libby, G. L. Whiting, and A. P. Alivisatos. Controlling the morphology of nanocrystal-polymer composites for solar cells. *Adv. Funct. Mater.*, 13:73–79, 2003.

[6] V. I. Klimov, A. A. Mikhailovsky, S. Xu, A. Malko, J. A. Hollingsworth, C. A. Leatherdale, H.-J. Eisler, and M. G. Bawendi. Optical gain and stimulated emission in nanocrystal quantum dots. *Adv. Mater.*, 290:314–317, 2000.

[7] R. J. Walters, P. G. Kik, J. D. Casperson, H. A. Atwater, R. Lindstedt, M. Giorgi, and G. Bourianoff. Silicon optical nanocrystal memory. *Appl. Phys. Lett.*, 85:2622–2624, 2004.

[8] M. Han, X. Gao, J. Z. Su, and S. O. Nie. Quantum-dot-tagged microbeads for multiplexed optical coding of biomolecules. *Nat. Biotechnol.*, 19:631–635, 2001.

[9] M. Green. Semiconductor quantum dots as biological imaging agents. *Angew. Chem. Int. Ed.*, 43:4129–4131, 2004.

[10] D. Pan, N. Zhao, Q. Wang, S. Jiang, X. Ji, and L. An. Facile synthesis and characterization of luminescent TiO_2 nanocrystals. *Adv. Mater.*, 17:1991–1995, 2005.

[11] T. W. Zeng, Y. Y. Lin, H. H. Lo, C. W. Chen, C. H. Chen, S. C. Liou, H. Y. Huang, and W. F. Su. A large interconnecting network within hybrid MEH-PPV/TiO_2 nanorod photovoltaic devices. *Nanotechnology*, 17:5387–5392, 2006.

[12] P. Bouvier, V. Dmitriev, and G. Lucazeau. The high-pressure phase sequence in nanocrystalline zirconia. *Eur. Phys. J. B*, 35:301–309, 2003.

[13] N. Zhao, D. Pan, W. Nie, and X. Ji. Two-phase synthesis of shape-controlled colloidal zirconia nanocrystals and their characterization. *J. Am. Chem. Soc.*, 128:10118–10124, 2006.

[14] J. F. Liu, Y. He, W. Chen, G. Q. Zhang, Y. W. Zeng, T. Kikegawa, and J. Z. Jiang. Bulk modulus and structural phase transitions of wurtzite CoO nanocrystals. *J. Phys. Chem. C*, 111:2–5, 2007.

[15] M. Boulova and G. Lucazeau. Crystallite nanosize effect on the structural transitions of WO_3 studied by raman spectroscopy. *J. Solid State Chem.*, 167:425–434, 2002.

[16] W. J. E. Beek, M. M. Wienk, and R. A. J. Janssen. Efficient hybrid solar cells from zinc oxide nanoparticles and a conjugated polymer. *Adv. Mater.*, 16:1009–1013, 2004.

[17] T. K. Sau, A. Pal, N. R. Jana, Z. L. Wang, and T. Pal. Size controlled synthesis of gold nanoparticles using photochemically prepared seed particles. *J. Nanopart. Res.*, 3:257–261, 2001.

[18] A. D. McFarland, C. L. Haynes, C. A. Mirkin, R. P. van Duyne, and H. A. Godwin. Color my nanoworld. *J. Chem. Educ.*, 81:544A, 2004.

[19] O. S. Ivanova and F. P. Zamborini. Size-dependent electrochemical oxidation of silver nanoparticles. *J. Am. Chem. Soc.*, 132:70–72, 2010.

[20] D. Fenske, H. Borchert, R. Kröger, M. Bäumer, J. Parisi, K. Al-Shamery, and J. Kolny-Olesiak. Colloidal synthesis of Pt nanoparticles: on the formation and stability of nanowires. *Langmuir*, 24:9011–9016, 2008.

[21] Y. K. Su, C. M. Shen, T. Z. Yang, H. T. Yang, H. J. Gao, and H. L. Li. The dependence of Co nanoparticle sizes on the ratio of surfactants and the influence of different crystal sizes on magnetic properties. *Appl. Phys. A*, 81:569–572, 2005.

[22] S. Chen, K. Huang, and J. A. Stearns. Alkanethiolate-protected palladium nanoparticles. *Chem. Mater.*, 12:540–547, 2000.

[23] M. Epifani, E. Pellicer, J. Arbiol, N. Sergent, T. Pagnier, and J. R. Morante. Capping ligand effects on the amorphous-to-crystalline transition of CdSe nanoparticles. *Langmuir*, 24:11182–11188, 2008.

[24] M. B. Mohamed, D. Tonti, A. Al Salman, and M. Chergui. Chemical synthesis and optical properties of size-selected CdSe tetrapod-shaped nanocrystals. *Chem. Phys. Chem.*, 6:2505–2507, 2005.

[25] I. Gur, N. A. Fromer, and A. P. Alivisatos. Controlled assembly of hybrid bulk heterojunction solar cells by sequential deposition. *J. Phys. Chem. B*, 110:25543–25546, 2006.

[26] W. W. Yu, Y. A. Wang, and X. Peng. Formation and stability of size-, shape- and structure-controlled CdTe nanocrystals: ligand effects on monomers and nanocrystals. *Chem. Mater.*, 15:4300–4308, 2003.

[27] A. Ghezelbash, B. Koo, and B. A. Korgel. Self-assembled stripe patterns of CdS nanorods. *Nano Lett.*, 6:1832–1836, 2006.

[28] T. Tanigaki, Y. Saito, T. Nakada, N. Tsuda, and C. Kaito. Structure of carbon-coated or silicon-oxide-coated ZnTe, ZnSe and ZnS nanoparticles produced by gas evaporation technique. *J. Nanopart. Res.*, 4:83–90, 2002.

[29] S. Kodiyalam, R. K. Kalia, A. Nakano, and P. Vashishta. Multiple grains in nanocrystals: effect of initial shape and size on transformed structures under pressure. *Phys. Rev. Lett.*, 93:203401, 2004.

[30] K. S. Hamad, R. Roth, J. Rockenberger, T. van Buuren, and A. P. Alivisatos. Structural disorder in colloidal InAs and CdSe nanocrystals observed by X-ray absorption near-edge spectroscopy. *Phys. Rev. Lett.*, 83:3474–3477, 1999.

[31] J. Zhu, X. Liao, J. Wang, and H.-Y. Chen. Photochemical synthesis and characterization of PbSe nanoparticles. *Mater. Res. Bull.*, 36:1169–1176, 2001.

[32] T. Mokari, M. Zhang, and P. Yang. Shape, size, and assembly control of PbTe nanocrystals. *J. Am. Chem. Soc.*, 129:9864–9865, 2007.

[33] X. Li, Y. He, S. S. Talukdar, and M. T. Swihart. Preparation of luminescent silicon nanoparticles by photothermal aerosol synthesis followed by acid etching. *Phase Transitions*, 77:131–137, 2004.

[34] A. P. Alivisatos. Semiconductor clusters, nanocrystals, and quantum dots. *Science*, 271:933–937, 1996.

[35] L. Qu and X. Peng. Control of photoluminescence properties of CdSe nanocrystals in growth. *J. Am. Chem. Soc.*, 124:2049–2055, 2002.

[36] D. Zhu, H. Ye, H. Zhen, and X. Liu. Improved performance in green light-emitting diodes made with CdSe-conjugated polymer composite. *Synthetic Met.*, 158:879–882, 2008.

[37] R. F. Louh, A. C. C. Chang, R. Wang, and C. H. Hsiao. Photoluminescence response and particle size control of CdSe quantum dots by wet chemical synthesis for biomedical applications. *Adv. Sci. Tech.*, 57:37–43, 2008.

[38] J. Chen, J. L. Song, X. W. Sun, W. Q. Deng, C. Y. Jiang, W. Lei, J. H. Huang, and R. S. Liu. An oleic acid-capped CdSe quantum-dot sensitized solar cell. *Appl. Phys. Lett.*, 94:153115, 2009.

[39] J. Kolny-Olesiak, V. Kloper, R. Osovsky, A. Sashchiuk, and E. Lifshitz. Synthesis and characterization of brightly photoluminescent CdTe nanocrystals. *Surf. Sci.*, 601:2667–2670, 2007.

[40] R. Osovsky, V. Kloper, J. Kolny-Olesiak, A. Sashchiuk, and E. Lifshitz. Optical properties of CdTe nanocrystal quantum dots, grown in the presence of Cd^0 nanoparticles. *J. Phys. Chem. C.*, 111:10841–10847, 2007.

[41] F. Zutz, I. Lokteva, N. Radychev, J. Kolny-Olesiak, I. Riedel, H. Borchert, and J. Parisi. Study of the influence of the Cd:Se precursor ratio during the synthesis of CdSe nanocrystals on the performance of CdSe/P3HT hybrid solar cells. *Phys. Status Solidi A*, 206:2700–2708, 2009.

[42] W. W. Yu, L. Qu, W. Guo, and X. Peng. Experimental determination of the extinction coefficient of CdTe, CdSe, and CdS nanocrystals. *Chem. Mater.*, 15:2854–2860, 2003.

[43] J. Nanda, S. Sapra, and D. D. Sarma. Size-selected zinc sulfide nanocrystallites: synthesis, structure and optical studies. *Chem. Mater.*, 12:1018–1024, 2000.

[44] H.-L. Li, Y.-C. Zhu, S.-G. Chen, O. Palchik, J.-P. Xiong, Y. Koltypin, Y. Gofer, and A. Gedanken. A novel ultrasound-assisted approach to the synthesis of CdSe and CdS nanoparticles. *J. Solid State Chem.*, 172:102–110, 2003.

[45] H. Borchert, E. V. Shevchenko, A. Robert, I. Mekis, A. Kornowski, G. Grübel, and H. Weller. Determination of nanocrystal sizes: a comparison of TEM, SAXS and XRD studies of highly monodisperse $CoPt_3$ particles. *Langmuir*, 21:1931–1936, 2005.

[46] H. Frohe, S. E. Shaheen, C. J. Brabec, D. C. Müller, N. S. Sariciftci, and K. Meerholz. Influence of the anodic work function on the performance of organic solar cells. *Chem. Phys. Chem.*, 3:795–799, 2002.

[47] W. J. E. Beek and R. A. J. Janssen. Hybrid polymer-inorganic photovoltaic cells. In L. Merhari, editor, *Hybrid Nanocomposites for Nanotechnology*. Springer US, 2009.

[48] V. K. LaMer and M. D. Barnes. Monodispersed hydrophobic colloidal dispersions and light scattering properties. i. preparation and light scattering properties of monodispersed colloidal sulfur. *J. Colloid. Sci.*, 1:71–77, 1946.

[49] V. K. LaMer and R. H. Dinegar. Theory, production and mechanism of formation of monodispersed hydrosols. *J. Am. Chem. Soc.*, 72:4847–4854, 1950.

[50] J. Park, J. Joo, S. G. Kwon, Y. Jang, and T. Hyeon. Synthesis of monodisperse spherical nanocrystals. *Angew. Chem. Int. Ed.*, 46:4630–4660, 2007.

[51] C. B. Murray, D. J. Norris, and M. G. Bawendi. Synthesis and characterization of nearly monodisperse CdE (E = S, Se, Te) semiconductor nanocrystallites. *J. Am. Chem. Soc.*, 115:8706–8715, 1993.

[52] W. W. Yu and X. Peng. Formation of high-quality CdS and other II-VI semiconductor nanocrystals in noncoordinating solvents: Tunable reactivity of monomers. *Angew. Chem. Int. Ed.*, 41:2368–2371, 2002.

[53] C. de Mello Donegá, P. Liljeroth, and D. Vanmaekelbergh. Physicochemical evaluation of the hot-injection method, a synthesis route for monodisperse nanocrystals. *Small*, 1:1152–1162, 2005.

[54] X. Peng, J. Wickham, and A. P. Alivisatos. Kinetics of II-VI and III-V colloidal semiconductor nanocrystal growth: "focusing" of size distributions. *J. Am. Chem. Soc.*, 120:5343–5344, 1998.

[55] J. van Embden and P. Mulvaney. Nucleation and growth of CdSe nanocrystals in a binary ligand system. *Langmuir*, 21:10226–10233, 2005.

[56] H. Reiss. The growth of uniform colloidal dispersions. *J. Chem. Phys.*, 19:482–487, 1951.

[57] L. Qu, W. W. Yu, and X. Peng. In situ observation of the nucleation and growth of CdSe nanocrystals. *Nano Lett.*, 4:465–469, 2004.

[58] C. R. Bullen and P. Mulvaney. Nucleation and growth kinetics of CdSe nanocrystals in octadecene. *Nano Lett.*, 4:2303–2307, 2004.

[59] D. V. Talapin, A. L. Rodach, M. Haase, and H. Weller. Evolution of an ensemble of nanoparticles in a colloidal solution: Theoretical study. *J. Phys. Chem. B*, 105:12278–12285, 2001.

[60] J. Thessing, J. Qian, H. Chen, N. Pradhan, and X. Peng. Interparticle influence on size/size distribution evolution of nanocrystals. *J. Am. Chem. Soc.*, 129:2736–2737, 2007.

[61] Y. Chen, E. Johnson, and X. Peng. Formation of monodisperse and shape-controlled MnO nanocrystals in non-injection synthesis: self-focusing via ripening. *J. Am. Chem. Soc.*, 129:10937–10947, 2007.

[62] J. van Embden, J. E. Sader, M. Davidson, and P. Mulvaney. Evolution of colloidal nanocrystals: theory and modeling of their nucleation and growth. *J. Phys. Chem. C*, 113:16342–16355, 2009.

[63] J. Y. Rempel, M. G. Bawendi, and K. F. Jensen. Insights into the kinetics of semiconductor nanocrystal nucleation and growth. *J. Am. Chem. Soc.*, 131:4479–4489, 2009.

[64] C. de Mello Donega, S. G. Hickey, S. F. Wuister, D. Vanmaekelbergh, and A. Meijerink. Single-step synthesis to control the photoluminescence quantum yield and size dispersion of CdSe nanocrystals. *J. Phys. Chem. B*, 107:489–496, 2003.

[65] D. V. Talapin, A. L. Rogach, A. Kornowski, M. Haase, and H. Weller. Highly luminescent monodisperse CdSe and CdSe/ZnS nanocrystals synthesized in a hexadecylamine – trioctylphosphine oxide – trioctylphospine mixture. *Nano Lett.*, 1:207–211, 2001.

[66] J. Jasieniak and P. Mulvaney. From Cd-rich to Se-rich - the manipulation of CdSe nanocrystal surface stoichiometry. *J. Am. Chem. Soc.*, 129:2841–2848, 2007.

[67] J. V. Williams, N. A. Kotov, and F. E. Savage. A rapid hot-injection method for the improved hydrothermal synthesis of CdSe nanoparticles. *Ind. Eng. Chem. Res.*, 48:4316–4321, 2009.

[68] L. E. Brus. A simple model for the ionization potential, electron affinity, and aqueous redox potentials of small semiconductor crystallites. *J. Chem. Phys.*, 79:5566–5571, 1983.

[69] M. L. Steigerwald, A. P. Alivisatos, J. M. Gibson, T. D. Harris, R. Kortan, A. J. Muller, A. M. Thayer, T. M. Duncan, D. C. Douglass, and L. E. Brus. Surface derivatization and isolation of semiconductor cluster molecules. *J. Am. Chem. Soc.*, 10:3046–3050, 1988.

[70] J. G. Brennan, T. Sigrist, P. J. Carroll, S. M. Stuczynski, L. E. Brus, and M. L. Steigerwald. The preparation of large semiconductor clusters via the pyrolysis of a molecular precursor. *J. Am. Chem. Soc.*, 11:4141–4143, 1989.

[71] A. Henglein. Photochemistry of colloidal cadmium sulfide. 2. effects of adsorbed methyl viologen and of colloidal platinum. *J. Phys. Chem.*, 86:2291–2293, 1982.

[72] L. Spanhel, M. Haase, H. Weller, and A. Henglein. Photochemistry of colloidal semiconductors. 20. surface modification and stability of strong luminescing CdS particles. *J. Am. Chem. Soc.*, 19:5649–5655, 1987.

[73] J. E. Bowen Katari, V. L. Colvin, and A. P. Alivisatos. X-ray photoelectron spectroscopy of CdSe nanocrystals with applications to studies of the nanocrystal surface. *J. Phys. Chem.*, 98:4109–4117, 1994.

[74] T. Trindade and P. O'Brien. A single source approach to the synthesis of CdSe nanocrystallites. *Adv. Mater.*, 8:161–163, 1996.

[75] T. Trindade and P. O'Brien. Synthesis of CdS and CdSe nanocrystallites using a novel single-molecule precursors approach. *Chem. Mater.*, 9:523–530, 1997.

[76] Z. A. Peng and X. Peng. Formation of high-quality CdTe, CdSe, and CdS nanocrystals using CdO as precursor. *J. Am. Chem. Soc.*, 123:183–184, 2001.

[77] L. H. Qu, Z. A. Peng, and X. Peng. Alternative routes toward high quality CdSe nanocrystals. *Nano Lett.*, 1:333–337, 2001.

[78] Z. A. Peng and X. Peng. Nearly monodisperse and shape controlled CdSe nanocrystals via alternative routes: Nucleation and growth. *J. Am. Chem. Soc.*, 124:3343–3353, 2002.

[79] Z. A. Peng and X. Peng. Mechanisms of the shape evolution of CdSe nanocrystals. *J. Am. Chem. Soc.*, 123:1389–1395, 2001.

[80] Z. Deng, L. Cao, F. Tang, and B. Zou. A new route to zinc-blende CdSe nanocrystals: mechanism and synthesis. *J. Phys. Chem. B*, 109:16671–16675, 2005.

[81] S. Sapra, A. L. Rogach, and J. Feldmann. Phosphine-free synthesis of monodisperse CdSe nanocrystals in olive oil. *J. Mater. Chem.*, 16:3391–3395, 2006.

[82] J. Jasieniak, C. Bullen, J. van Embden, and P. Mulvaney. Phosphine-free synthesis of CdSe nanocrystals. *J. Phys. Chem. B*, 109:20665–20668, 2005.

[83] V. Kloper, R. Osovsky, J. Kolny-Olesiak, A. Sashchiuk, and E. Lifshitz. The growth of colloidal cadmium telluride nanocrystal quantum dots in the presence of Cd^0 nanoparticles. *J. Phys. Chem. C.*, 111:10336–10341, 2007.

[84] H. Liu, J. S. Owen, and A. P. Alivisatos. Mechanistic study of precursor evolution in colloidal group II-VI semiconductor nanocrystal synthesis. *J. Am. Chem. Soc.*, 129:305–312, 2007.

[85] M. Sun and X. Yang. Phosphine-free synthesis of high-quality CdSe nanocrystals in noncoordination solvents: “activating agent” and “nucleating agent” controlled nucleation and growth. *J. Phys. Chem. C*, 113:8701–8709, 2009.

[86] M. Lardon. Selenium and proton nuclear magnetic resonance measurements on organic selenium compounds. *J. Am. Chem. Soc.*, 92:5063–5066, 1970.

[87] J. Z. Niu, H. Shen, H. Wang, W. Xu, S. Lou, Z. Du, and L. S. Li. Investigation on the phosphine-free synthesis of CdSe nanocrystals by cadmium precursor injection. *New J. Chem.*, 33:2114–2119, 2009.

[88] S. D. Bunge, K. M. Krueger, T. J. Boyle, M. A. Rodriguez, T. J. Headley, and V. L. Colvin. Growth and morphology of cadmium chalcogenides: the synthesis of nanorods, tetrapods, and spheres from CdO and $Cd(O_2CCH_3)_2$. *J. Mater. Chem.*, 13:1705–1709, 2003.

[89] X. Zhong, Y. Feng, and Y. Zhang. Facile and reproducible synthesis of red-emitting CdSe nanocrystals in amine with long-term fixation of particle size and size distribution. *J. Phys. Chem. C*, 111:526–531, 2007.

[90] H.-S. Chen and R. V. Kumar. Direct synthesis of quantum dots with controllable multimodal size distribution. *J. Phys. Chem. C*, 113:12236–12242, 2009.

[91] M. B. Mohamed, D. Tonti, A. Al-Salman, A. Chemseddine, and M. Chergui. Synthesis of high quality zinc blende CdSe nanocrystals. *J. Phys. Chem. B*, 109:10533–10537, 2005.

[92] Y. A. Yang, H. Wu, K. R. Williams, and Y. C. Cao. Synthesis of CdSe and CdTe nanocrystals without precursor injection. *Angew. Chem. Int. Ed.*, 44:6712–6715, 2005.

[93] D. Tonti, M. B. Mohammed, A. Al-Salman, P. Pattison, and M. Chergui. Multimodal distribution of quantum confinement in ripened CdSe nanocrystals. *Chem. Mater.*, 20:1331–1339, 2008.

[94] D. Wu, M. E. Kordesch, and P. G. van Patten. A new class of capping ligands for CdSe nanocrystal synthesis. *Chem. Mater.*, 17:6436–6441, 2005.

[95] Q. Dai, D. Li, H. Chen, S. Kan, H. Li, S. Gao, Y. Hou, B. Liu, and G. Zou. Colloidal CdSe nanocrystals synthesized in noncoordinating solvents with the addition of a secondary ligand: Exceptional growth kinetics. *J. Phys. Chem. B*, 110:16508–16513, 2006.

[96] C. Wang, Y. Jiang, L. Chen, S. Li, G. Li, and Z. Zhang. Temperature dependence of optical properties and size tunability CdSe quantum dots via non-TOP synthesis. *Mater. Chem. Phys.*, 116:388–391, 2009.

[97] A. Venkateswara Rao, G. M. Pajonk, and N. N. Parvathy. Preparation and characterization of nanocrystalline CdS doped monolithic and transparent TEOS silica xerogels using sol-gel method. *Mater. Chem. Phys.*, 48:234–239, 1997.

[98] N. V. Hullavarad and S. S. Hullavarad. Synthesis and characterization of monodispersed CdS nanoparticles in SiO_2 fibers by sol-gel method. *Photonics and Nanostructures*, 5:156–163, 2007.

[99] R. J. Bandaranayake, G. W. Wen, J. Y. Lin, H. X. Jiang, and C. M. Sorensen. Structural phase behavior in II-VI semiconductor nanoparticles. *Appl. Phys. Lett.*, 67:831–833, 1995.

[100] M. G. Sandoval-Paz, M. Sotelo-Lerma, A. Mendoza-Galvan, and R. Ramirez-Bon. Optical properties and layer microstructure of CdS films obtained from an ammonia-free chemical bath deposition process. *Thin Solid Films*, 515:3356–3362, 2007.

[101] M. Karimi, M. Rabiee, F. Moztarzadeh, M. Tahriri, and M. Bodaghi. Controlled synthesis, characterization and optical properties of CdS nanocrystalline thin films via chemical bath deposition (CBD) route. *Curr. Appl. Phys.*, 9:1263–1268, 2009.

[102] S. Pethkar, R. C. Patil, J. A. Kher, and K. Vijayamohanan. Deposition and characterization of CdS nanoparticle/polyaniline composite films. *Thin Solid Films*, 349:105–109, 1999.

[103] G. Q. Xu, B. Liu, S. J. Xu, C. H. Chew, S. J. Chua, and L. M. Gana. Luminescence studies of CdS spherical particles via hydrothermal synthesis. *J. Phys. Chem. Solid*, 61:829–836, 2000.

[104] C. Li, X. Yang, B. Yang, Y. Yan, and Y. Qian. Growth of microtubular complexes as precursors to synthesize nanocrystalline ZnS and CdS. *J. Cryst. Growth*, 291:45–51, 2006.

[105] M. Salavati-Niasari, M. R. Loghman-Estarki, and F. Davar. Controllable synthesis of nanocrystalline CdS with different morphologies by hydrothermal process in the presence of thioglycolic acid. *Chem. Eng. J.*, 145:346–350, 2008.

[106] Q. Wang, G. Xu, and G. Han. Solvothermal synthesis and characterization of uniform CdS nanowires in high yield. *J. Solid State Chem.*, 178:2680–2685, 2005.

[107] S. Q. Sun and T. Li. Synthesis and characterization of CdS nanoparticles and nanorods via solvo-hydrothermal route. *Cryst. Growth Des.*, 7:2367–2371, 2007.

[108] J. Álvarez Ruiz, M. López-Arias, R. de Nalda, M. Martín, A. Arregui, and L. Bañares. Generation of CdS clusters using laser ablation: the role of wavelength and fluence. *Appl. Phys. A*, 95:681–687, 2009.

[109] S. Emin, N. Sogoshi, S. Nakabayashi, M. Villeneuve, and C. Dushkin. Growth kinetics of CdS quantum dots and synthesis of their polymer nano-composites in CTAB reverse micelles. *J. Photochem. Photobiol. A: Chem.*, 207:173–180, 2009.

[110] K. G. Kanade, R. R. Hawaldar, R. Pasricha, S. Radhakrishnan, T. Seth, U. P. Mulik, B. B. Kale, and D. P. Amalnerkar. Novel polymer-inorganic solid-state reaction for the synthesis of CdS nanocrystallites. *Mater. Lett.*, 59:554–559, 2005.

[111] J. Liu, J. Cao, Z. Li, G. Ji, S. Deng, and M. Zheng. Low-temperature solid-state synthesis and phase-controlling studies of CdS nanoparticles. *J. Mater. Sci.*, 42:1054–1059, 2007.

[112] Y. C. Cao and J. Wang. One-pot synthesis of high-quality zinc-blende CdS nanocrystals. *J. Am. Chem. Soc.*, 126:14336–14337, 2004.

[113] J. Ouyang, J. Kuijper, S. Brot, D. Kingston, X. Wu, D. M. Leek, M. Z. Hu, J. A. Ripmeester, and K. Yu. Photoluminescent colloidal CdS nanocrystals with high quality via noninjection one-pot synthesis in 1-octadecene. *J. Phys. Chem. C*, 113:7579–7593, 2009.

[114] H. Li, W. Y. Shih, and W.-H. Shih. Synthesis and characterization of aqueous carboxyl-capped CdS quantum dots for bioapplications. *Ind. Eng. Chem. Res.*, 46:2013–2019, 2007.

[115] L. Zou, Z. Fang, Z. Gu, and X. Zhong. Aqueous phase synthesis of biostabilizer capped CdS nanocrystals with bright emission. *J. Lumin.*, 129:536–540, 2009.

[116] R. K. Sharma, S. N. Sharma, and A. C. Rastogi. Optical properties of CdS nanoclusters: effects of size, stoichiometry and alloying with Ag_2S. *Curr. Appl. Phys.*, 3:257–262, 2003.

[117] S.-W. Yeh, T.-L. Wu, and K.-H. Wei. Spatial position control of pre-synthesized CdS nanoclusters using a self-assembled diblock copolymer template. *Nanotechnology*, 16:683–687, 2005.

[118] M. C. Troparevsky and J. R. Chelikowsky. Structural and electronic properties of CdS and CdSe clusters. *J. Chem. Phys.*, 114:943, 2001.

[119] J.-O. Joswig, S. Roy, P. Sarkar, and M. Springborg. Stability and bandgap of semiconductor clusters. *Chem. Phys. Lett.*, 365:75–81, 2002.

[120] H.-Y. Chu, Z.-X. Liu, G.-L. Qiu, Kong D.-G., S.-X. Wu, Y.-C. Li, and Z.-L. Du. First-principles study of structures and electronic properties of cadmium sulfide clusters. *Chin. Phys. B*, 17:2478–2483, 2008.

[121] D. Pan, X. Ji, L. An, and Y. Lu. Observation of nucleation and growth of CdS nanocrystals in a two-phase system. *Chem. Mater.*, 20:3560–3566, 2008.

[122] Q. Yu and C.-Y. Liu. Study of magic-size-cluster mediated formation of CdS nanocrystals: Properties of the magic-size clusters and mechanism implication. *J. Phys. Chem. C*, 113:12766–12771, 2009.

[123] M. Li, J. Ouyang, C. I. Ratcliffe, L. Pietri, Wu X., D. M. Leek, I. Moudrakovski, Q. Lin, B. Yang, and K. Yu. CdS magic-sized nanocrystals exhibiting bright band gap photoemission via thermodynamically driven formation. *ASC Nano*, 3:3832–3838, 2009.

[124] A. Kasuya, R. Sivamohan, Y. A. Barnakov, I. M. Dmitruk, T. Nirasawa, V. R. Romanyuk, V. Kumar, S. V. Mamykin, K. Tohji, B. Jeyadevan, K. Shinoda, T. Kudo, O. Terasaki, Z. Liu, R. V. Belosludov, V. Sundararajan, and Y. Kawazoe. Ultra-stable nanoparticles of CdSe revealed from mass spectrometry. *Nat. Mater.*, 3:99–102, 2004.

[125] M. C. Troparevsky, L. Kronik, and J. R. Chelikowsky. Ab initio absorption spectra of CdSe clusters. *Phys. Rev. B*, 65:033311, 2001.

[126] H.-G. Boyen, G. Kästle, F. Weigl, B. Koslowski, C. Dietrich, P. Ziemann, J. P. Spatz, S. Riethmüller, C. Hartmann, M. Möller, G. Schmid, M. G. Garnier, and P. Oelhafen. Oxidation-resistant gold-55 clusters. *Science*, 297:1533–1536, 2002.

[127] S. Stoeva, K. J. Klabunde, C. M. Sorensen, and I. Dragieva. Gram-scale synthesis of monodisperse gold colloids by the solvated metal atom dispersion method and digestive ripening and their organization into two- and three-dimensional structures. *J. Am. Chem. Soc.*, 124:2305–2311, 2002.

[128] T. Vossmeyer, G. Reck, L. Katsikas, E. T. K. Haupt, B. Schulz, and H. Weller. A "double-diamond superlattice" built up of $Cd_{17}S_4(SCH_2CH_2OH)_{26}$ clusters. *Science*, 267:1476–1479, 1995.

[129] D. Pan, S. Jiang, L. An, and B. Jiang. Controllable synthesis of highly luminescent and monodisperse CdS nanocrystals by a two-phase approach under mild conditions. *Adv. Mater.*, 16:982–985, 2004.

[130] Q. Yu, C. Liu, Z. Zhang, and Y. Liu. Facile synthesis of semiconductor and noble metal nanocrystals in high-boiling two-phase liquid/liquid systems. *J. Phys. Chem. C*, 112:2266–2270, 2008.

[131] J. Ouyang, B. Zaman, F. Yan, D. Johnston, G. Li, X. Wu, D. M. Leek, C. I. Ratcliffe, J. A. Ripmeester, and K. Yu. Multiple families of magic-sized CdSe nanocrystals with strong bandgap photoluminescence via noninjection one-pot syntheses. *J. Phys. Chem. C*, 112:13805–13811, 2008.

[132] R. Wang, J. Ouyang, S. Nikolaus, L. Brestaz, M. B. Zaman, X. Wu, D. Leek, C. I. Ratcliffe, and K. Yu. Single-sized colloidal CdTe nanocrystals with strong bandgap photoluminescence. *Chem. Commun.*, pages 962–964, 2009.

[133] N. Herron, J. C. Calabrese, W. E. Farneth, and Y. Wang. Crystal structure and optical properties of $Cd_{32}S_{14}(SC_6H_5)_{36} \cdot DMF_4$, a cluster with a 15 angstrom CdS core. *Science*, 259:1426–1428, 1993.

[134] Q. Dai, D. Li, J. Chang, Y. Song, S. Kan, H. Chen, B. Zou, W. Xu, S. Xu, B. Liu, and G. Zou. Facile synthesis of magic-sized CdSe and CdTe nanocrystals with tunable existence periods. *Nanotechnology*, 18:405603, 2007.

[135] P. Dagtepe, V. Chikan, J. Jasinski, and V. J. Leppert. Quantized growth of CdTe quantum dots; observation of magic-sized CdTe quantum dots. *J. Phys. Chem. C*, 111:14977–14983, 2007.

[136] G. Kalyuzhny and R. W. Murray. Ligand effects on optical properties of CdSe nanocrystals. *J. Phys. Chem. B*, 109:7012–7021, 2005.

[137] A. M. Munro, J. A. Bardecker, M. S. Liu, Y.-J. Cheng, Y.-H. Niu, I. J.-L. Plante, A. K.-Y. Jen, and D. S. Ginger. Colloidal CdSe quantum dot electroluminescence: ligands and light-emitting diodes. *Microchim. Acta*, 160:345–350, 2008.

[138] W. W. Yu, J. C. Falkner, B. S. Shih, and V. L. Colvin. Preparation and characterization of monodisperse PbSe semiconductor nanocrystals in a noncoordinating solvent. *Chem. Mater.*, 16:3318–3322, 2004.

[139] M. D. Heinemann, K. von Maydell, F. Zutz, J. Kolny-Olesiak, H. Borchert, I. Riedel, and J. Parisi. Photoinduced charge transfer and relaxation of persistent charge carriers in polymer/nanocrystal composites for applications in hybrid solar cells. *Adv. Funct. Mater.*, 19:3788–3795, 2009.

[140] G. G. Yordanov, H. Yoshimura, and C. D. Dushkin. Fine control of the growth and optical properties of CdSe quantum dots by varying the amount of stearic acid in a liquid paraffin matrix. *Colloid. Surface A: Physicochem. Eng. Aspect*, 322:177–182, 2008.

[141] S. O. Oluwafemi and N. Revaprasadu. Study on growth kinetics of hexadecylamine capped CdSe nanoparticles using its electronic properties. *Phys. B: Condens. Matter*, 404:1204–1208, 2009.

[142] K. Nose, H. Fujita, T. Omata, S. Otsuka-Yao-Matsuo, H. Nakamura, and H. Maeda. Chemical role of amines in the colloidal synthesis of CdSe quantum dots and their luminescence properties. *J. Lumin.*, 126:21–26, 2007.

[143] M. Q. Zhu, E. Chang, J. Sun, and R. A. Drezek. Surface modification and functionalization of semiconductor quantum dots through reactive coating of silanes in toluene. *J. Mater. Chem.*, 17:800–805, 2007.

[144] X. Peng, T. E. Wilson, A. P. Alivisatos, and P. G. Schultz. Synthesis and isolatin of a homodimer of cadmium selenide nanocrystals. *Angew. Chem. Int. Ed. Engl.*, 36:145–147, 1997.

[145] W. H. Binder, R. Sachsenhofer, C. J. Straif, and R. Zirbs. Surface-modified nanoparticles *via* thermal and Cu(I)-mediated “click” chemistry: Generation of luminescent CdSe nanoparticles with polar ligands guiding supramolecular recognition. *J. Mater. Chem.*, 17:2125–2132, 2007.

[146] B. von Holt, S. Kudera, A. Weiss, T. E. Schrader, L. Manna, W. J. Parake, and M. Braun. Ligand exchange of CdSe nanocrystals probed by optical spectroscopy in the visible and mid-IR. *J. Mater. Chem.*, 18:2728–2732, 2008.

[147] C. Zhang, S. O’Brien, and L. Balogh. Comparison and stability of CdSe nanocrystals covered with amphiphilic poly(amidoamine) dendrimers. *J. Phys. Chem. B*, 106:10316–10321, 2002.

[148] Y. A. Wang, J. J. Li, H. Chen, and X. Peng. Stabilization of inorganic nanocrystals by organic dendrons. *J. Am. Chem. Soc.*, 124:2293–2298, 2002.

[149] N. C. Greenham, X. G. Peng, and A. P. Alivisatos. Charge separation and transport in conjugated-polymer/semiconductor-nanocrystal composites studied by photoluminescence quenching and photoconductivity. *Phys. Rev. B*, 54:17628–17637, 1996.

[150] G. I. Koleilat, L. Levina, H. Shukla, S. H. Myrskog, S. Hinds, A. G. Pattantyus-Abraham, and E. H. Sargent. Efficient, stable infrared photovoltaics based on solution-cast colloidal quantum dots. *ACS Nano*, 2:833–840, 2008.

[151] M. K. Mandal and P. K. Bhattacharya. Poly(ether-block-amide) membrane for pervaporative separation of pyridine present in low concentration in aqueous solution. *J. Membr. Sci.*, 286:115–124, 2006.

[152] X. Peng, M. C. Schlamp, A. V. Kadavanich, and A. P. Alivisatos. Epitaxial growth of highly luminescent CdSe/CdS core/shell nanocrystals with photostability and electronic accessibility. *J. Am. Chem. Soc.*, 119:7019–7029, 1997.

[153] P. Guyot-Sionnest, M. Shim, C. Matranga, and M. Hines. Intraband relaxation in CdSe quantum dots. *Phys. Rev. B*, 60:R2181–R2184, 1999.

[154] B. S. Kim, L. Avila, L. E. Brus, and I. P. Hermana. Organic ligand and solvent kinetics during the assembly of CdSe nanocrystal arrays using infrared attenuated total reflection. *Appl. Phys. Lett.*, 76:3715–3717, 2000.

[155] X. Ji, D. Copenhaver, C. Sichmeller, and X. Peng. Ligand bonding and dynamics on colloidal nanocrystals at room temperature: The case of alkylamines on CdSe nanocrystals. *J. Am. Chem. Soc.*, 130:5726–5735, 2008.

[156] S. Trotzky, J. Kolny-Olesiak, S. M. Falke, T. Hoyer, C. Lienau, W. Tuszynski, and J. Parisi. Ligand removal from soluble CdTe nanocrystals evidenced by time-resolved photoluminescence spectroscopy. *J. Phys. D: Appl. Phys.*, 41:102004, 2008.

[157] V. M. Dzhagan, I. Lokteva, M. Ya. Valakh, O. E. Raevska, J. Kolny-Olesiak, and D. R. T. Zahn. Spectral features above LO phonon frequency in resonant raman scattering spectra of small CdSe nanoparticles. *J. Appl. Phys.*, 106:084318, 2009.

[158] M. Kuno, J. K. Lee, B. O. Dabbousi, F. V. Mikulec, and M. G. Bawendi. The band edge luminescence of surface modified CdSe nanocrystallites: Probing the luminescing state. *J. Chem. Phys.*, 106:9869–9882, 1997.

[159] V. Protasenko, D. Bacinello, and M. Kuno. Experimental determination of the absorption cross-section and molar extinction coefficient of CdSe and CdTe nanowires. *J. Phys. Chem. B*, 110:25322–25331, 2006.

[160] W. Zhang, C. Wang, L. Zhang, X. Zhang, X. Liu, K. Tang, and Y. Qian. Room temperature synthesis of cubic nanocrystalline CdSe in aqueous solution. *J. Solid State Chem.*, 151:242–244, 2000.

[161] P. K. Khanna, K. Srinivasa Rao, K. R. Patil, V. N. Singh, and B. R. Mehta. One-pot synthesis of oleic acid-capped cadmium chalcogenides (CdE: E = Se, Te) nano-crystals. *J. Nanopart. Res.*, 12:101–109, 2010.

[162] E. E. Foos, J. Wilkinson, A. J. Mäkinen, N. J. Watkins, Z. H. Kafafi, and J. P. Long. Synthesis and surface composition study of CdSe nanoclusters prepared using solvent systems containing primary, secondary, and tertiary amines. *Chem. Mater.*, 18:2886–2894, 2006.

[163] S. Kumar and G. D. Scholes. Colloidal nanocrystal solar cells. *Microchim. Acta*, 160:315–325, 2008.

[164] B. R. Saunders and M. L. Turner. Nanoparticle–polymer photovoltaic cells. *Adv. Colloid. Interface Sci.*, 138:1–23, 2008.

[165] G. Yu, J. Gao, J. C. Hummelen, F. Wudl, and A. J. Heeger. Polymer photovoltaic cells: Enhanced efficiencies via a network of internal donor-acceptor heterojunctions. *Science*, 270:1789–1791, 1995.

[166] W. U. Huynh, J. J. Dittmer, and A. P. Alivisatos. Hybrid nanorod-polymer solar cells. *Science*, 295:2425–2427, 2002.

[167] J. Y. Kim, K. Lee, N. E. Coates, D. Moses, T.-Q. Nguyen, M. Dante, and A. J. Heeger. Efficient tandem polymer solar cells fabricated by all-solution processing. *Science*, 317:222–225, 2007.

[168] B. Sun, H. J. Snaith, A. S. Dhoot, S. Westenhoff, and N. C. Greenham. Vertically segregated hybrid blends for photovoltaic devices with improved efficiency. *J. Appl. Phys.*, 97:014914, 2004.

[169] B. Sun and N. C. Greenham. Improved efficiency of photovoltaics based on CdSe nanorods and poly(3-hexylthiophene) nanofibers. *Phys. Chem. Chem. Phys.*, 8:3557–3560, 2006.

[170] I. Gur, N. A. Fromer, C. P. Chen, A. G. Kanaras, and A. P. Alivisatos. Hybrid solar cells with prescribed nanoscale morphologies based on hyperbranched semiconductor nanocrystals. *Nano Lett.*, 7:409–414, 2007.

[171] Y. Liu, L. Wang, and Y. Cao. Photovoltaic devices from CdSe nanocrystals and conjugated polymer composites. *Front. Chem. China*, 2:383–386, 2007.

[172] J. D. Olson, G. P. Gray, and S. A. Carter. Optimizing hybrid photovoltaics through annealing and ligand choice. *Sol. Energy Mater. Sol. Cells*, 93:519–523, 2009.

[173] W. U. Huynh, X. Peng, and A. P. Alivisatos. CdSe nanocrystal rods/poly(3-hexylthiophene) composite photovoltaic devices. *Adv. Mater.*, 11:923–927, 1999.

[174] B. Sun, E. Marx, and N. C. Greenham. Photovoltaic devices using blends of branched CdSe nanoparticles and conjugated polymers. *Nano Lett.*, 3:961–963, 2003.

[175] Y. Zhou, F. S. Riehle, Y. Yuan, H.-F. Schleiermacher, M. Niggemann, G. A. Urban, and M. Krüger. The improved efficiency of hybrid solar cells based on non-ligand-exchanged CdSe quantum dots and poly(3-hexylthiophene). *Appl. Phys. Lett.*, 96:013304, 2010.

[176] D. S. Ginger and N. C. Greenham. Charge injection and transport in films of CdSe nanocrystals. *J. Appl. Phys.*, 87:1361, 2000.

[177] L. Han, D. Qin, X. Jang, Y. Liu, and Y. Cao. Synthesis of high quality zinc-blende CdSe nanocrystals and their application in hybrid solar cells. *Nanotechnology*, 17:4736–4742, 2006.

[178] C. Querner, P. Reiss, S. Sadki, M. Zagorska, and A. Pron. Size and ligand effects on the electrochemical and spectroelectrochemical responses of CdSe nanocrystals. *Phys. Chem. Chem. Phys.*, 7:3204–3209, 2005.

[179] J. Seo, W. J. Kim, S. J. Kim, K.-S. Lee, A. N. Cartwright, and P. N. Prasad. Polymer nanocomposite photovoltaics utilizing CdSe nanocrystals capped with a thermally cleavable solubilizing ligand. *Appl. Phys. Lett.*, 94:133302, 2009.

[180] I. Lokteva, N. Radychev, F. Witt, H. Borchert, J. Parisi, and J. Kolny-Olesiak. Surface treatment of CdSe nanoparticles for application in hybrid solar cells: The effect of multiple ligand exchange with pyridine. *J. Phys. Chem. C*, 114:12784–12791, 2010.

[181] M. A. Islam, Y. Xia, D. A. Telesca Jr., M. L. Steigerwald, and I. P. Herman. Controlled electrophoretic deposition of smooth and robust films of CdSe nanocrystals. *Chem. Mater.*, 16:49–54, 2004.

[182] D. Yu, C. Wang, and P. Guyot-Sionnest. n-type conducting CdSe nanocrystal solids. *Science*, 300:1277–1280, 2003.

[183] P. Guyot-Sionnest and C. Wang. Fast voltammetric and electrochromic response of semiconductor nanocrystal thin films. *J. Phys. Chem. B*, 107:7355–7359, 2003.

Acknowledgments

This work was completed under supervision of Jun.-Prof. Dr. Joanna Kolny-Olesiak at the Carl von Ossietzky Universität Oldenburg, Institut für Physik, Abteilung Energie- und Halbleiterforschung (Arbeitsgruppe von Prof. Dr. Jürgen Parisi).

I would like to thank all my colleagues and especially

Jun.-Prof. Dr. Joanna Kolny-Olesiak for providing me the opportunity to work on this interesting topic, guidance and motivation throughout this work, many fruitful and interesting discussions, as well as thorough reading of this thesis;

Prof. Dr. Jürgen Parisi for his support and agreement to referee this thesis;

Dr. Holger Borchert for the experimental ideas concerning solar cells, fruitful discussions, and proof-reading of Chapter 7 in this thesis;

Dr. Nikolay Radychev for help in the fabrication of hybrid solar cells and I-V measurements;

People who contributed to the measurements: *Dr. Erhard Rhiel*, *Heike Oetting*, and *Renate Kort* for assistance in obtaining TEM images and EDX data, *Marlies Rundshagen* and *Dieter Neemeyer* for assistance in obtaining NMR data, *Francesco Fabbretti* for assistance in obtaining MS data, *Mareike Ahlers* and *Katja Rieß* for assistance in obtaining TGA data, *Gunda Sängerlaub* for assistance in obtaining XRD data, *Eleonore Gründken* for assistance in obtaining AAS data, *Dr. Steffen Schulze* for assistance in obtaining HRTEM images, *Prof. Dr. Christoph Lienau* and PhD students from his group for providing the opportunity to measure PL spectra;

Everyone in our group for making the lab an enjoyable and productive place to work: *Matthias Macke* for the necessary chemicals, *Elena Selishcheva*, *Xiaoping Jin*, and *Marta Kruszynska* for a nice collaboration.

I am much obliged to my friend *Dr. Yulia Meteleva-Fischer* for the long journey that led me to Oldenburg. If it was not for her, I would not be writing this thesis in this place today.

I am very grateful to *Ruslan* for his help with LaTeX and warm encouragement. Without him, I would not be able to write this PhD thesis in the form it is now.

I owe *my family* heartiest thanks for their love, continuous support, and more things than space allows. Thanks for their readiness to help me always when I needed it.

Niedersächsisch-Israelisches Forschungsvorhaben Niedersächsisches Ministerium für Wissenschaft und Kultur und die Volkswagenstiftung and *EWE Research Group "Thin Film Photovoltaics" by the EWE AG, Oldenburg* are acknowledged for financial support.

CURRICULUM VITAE

IRINA LOKTEVA

PERSÖNLICHE DATEN

Geschlecht: weiblich
Geburtsdatum: 27. August 1985
Geburtsort: Woronesch, Russland
Staatsangehörigkeit: russisch

SCHULBILDUNG

09/1992–06/2002	Gymnasium in Woronesch (Russland) Abschluss: Abitur mit Goldmedaille

---

STUDIUM

09/2002–06/2007	Studium der Chemie an der Staatlichen Universität Woronesch (Russland) Abschluss: Diplom in Chemie mit Auszeichnung Schwerpunkt: analytische Chemie Thema der Diplomarbeit: "Quantitative Piezosensor Analyse der Wasserlösungen von Aminosäuren und Peptiden"
10/2003–06/2006	Zusätzliches Studium als Übersetzer an der Staatlichen Universität Woronesch (Russland) Abschluss: Diplom-Fachübersetzerin für Chemie (Englisch)

BERUFSERFAHRUNG UND PROMOTION

07/2007–07/2010	Doktorandin und wissenschaftliche Mitarbeiterin an der Carl von Ossietzky Universität Oldenburg, Institut für Physik, Abteilung Energie- und Halbleiterforschung, Arbeitsgruppe Nanochemie Forschungsbereich: Synthese von Halbleiternanopartikeln, deren Charakterisierung und Anwendung für die Hybrid Nanopartikel/Polymer Solarzellen
09/2004–07/2007	Sozialpädagoge der zusätzlichen Bildung am Center der Kreativitätsentwicklung für Kinder und Jugendliche in Woronesch (Russland)

VERZEICHNIS WISSENSCHAFTLICHER PUBLIKATIONEN

Artikel in Zeitschriften

1. I. Lokteva, N. Radychev, F. Witt, H. Borchert, J. Parisi, and J. Kolny-Olesiak. Surface treatment of CdSe nanoparticles for application in hybrid solar cells: The effect of multiple ligand exchange with pyridine, J. Phys. Chem. C, 114 (2010), 12784-12791
2. F. Zutz, I. Lokteva, N. Radychev, J. Kolny-Olesiak, I. Riedel, H. Borchert, and J. Parisi. Study of the influence of the Cd:Se precursor ratio during the synthesis of CdSe nanocrystals on the performance of CdSe/P3HT hybrid solar cells, Phys. Status Solidi A, 206 (2009), 2700-2708
3. V. M. Dzhagan, I. Lokteva, M. Ya. Valakh, O. E. Raevska, J. Kolny-Olesiak, and D. R. T. Zahn. Spectral features above LO phonon frequency in resonant Raman scattering spectra of small CdSe nanoparticles, J. Appl. Phys. 106 (2009), 084318
4. V. Dzhagan, M. Ya. Valakh, J. Kolny-Olesiak, I. Lokteva, and D. R. T. Zahn. Resonant Raman study of phonons in high-quality colloidal CdTe nanoparticles, Appl. Phys. Lett. 94 (2009), 243101

Konferenzbeiträge (Auswahl)

1. I. Lokteva, J. Kolny-Olesiak. Synthesis of high quality phosphine-free CdSe nanocrystal quantum dots (NQDs) using in-situ formed Cd^0 nanoparticles. Posterpräsentation, Bunsentagung 2010, 13.-15. Mai 2010, Bielefeld
2. I. Lokteva, N. Radychev, H. Borchert, J. Parisi, J. Kolny-Olesiak. Influence of pyridine treatment on the ligand shell of OA-capped CdSe nanoparticles and the impact on polymer/CdSe hybrid solar cells. Posterpräsentation, DPG Frühjahrstagung 2010, 21.-26. März 2010, Regensburg
3. I. Lokteva, V. Kloper, E. Lifshitz, J. Kolny-Olesiak. Formation of CdSe nanoparticles from in-situ formed crystalline Cd^0 particles and three different Se precursors. Vortrag, 2nd German-Danish meeting on Interface Related Phenomena, 14.-16. Juli 2008, Sønderborg (Dänemark)
4. I. Lokteva, V. Kloper, E. Lifshitz, J. Kolny-Olesiak. Formation of CdSe nanoparticles from in-situ formed crystalline Cd particles and two different Se-precursors. Vortrag, III International conference on colloid chemistry and physicochemical mechanics, 24.-28. Juni 2008, Moskau
5. I. Lokteva, V. Kloper, E. Lifshitz, J. Kolny-Olesiak. Synthesis of CdSe nanoparticles with in-situ formed crystalline Cd particles as a Cd-precursor. Posterpräsentation, Bunsentagung 2008, 1.-3. Mai 2008, Saarbrücken
6. I. A. Lokteva, A. V. Kalach, A. N. Zyablov. Piezosensor analysis of leucine and isoleucine solutions. Posterpräsentation, SENSOR Conference 2007, 22.-24. Mai 2007, Nürnberg. – S. 409-413
7. I. A. Lokteva, A. V. Kalach, A. N. Zyablov, V. F. Selemenev. Piezosensor analysis of α- and β-alanine water solutions. Posterpräsentation, International Symposium on Olfaction and Electronic Noses ISOEN 2007, 3.-5. Mai 2007, St. Petersburg. – S. 97-98

Erklärung

Hiermit erkläre ich, dass ich diese Arbeit selbständig verfasst und nur die angegebenen Hilfsmittel benutzt habe.

Oldenburg, den 03.05.2010

Irina Lokteva